

THERMAL ELECTROCHEMICAL DYNAMIC MODELING OF SEALED LEAD  
ACID BATTERIES

Except where reference is made to the work of others, the work described in this thesis is my own or was done in collaboration with my advisory committee. This thesis does not include proprietary or classified information.

---

Kevin Siniard

Certificate of Approval:

---

Daniel Harris  
Associate Professor  
Mechanical Engineering

---

Song-Yul Choe, Chair  
Associate Professor  
Mechanical Engineering

---

George Flowers  
Professor  
Mechanical Engineering

---

George Flowers  
Dean  
Graduate School

THERMAL ELECTROCHEMICAL DYNAMIC MODELING OF SEALED LEAD  
ACID BATTERIES

Kevin Siniard

A Thesis

Submitted to

the Graduate Faculty of

Auburn University

in Partial Fulfillment of the

Requirements for the

Degree of

Master of Science

Auburn, Alabama  
December 18, 2009

THERMAL ELECTROCHEMICAL DYNAMIC MODELING OF SEALED LEAD  
ACID BATTERIES

Kevin Siniard

Permission is granted to Auburn University to make copies of this thesis at its discretion,  
upon the request of individuals or institutions and at their expense.  
The author reserves all publication rights.

---

Signature of Author

---

Date of Graduation

## VITA

Kevin Siniard, son of Thomas Alan Siniard and Sheri Myers Siniard, was born on Oct 19<sup>th</sup>, 1984 in Huntsville, Alabama. He entered the University of Alabama in August 2003 and earned a Bachelors of Science degree in Mechanical Engineering in May, 2007. In August 2007, he enrolled at Auburn University to pursue a Master of Science degree in the Department of Mechanical Engineering.

## THESIS ABSTRACT

# THERMAL ELECTROCHEMICAL DYNAMIC MODELING OF SEALED LEAD ACID BATTERIES

Kevin Siniard

Master of Science, December 18, 2009  
(B.S., University of Alabama, 2007)

121 Typed Pages

Directed by Song-Yul Choe

Limitations to battery technology ranks second as the most vital problem facing the electronic and mechanical engineering industry in the future. The life span and performance of batteries specifically SLI (Starting – Lighting – Ignition) lead acid batteries have been well documented by researchers [2-9]. One of the utmost problems facing the lead acid battery performance is the thermal effect on the batteries active materials and capacity.

Despite the fact that there has been some focus on the thermodynamic principles in the battery performance, a comprehensive model of the effects is lacking. The Auburn University research will address the absence of an in-depth model of battery performance and different temperatures during the life span. The modeling focuses on the Gibbs free energy, entropy, and enthalpy changes for varying temperatures for different charging

and discharging parameters. Also, the model incorporates control volumes for each of the major constituents of the battery cells (casing, electrolyte, and electrodes). Once the thermal effects are addressed through simulation, the MATLAB model will be tested against experimental results using a thermal chamber provided by Auburn University. The thermal chamber will be used to vary the atmospheric temperature to the extremes between 0 and 80 degrees Celsius. Laboratory results will be used to validate the computerized modeling of battery performance. Additionally, vibration testing will be set to reproduce the battery environment in automotive applications in close proximity to the vehicle engine and suspension. Thermal effects will be modeled using finite element software for further representation of the battery performance under extreme environments.

## ACKNOWLEDGEMENTS

The author would like to thank the members of his research committee, Dr. Song-Yul Choe, Dr. George Flowers, and Dr. Daniel Harris for their advice and continued support during his research. He would also like to thank Mr. Xaio Meng, Mr. Joshua Sadler, and Mr. Stephen Wall for his assistance during his research work. Additional thanks are given to the other group members, faculty, and graduate students who provided help during his time at Auburn University.

Computer software used: Microsoft 2007  
MATLAB 7.0.4  
ProEngineer  
ANSYS



## TABLE OF CONTENTS

LIST OF FIGURES.....	x
NOMENCLATURE.....	xii
1 INTRODUCTION .....	1
2 BACKGROUND .....	3
2.1 Chemical Processes .....	3
2.2 Dynamic Modeling.....	6
2.3 Porosity Effects on Surface Area .....	7
2.4 Overpotential.....	9
2.4.1 Charge Transfer Overpotential .....	9
2.4.2 Diffusion Overpotential .....	11
2.4.3 Overall Overpotential.....	13
2.5 State of Charge.....	14
2.5.1 Specific Gravity of Electrolyte .....	14
2.6 Voltage Drop.....	15
2.7 Voltage Recovery.....	16
3 MODEL DESCRIPTION .....	18
3.1 Governing Equations.....	19
3.1.1 Conservation of Charge .....	19
3.1.2 Material Balance .....	21
3.1.3 Initial and Boundary Conditions.....	22
3.1.4 Equation Relationships .....	23
3.2 Thermal effects.....	26
3.3 Overall Thermal Effects .....	28
3.4 Numerical Procedures .....	31
4 MODELING RESULTS .....	36
4.1 Isothermal Modeling .....	37
4.1.1 Overpotential and Reaction Rate .....	37
4.1.2 Electrolyte Concentration .....	40
4.1.3 Phase Potentials .....	44
4.1.4 Porosity and Effective Surface Area.....	48
4.2 Temperature Effects .....	50
4.2.1 Constant Current Temperature Response .....	51

4.2.2	Dynamic Current Effects .....	57
4.2.3	Two Dimensional Finite Element Analysis .....	60
4.2.4	Three Dimensional Finite Element Analysis .....	64
5	EXPERIMENTAL TESTING .....	71
5.1	Testing Equipment .....	72
5.2	Battery Parameters .....	75
5.3	Battery Testing Station Description .....	77
5.3.1	Programmable Charge and Discharge .....	79
5.3.2	Measurement Devices .....	79
5.3.3	External Environment .....	82
5.4	Vibration Effects .....	83
6	COMPARISON OF RESULTS .....	86
6.1	Dynamic Temperature Comparison .....	86
6.2	Discharge Performance .....	89
6.3	Thermal Imaging .....	94
7	CONCLUSION .....	99
7.1	Future Work .....	103
	REFERENCES .....	104
	APPENDIX .....	106

## LIST OF FIGURES

Figure 1. Ion migration in lead acid battery cell.....	3
Figure 2. Porous electrodes.....	8
Figure 3. Current density and overpotential relationship.....	11
Figure 4. Example discharge curve at constant current 2.5A. ....	16
Figure 5. Voltage recovery example from experimental testing.....	17
Figure 6. Modeling Flow Chart. ....	19
Figure 7. Temperature distribution for 2 cell battery at $T_a=273\text{ K}$ and $T_e=298\text{ K}$ for increase of 15 A of discharge current. ....	30
Figure 8. Finite Difference Method example.....	33
Figure 9. MATLAB data analysis and program structure. ....	34
Figure 10. Data Interaction. ....	36
Figure 11. Isothermal reaction rate, $\text{A}/\text{cm}^3$ , after 15 minute discharge at 10A (.), 30 A (*), 60 A (o), 100 A (o).....	38
Figure 12. Reaction rate of the positive electrode after 15 minute discharge at 30 A and 280 K (solid), 300 K (dash), 340 K (solid dot), and 380 K (dash dot). ....	39
Figure 13. (Left) Acid concentration gradient, $\text{mol}/\text{cm}^3$ , after 15 minute discharge at 10A (g), 30 A (r), 60 A (b), 100 A (blue). (Right) Acid concentration gradient, $\text{mol}/\text{cm}^3$ , after 15 minute discharge at 60 A for various isothermal temperatures. ....	41
Figure 14. One dimensional electrolyte concentration for 30 A discharge. ....	42
Figure 15. (Left) Concentration gradient, $\text{mol}/\text{cm}^3$ , after 30 minute discharge at 5 A, 20 A, 40 A, and 80 A. (Right) Acid concentration gradient, $\text{mol}/\text{cm}^3$ , after 30 min charge at 45 A from 50% SOC at various isothermal temperatures.....	43
Figure 16. Electrolyte concentration 0 s, 100 s, 500 s, 1000 s, and 1500 s after load is removed.....	44
Figure 17. Solid Phase Potential. (Black) Response after 500s of 30 A discharge. (Blue) Response after 1200s of 30 A discharge.....	45
Figure 18. Electrolyte phase potential for 60 A discharge.....	46
Figure 19. Discharge curves for 12 V lead acid battery under various loads. ....	48
Figure 20. Initial porosity parameter effects for 60 A discharge. ....	50
Figure 21. Temperatures for a 60 A charge. Adiabatic, solid line, non-adiabatic, dashed line.....	52
Figure 22. Temperature for a 100 A charge. Adiabatic, solid line, non-adiabatic, dashed line.....	53
Figure 23. Coefficient temperature dependence. ....	54
Figure 24. Electrolyte concentration for isothermal, adiabatic, and non-adiabatic models after 150 A discharge for 1200s, with initial temperature 300 K. ....	55

Figure 25. (Left) Discharge for 100 A. (Right) Charge for 15A or .25C for 60 A-h battery. Solid line, isothermal, dotted line, adiabatic, thick line, non-adiabatic.....	56
Figure 26. Terminal Voltage response to dynamic current.....	58
Figure 27. Ramp input temperature response. ....	59
Figure 28. Electrode, separator, and current collector configuration. ....	61
Figure 29. Two-dimensional thermal profile under 60 A current load.....	63
Figure 30. Blueprint of battery configuration. ....	65
Figure 31. Temperature distribution for 60 A discharge after 3 min. ....	67
Figure 32. Three-dimensional thermal profile during discharge. ....	68
Figure 33. Transient non-adiabatic temperature modeling comparison during the first ten minutes of 60A discharge. ....	69
Figure 34. Automobile electrical system diagram [26]. ....	71
Figure 35. Battery testing station. ....	74
Figure 36. Experimental setup wiring diagram.....	75
Figure 37. Battery LabView Control Station screenshot. ....	78
Figure 38. Vibration experimental results during the initial stages of discharge. ....	84
Figure 39. Transient temperature, (Top) Experimental, (Bottom) Modeling. ....	87
Figure 40. Temperature comparison for 1.25C (75 A) discharge current. ....	88
Figure 41. Reference at 300K, 100 % SOC. Solid, experiment, dashed, model. ....	89
Figure 42. Ambient temperature effects on terminal voltage comparison during 45 A discharge. (Top) experimental, (Bottom) modeling. ....	91
Figure 43. Step Response for discharge at 300 K. ....	93
Figure 44. 50 A pulse discharge response. ....	94
Figure 45. Thermal imaging and FE analysis comparison at 60 A discharge. ....	96
Figure 46. Specific areas temperature comparison 600s after initial 60 A load. ....	97

## NOMENCLATURE

a	Specific surface area for electrode ( $\text{cm}^{-1}$ )
$c_p$	Specific heat ( $\text{J/kg-K}$ )
D	Diffusion coefficient ( $\text{cm}^2/\text{s}$ )
$E_j$	Open circuit potential (V)
F	Faraday's constant ( $96,487 \text{ C/mol}$ )
h	Heat transfer coefficient ( $\text{W/cm}^2\text{-K}$ )
H	Enthalpy (J)
$i_0$	Reference exchange current density ( $\text{A/cm}^2$ )
I	Applied current density ( $\text{A/cm}^2$ )
j	Transfer current density ( $\text{A/cm}^2$ )
k	Thermal conductivity ( $\text{W/m-K}$ )
q	Volumetric heat generation rate ( $\text{W/cm}^3$ )
Q	State of charge, SOC
R	Universal gas constant ( $8.3143 \text{ J/mol-K}$ )
S	Partial molar entropy ( $\text{J/mol-K}$ )
$t_+^0$	Transference number
T	Cell temperature (K)
$V_c$	Cell volume ( $\text{cm}^3$ )

### **Greek symbols**

$\alpha$	Transfer coefficient
$\delta$	Exchange current density correction factor
$\varepsilon$	Porosity of a porous medium
$\gamma$	Activity coefficient
$\phi$	Potential in a phase (V)
$\eta$	Surface overpotential (V)

$\kappa$	Ionic conductivity of electrolyte (S/cm)
$\kappa_D$	Diffusional conductivity (A/cm)
$\rho$	Density (g/cm <sup>3</sup> )
$\sigma$	Conductivity of solid active material (S/cm)
$\nu$	Stoichiometric coefficient
$\zeta$	Area correction factor

**Subscripts**

a	Anode reaction
b	Battery
c	Cathode reaction
e	Electrolyte phase
eff	Effective
int	Internal
irr	Irreversible
j	Grid number
n	Electrode reaction, Pb, PbO <sub>2</sub>
rev	Reversible
s	Solid phase
t	Charge transfer

# *1 INTRODUCTION*

Advancements in automotive battery technology from electrode and electrolyte materials to a range of environmental effects on battery performance have been the leading focus for researchers in recent years. There have been a number of approaches implemented to characterize battery performance for traditional internal combustion vehicles and hybrid battery applications.

Esperilla and Felez addressed the thermal effects on lead acid batteries in terms of thermodynamic equations along with an equivalent circuit to represent the electrochemical reaction of the battery cells [3]. An alternative method, presented by Gu et al, uses a Thevenin equivalent model focusing on battery electrochemistry by considering activity of the migrating ions and porosity of electrodes to obtain a more comprehensive model of the battery during charge and discharge [5]. Kim and Hong focused on effects of varying battery parameters on the electrolyte concentration and discharge performance neglecting temperature change. Additionally, close attention was paid to the effects of the limiting current density [9].

Although there are models that concentrate on specific aspects of automotive batteries, the need for a complete model of a six cell battery performance remains. The approach outlined in this work includes various aspects of previously mentioned models as well as a few novel techniques to represent the battery's physical properties

and performance. Accepted electrochemical, thermodynamic, and heat transfer methods are employed as the equivalent circuit does not adequately represent complex battery electrochemistry and mass transport. In order to obtain an adequate representation of the automotive battery, the model will be subjected to several charge and discharge methods. However, the effects of temperature and heat generation focus mostly on the discharge process when high current is present. The environments to which the battery will be tested and modeled consist of an array of temperatures and intensities of vibration as part of the battery testing station which includes a programmable thermal chamber and shaker.



## 2 BACKGROUND

### 2.1 Chemical Processes

The driving force behind any battery is the reversible chemical reaction that occurs between the electrodes and electrolyte. The reaction below shows the chemistry of the battery at discharge. The reversible process will move in the opposite direction when charging.

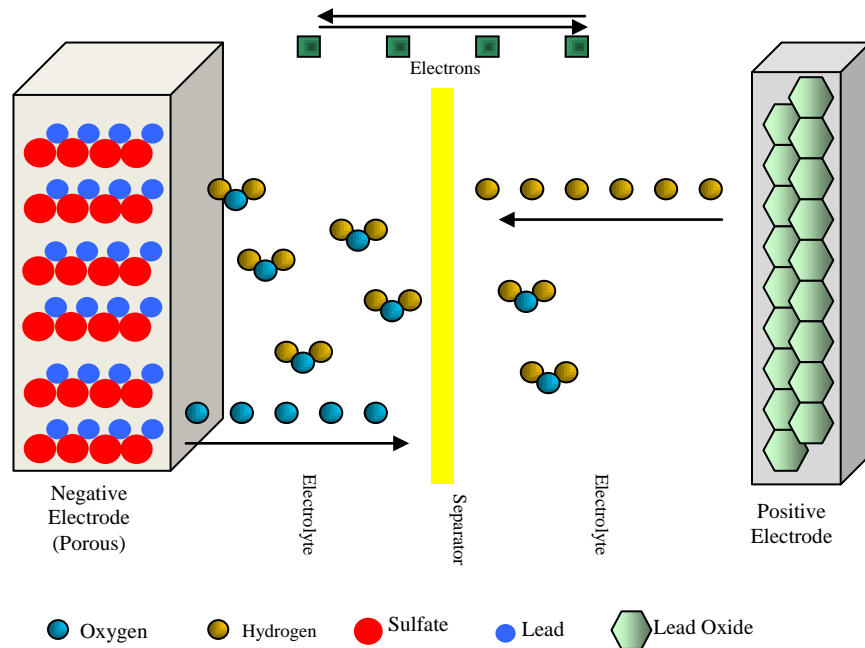
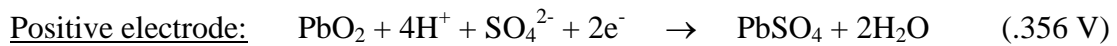
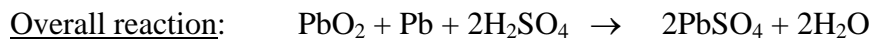


**Figure 1.** Ion migration in lead acid battery cell.

Oxidation occurs at the anode and reduction at the cathode. As shown above, during discharge the negative electrode gives up electrons and the positive accepts electrons. During discharge, the negative electrode experiences reduction, and is therefore the cathode. The positive electrode or anode experiences oxidation or the acceptance of charge. For the charge processes, the roles are reversed therefore labeling an electrode as the cathode or anode is not appropriate for all cases.

When under no load conditions the battery settles at a chemical equilibrium, but due to the opposing charges an electric potential is created. Prior to current flow experienced during charge or discharge, the battery has an initial electromotive force, EMF, which describes the force between protons and electrons of a given molecule. The EMF of the galvanic cell is described by the difference in the electrode potentials when there is no external current between the terminals. This is not to be confused with open circuit voltage, Equation 1, which possesses the opposite sign.

$$E = E_c - E_a \quad (1)$$

where  $E_a$  and  $E_c$  are the potentials of the cathode and anode, respectively [6]. The electromotive force of a cell can be derived using Gibbs Free Energy which calculates electrical potential from a provided chemical potential of each of the chemical compounds. The change in Gibbs Free Energy is a result of the reactants and products of the chemical equation where each compound has a similar change in Gibbs Free Energy from the corresponding chemical reaction [1]. By calculating the difference in the Gibbs Free Energy of the products and reactants, a change in energy is obtained. For the chemical reaction described above, the overall change in Gibbs Free Energy is 1729.1 kJ

and 2100.3 kJ for the reactants and products, respectively, resulting in a total energy change of 371.2 kJ [1]. Therefore, the electric potential of the cell is calculated by dividing the change in Gibbs Free energy,  $G$ , by the product of the number of electrons transferred,  $n$ , and Faraday's constant,  $F$ . The electromotive force for a single cell is calculated below:

$$E^{\circ} = \frac{\Delta G^{\circ}}{n \cdot F} = \frac{371.2 \text{ kJ}}{2 \cdot 96,495 \text{ C}} = 2.0 \text{ V} \quad (2)$$

A typical sealed lead acid battery consists of six cells, resulting in an overall battery voltage of 12.0 V, in units of energy per unit charge. In order to evaluate the overall systems of the battery there are a few initial conditions that must be determined and since Gibbs Free Energy of the components cannot be measured, the electrolyte concentration is substituted. When observing the battery at charge or discharge the initial cell potentials are of great concern. First, the values of standard potential,  $E^{\circ}$ , refer to the amount of available energy when the electrolyte concentration is maximized. Therefore, the dependence of cell potential on acid concentration when no current is flowing is determined by the Nernst Equation, shown below

$$E = E^{\circ} - \frac{R \cdot T}{n \cdot F} \ln \prod_{i=1}^{\infty} (m_i \gamma_i)^{\nu} \quad (3)$$

where  $R$  is the gas constant,  $T$  is temperature,  $m$  is molality (acid concentration),  $\gamma$  is activity coefficient, and  $\nu$  is the stoichiometric coefficient. Several values for the electrode potentials at various concentrations found through experimental process are provided by reference materials [1].

The activity coefficient is electrolyte concentration dependent and is a combination of the negative and positive ions involved in the reaction and cannot be individually calculated [5]. For the purposes of modeling, the activity coefficient is found as a function of molality by curve fitting to the reference data [1]. The stoichiometric coefficient is taken from the chemical reactions described above.

## ***2.2 Dynamic Modeling***

The dynamic performance of a lead acid battery is dependent on several parameters which are constantly changing. This complexity of the internal chemical reactions of the battery requires a few assumptions in order to appropriately model battery performance. The relationships governing the battery performance are based on the following assumptions made by Tiedemann and Newman [10]:

- i) The lead acid cell is comprised of a lead dioxide electrode,  $\text{PbO}_2$ , an electrolyte reservoir, a porous separator and a lead electrode,  $\text{Pb}$ .
- ii) The electrolyte is completely dissociated into  $\text{H}^+$  and  $\text{HSO}_4^-$  ions
- iii) The initial temperature of the battery is 300 °K
- iv) The model is one-dimensional in the direction perpendicular to the electrodes

Various modeling and experimental efforts will test the response of the batteries initially under constant current and voltage applications. Experimental testing will employ various step and ramp discharge methods. Although constant loads or supply charges are applied, the rate at which the battery materials perform charging or discharging is not linear but determined by the rate of the reactions at the battery

electrodes and electrolyte. Since chemical reactions are the driving force behind battery cycles, the rate of reaction refers to the amount of mol transferred per second. The amount of time needed to discharge the battery, determined by the slowest reaction, is a function of current density,  $i$ , the number of electrons transferred,  $z$ , Faraday's constant,  $F$  and the active surface area,  $A$ . The rate of reaction is given by Equation 4.

$$j = \frac{dn}{dt} = \frac{i \cdot A}{z \cdot F} \quad \Rightarrow \quad \frac{\frac{\text{amps}}{\text{cm}^2} \cdot \text{cm}^2}{\frac{\text{amps} \cdot \text{s}}{\text{mol}}} = \frac{\text{mol}}{\text{s}} \quad (4)$$

### 2.3 Porosity Effects on Surface Area

The effective surface area, shown in Equation 7, and current density of the electrode determines the rate of reaction and the amount of available energy, therefore, accurate area calculations are essential to the modeling effort. The variation of porosity,  $\epsilon$ , of the porous electrodes illustrated below must be considered to fully represent the electrode surface area. Porosity change is shown in Equation 5, where molecular weight,  $MW$ , and density,  $\rho$ , quantifies the percentage of the electrode not in solid phase:

$$\begin{array}{cc} \text{Lead, Pb} & \text{Lead Oxide, PbO}_2 \\ \frac{\partial \epsilon}{\partial t} = \frac{1}{2F} \cdot \left( \frac{MW_{PbSQ}}{\rho_{PbSQ}} - \frac{MW_{Pb}}{\rho_{Pb}} \right) \cdot j & \frac{\partial \epsilon}{\partial t} = \frac{1}{2F} \cdot \left( \frac{MW_{PbO_2}}{\rho_{PbO_2}} - \frac{MW_{PbSQ}}{\rho_{PbSQ}} \right) \cdot j \end{array} \quad (5)$$

where  $j$  is the reaction rate and the value in the parenthesis is the determined by material properties [9]. Illustrated in Figure 2, the porosity varies as the porous electrodes are filled with lead sulfate during the discharge process. Conversely, as the electrodes become increasingly porous, the sulfuric acid-water electrolyte fills the vacated spaces

improving the effective surface area. The detailed contribution of porosity is later explained in the material balance equation.

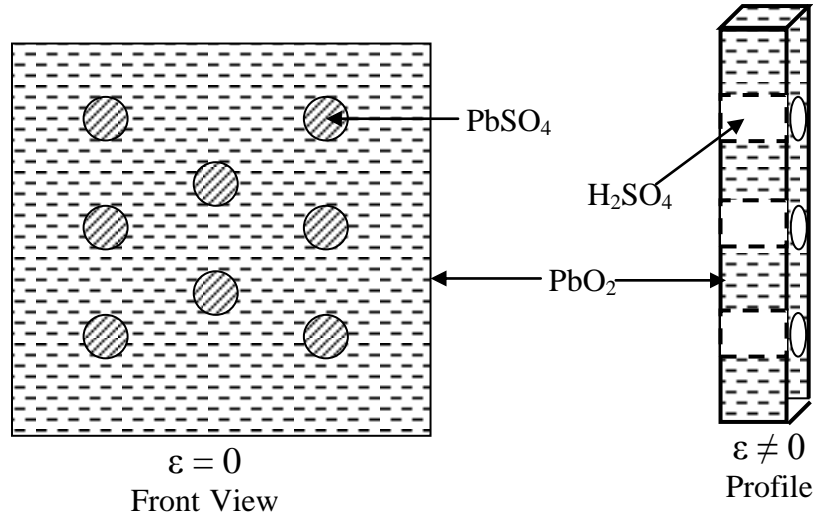


**Figure 2. Porous electrodes.**

Porosity for the electrolyte reservoir or the separator are specified as

$$\begin{aligned} \epsilon &= 1 \text{ for the reservoir, purely liquid} \\ \epsilon &= \epsilon_{\text{sep}} \text{ is a constant for the separator} \end{aligned}$$

Additionally, the rate of reaction determines the concentration of the electrolyte at a given time. Taking values for concentration prior to application of charge and discharge loads, the amount of sulfuric acid in the electrolyte can be determined at any instance during the processes from the previously mentioned reaction rate.

The state of charge or depth of discharge refers to the percentage of available capacity and is used to determine the electrode active surface area at a given time. Comparing the instantaneous and maximum state of charge along with the experimentally calculated correction factor,  $\zeta$ , provides the electrode surface area in Equation 6 below [6].

$$\text{Charge: } a_n = a_{n,\max} \cdot \left( \frac{Q}{Q_{\max}} \right)^\zeta \quad \text{Discharge: } a_n = a_{n,\max} \cdot \left( 1 - \frac{Q}{Q_{\max}} \right)^\zeta \quad (6)$$

## 2.4 Overpotential

The previously mentioned Nernst equation describes the battery potential at equilibrium, or when there is an absence of current flow. However, when charge or discharge current is applied, there is a difference between the equilibrium and actual battery potential. The discrepancy between the two values is known as overpotential,  $\eta$ . Various processes effect overpotential. Only the most significant values of overpotential, which occur as a result of charge transfer during chemical reactions, ohmic losses, and diffusion of ions across the electrolyte, will be considered. Specifically, overpotential is calculated as the difference in solid phase and electrolyte phase potentials compared to the equilibrium potential.

$$\eta = \varphi_s - \varphi_e - E_{\text{Pb}} \quad (\text{negative electrode}) \quad (7)$$

$$\eta = \varphi_s - \varphi_e - E_{\text{PbO}_2} \quad (\text{positive electrode}) \quad (8)$$

where  $\varphi_s$  is the potential of the electrode solid phase,  $\varphi_e$  is the potential of the electrolyte phase,  $E_{\text{Pb}}$  is the equilibrium potential of the negative electrode, and  $E_{\text{PbO}_2}$  is the equilibrium potential of the positive electrode [6].

### 2.4.1 Charge Transfer Overpotential

Charge transfer overpotential occurs at the battery electrodes where there is electron transfer between electrode and electrolyte. A significant amount of energy is

dissipated as result of the charge transfer resulting in a decreased cell potential. Charge transfer overpotential,  $\eta_t$ , is calculated using the Butler-Volmer equation [3]:

$$\frac{i}{i_o} = \exp\left(\frac{\alpha_a \cdot F}{R \cdot T} \cdot \eta_t\right) - \exp\left(-\frac{\alpha_c \cdot F}{R \cdot T} \cdot \eta_t\right) \quad (9)$$

The first term of the expression above corresponds to the oxidation reaction and represents the anodic current. The second exponential term corresponds to the reduction reaction and represents the cathodic current. In Equation 10, current density is represented as a function of overpotential. Therefore, overpotential affects the transfer rate of electrons between the reactants. However, for modeling purposes, overpotential is required as a function of current density,  $\eta_t = f(i)$ . Since the function cannot be directly calculated from the Butler-Volmer equation, approximations known as Tafel Equations are formulated to represent overpotential at various extremes. For large overpotential at the anode, Equation 10 is used:

$$\eta_t = \frac{R \cdot T}{z \cdot \alpha \cdot F} \cdot \ln \frac{i}{i_o} \quad (10)$$

For large overpotential at the cathode, Equation 11 is employed:

$$\eta_t = \frac{R \cdot T}{z \cdot (1 - \alpha) \cdot F} \cdot \ln \frac{i_o}{|i|} \quad (11)$$

For smaller overpotential there is a linear relationship between the overpotential and current density as the overpotential at the anode and cathode shown in Figure 3 are summed [7]:



$$\eta_t = \frac{R \cdot T}{i_o \cdot F} \cdot i \quad (12)$$

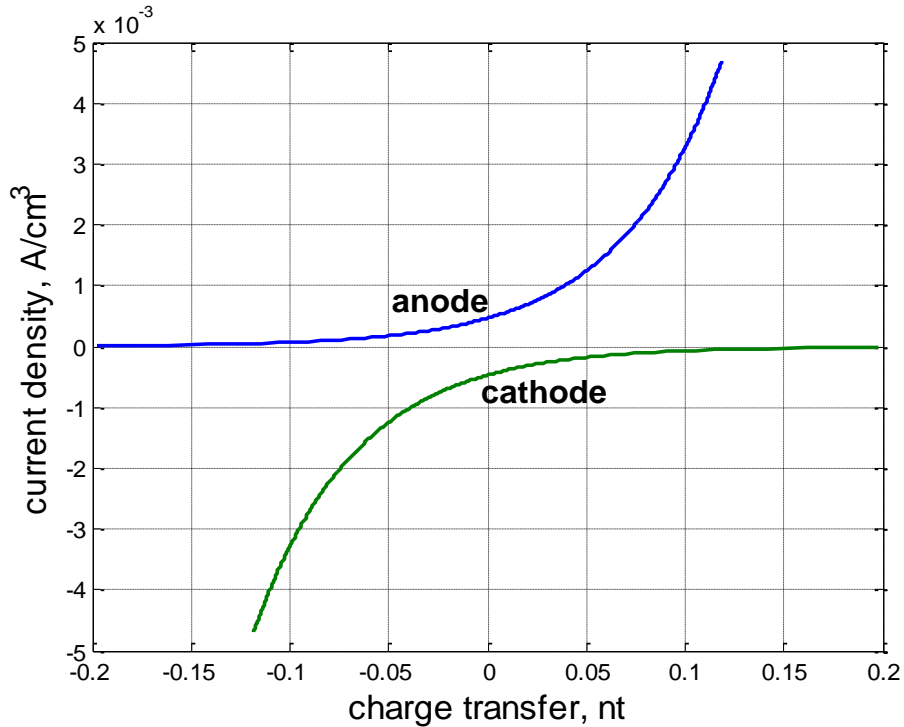


**Figure 3.** Current density and overpotential relationship.

### 2.4.2 Diffusion Overpotential

When the battery experiences current flow, components of the chemical reactions are being transported in both directions and a diffusion layer forms between the electrode and electrolyte. The diffusion layer refers to an area where the concentration gradient is not equal to zero. As the electrolyte concentration changes, diffusion overpotential is created and the cell potential now differs from the equilibrium potential. Behavior of the complex diffusion layer is modeled using the Nernst layer in which the gradient is

assumed constant. Using this approximation, the effects of ion diffusion across the electrolyte reservoir is calculated using the following equation:

$$\eta_d = \frac{R \cdot T}{n \cdot F} \cdot \ln \Pi \left( 1 - \frac{i}{i_L} \right)^v \quad (13)$$

The variables in Equation 13 are consistent with the values inserted into the Nernst equation with the exception of the limiting current density,  $i_L$ . At a given current, the concentration gradient and the current density reach a maximum known as the diffusion limiting current density. If the activity of the ions formed increases due to the chemical reaction, the diffusion gradient is directed away from the electrode where the reaction took place. The limiting current density, in Equation 14, is a function of the activity of the electrolyte, the diffusion coefficient, and diffusion layer thickness [1]

$$i_L = \frac{z \cdot F \cdot D \cdot \gamma}{\delta} \quad (14)$$

and

$$\delta = \frac{2}{\sqrt{\pi}} \cdot \sqrt{D \cdot t}$$

where D is the diffusion coefficient, t is time, z is number of electrons transferred, F is Faraday's constant,  $\gamma$  is the activity, and  $\delta$  is the diffusion layer thickness [1].

The diffusion coefficient determines diffusion rate of ions across the electrolyte reservoir and is concentration and temperature dependent. The diffusion coefficient equation, D, is found by curve fitting to experimental values taken for various concentrations, C and temperature, T shown below [9]. When the temperature is equal to the specified room temperature, 300 °K, the exponential term becomes unity.

$$D = \exp\left[\frac{2174.0}{298.15} - \frac{2174.0}{T}\right] \cdot (1.75 + 260.0 \cdot c_e) \cdot 10^{-5} \quad (15)$$

### 2.4.3 Overall Overpotential

Charge transfer overpotential takes place at the anode and cathode when bonds are created and broken between the elements of the electrode and electrolyte, causing a transfer of ions or electrons. Diffusion overpotential is a result of differing ion concentrations and is quantified for both electrode processes. In order to evaluate cell potential, the total dissipated energy, or overpotential, at each electrode must be considered. The overpotentials at the anode and cathode are denoted by subscripts a and c, respectively

$$E = E^\circ + (\eta_t + \eta_d)_a - (\eta_t + \eta_d)_c - I \cdot R_{\text{int}} \quad (16)$$

where I, current, represents the current flowing through the cell calculated as the product of the electrode current density and surface area and  $R_{\text{int}}$  is the resistance of the separator and electrolyte [1]. Overpotential is provided as a function of the current density of the electrodes outlined in Section 2.4.1. Following overpotential calculations, investigations of the energy transfers effect on internal temperature variation is necessary. However, since electrical and chemical potentials cannot be measured separately, the overall overpotential is obtained through comparison with a reference state shown in Equation 2 [1]. The reference state refers to the standard potential at a given electrolyte concentration, which is calculated from the change in Gibbs Free Energy discussed in Section 2.1.

## ***2.5 State of Charge***

Now that the electrochemical background is set, measurement and calculations of battery parameters are the main focus. The State of Charge (SOC) of the battery refers to the ratio of available energy and the maximum amount of available energy the battery is capable of providing. Evaluating battery SOC is vital for both modeling and experimental efforts. Despite the importance of valid SOC modeling approximations and measurements, there is no widely accepted standard method for either application. Discharging the battery to 0% SOC remains the only method to precisely measure a partially discharged battery's state of charge. In order to avoid the negative effects from extremely low SOC, a few more practical alternatives are commonly implemented.

### **2.5.1 Specific Gravity of Electrolyte**

Prior to the implementation of complex computer modeling, researchers estimated SOC by measuring the electrolyte specific gravity using a hydrometer. The chemical reactions described in Section 2 describe the conversion of the electrolyte from sulfuric acid to water during discharge. Conversely, as the battery charges, the amount of sulfuric acid in the electrolyte increases.

Sulfuric acid has a specific gravity of 1.28, while water is 1.0. Since the relationship between SOC and electrolyte specific gravity is linear, a useful estimation of SOC can be calculated. However, the specific gravity method is not suitable for sealed lead acid (SLA) battery, because when opened SLA batteries are rendered useless. Additionally, safety is a great concern due to the volatility of sulfuric acid. Therefore, temperature and

specific gravity readings directly from the battery cells will not be carried out during the experimentation process [19].

## **2.6 Voltage Drop**

There are several phenomena experienced during the observations of the processes of lead acid batteries. Constant discharge currents provide a nearly linear discharge curve, as shown in Figure 4, until the battery voltage decreases beyond harmful levels causing the internal resistance to drastically increase resulting in permanent capacity loss. However, when a battery is initially subjected to a load and current begins to pass through the components, an instantaneous voltage drop occurs across the terminals. The sudden drop is caused by the initial internal resistance of the battery components and is calculated as

$$V_{drop} = I_b \cdot R_{int} \quad (17)$$

where  $I_b$  is the total current passed through the battery, and  $R_{int}$  is the total internal resistance of the battery. For modeling reasons, the battery internal resistance is approximated from provided battery specifications in order to predict the voltage drop for a given discharge current. However, during experimental processes the voltage drop is used to compute the internal resistance of the battery during different stages of the testing procedures providing an approximation of the cycling effects on battery capacity.

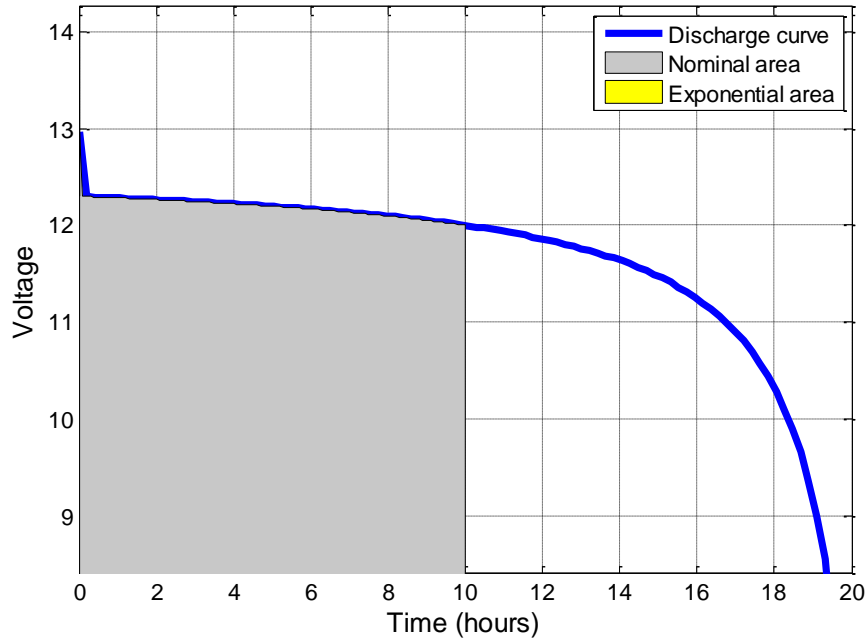


**Figure 4.** Example discharge curve at constant current 2.5A.

## 2.7 Voltage Recovery

Similar to the initial voltage drop of the battery when a load is applied, when a load is removed the battery experiences what is known as voltage recovery. All types of automotive batteries experience this phenomena but at different rates. Similar to the initial voltage drop experienced, the amount of voltage recovered is dependent on the discharge current and internal resistance of the battery. Estimation of internal resistance is difficult leading to the extraction of the parameters from experimental data. Typically, a series of steps increasing the current followed by a period of rest is utilized to observe the amount of voltage drop and recovery at the instances when current is increased or removed from the system. An example derived from experimental data is provided below where  $R_0$  and  $R_1$  are functions of SOC and temperature [25]. The current applied

is represented as  $I_1$  in Figure 5. Once the data for voltage drop and recovery is extracted, mathematical representation of the phenomena is formulated providing an estimation of initial voltage drop and final equilibrium potential.

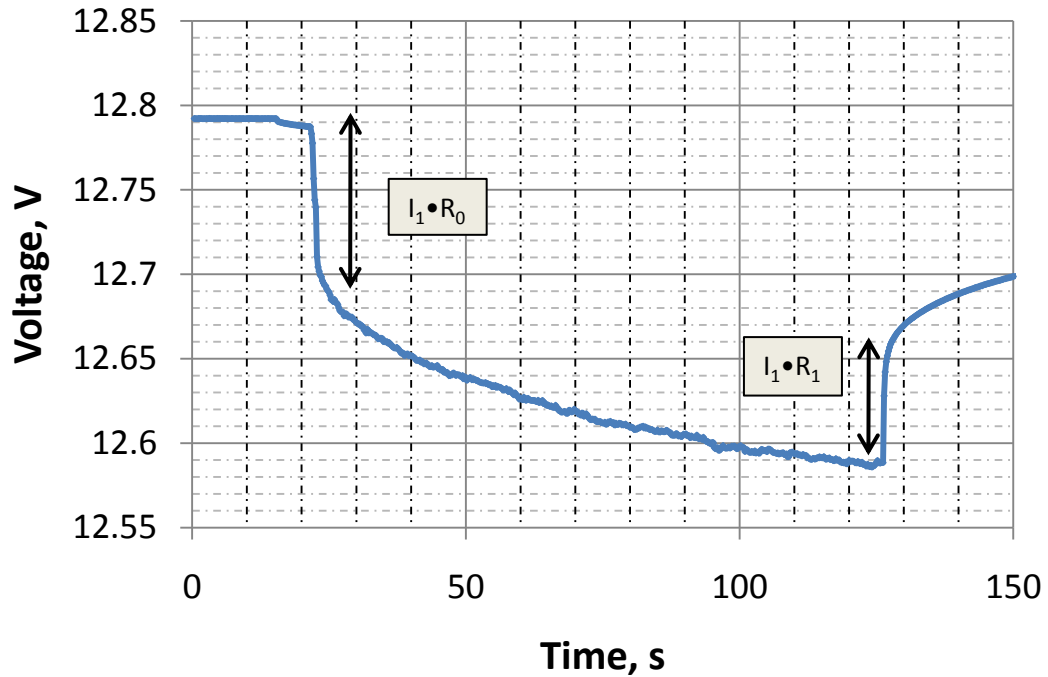


**Figure 5.** Voltage recovery example from experimental testing.

The illustration in Figure 5 gathered from experimental testing, shows a very distinctive voltage drop and recovery after the load is removed. The initial voltage drop and voltage recovery values are used to estimate the internal resistance of the battery for the computer simulations.

### *3 MODEL DESCRIPTION*

Once previous lead acid battery dynamic models were researched and scrutinized, an outlined approach was defined. In order to thoroughly represent the performance of a sealed lead acid battery, a 1D electrochemical approach is employed. However, a simple one dimensional model will not properly account for electrode active surface area, therefore the model assumes electrode surface area and electrolyte concentration is constant in the direction along the electrode surfaces. Several researchers have incorporated complicated equivalent circuits to represent the various components of the battery. While the equivalent circuit approach provides a basic estimation of the inner workings of the battery, the electrochemical processes that are the backbone of the battery are neglected. For instance, equivalent circuit methods provide effective surface area values as a mere function of the SOC [14]. In reality, electrode effective surface area is a product of the material porosity, reaction rate and the electrode-electrolyte interface, temperature, diffusion rate, and electrolyte concentration. Due to the complexity of the chemical reactions and the movement of ions across the electrolyte reservoir a one-dimensional model is able to provide concentration of ions, temperature, reaction rate, and phase potentials of the battery cell. The flow chart in Figure 6 outlines, from left to right, the specified input values, governing equations, and modeling outputs.



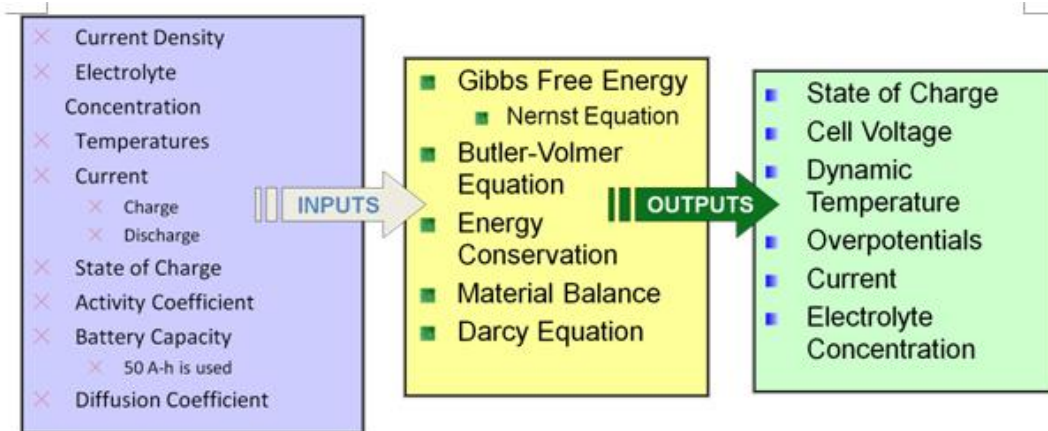


**Figure 6. Modeling Flow Chart.**

### **3.1 Governing Equations**

While the Gibbs Free Energy and Butler-Volmer Equations were briefly covered, the succeeding differential equations require a more in-depth discussion. The energy conservation, material balance, and Darcy equations characterize the dynamic physical and chemical properties of the battery during the charge and discharge processes.

#### **3.1.1 Conservation of Charge**

To fully understand the electrochemical dynamics of a lead acid battery, it is important to examine the physical processes that cause the reactions to occur. First, current flowing through the electrolyte phase of the positive electrode is driven by electric potential and the varying concentrations near the electrode/electrolyte interface. Movement of ions and flow of electrons are vital processes in battery performance, and the conductivity of the active materials determines the rate of that flow. Quantifying the ionic electrolyte conductivity, as with the diffusion coefficient, requires calculations as a function of electrolyte concentration and temperature [9].

$$\kappa = c_e \cdot \exp \left[ 1.1104 + (199.475 - 16097.781 \cdot c_e) \cdot c_e + \frac{3916.95 - 99406.0 \cdot c - \frac{721960}{T}}{T} \right] \quad (18)$$

Ionic conductivity, calculated above, is employed to determine effective ionic conductivity,  $\kappa^{eff}$ , incorporating porosity effects and diffusional conductivity,  $\kappa_D^{eff}$ , describing transference effects

$$\kappa^{eff} = \kappa \cdot \varepsilon^{1.5} \quad (19)$$

$$\kappa_D^{eff} = \frac{R \cdot T \cdot \kappa^{eff}}{F} \cdot (2 \cdot t_+^0 - 1)$$

where  $t_+^0$  is the transference number, which refers to each set of ions contribution to the overall current [6]. Involved in the charge transport of the ions in the electrolyte mixture, the transference number is unique to each chemical reaction. The overall transference number, derived from experimental data, refers to the transference of the hydrogen ion [13]. The result of the forces in liquid phase on the system is described by the conservation of charge equation

$$\frac{\partial}{\partial x} (\kappa^{eff} \cdot \frac{\partial \phi_e}{\partial x}) + \frac{\partial}{\partial x} [\kappa_D^{eff} \cdot \frac{\partial (\ln c)}{\partial x}] + a_n \cdot i_n = 0 \quad (20)$$

where  $i_n$  is the current density in the electrolyte or solid phase,  $\phi_e$  is the electrolyte potential,  $c$  is the concentration of the electrolyte,  $a_n$  is the active area,  $\kappa^{eff}$  is the effective electrolyte conductivity, while  $\kappa_D^{eff}$  includes tortuosity effects.

### 3.1.2 Material Balance

While the conservation of charge equation describes the reaction at the electrodes, the material balance equation illustrates the chemical processes across the entire battery cell. Material balance is a function of the concentration of the ions that make up the electrolyte as well as the diffusion caused by the concentration gradient of those ions. Furthermore, the electrolyte fills spaces of the porous electrodes, therefore the porosity of the electrodes must be considered. The effective diffusion coefficient,  $D_{eff}$ , is calculated using the equation below

$$D^{eff} = D \cdot \varepsilon^\zeta \quad (21)$$

where the diffusion coefficient,  $D$ , found using Equation 15 as a function of electrolyte concentration and temperature. The overall material balance equation is

$$\frac{\partial(\varepsilon_e \cdot c)}{\partial t} = \frac{\partial}{\partial x} \left( D_{eff} \cdot \frac{\partial c}{\partial x} \right) + \frac{3-2 \cdot t_+^0}{2 \cdot F} \cdot a_n \cdot i_n \quad (22)$$

where  $t_+^0$  is the transference number,  $c$  is electrolyte concentration,  $F$  is Faraday's constant,  $\varepsilon$  is porosity,  $a_n$  is effective surface area, and  $i_n$  is effective current density [6]. The conservation of species equation above removes the effects of momentum outlined in C. Y. Wang and Gu models. Momentum conservation, which is a function of electrolyte saturation, only exhibits significant effects during overcharge, therefore is neglected in this study.

As the rate of reaction directly changes the current density, the concentration is also affected. In addition, as the concentration and current density is affected, the diffusion coefficient changes, altering the diffusion rate of the ions across the electrolyte

reservoir. Consequently, the reaction rate determined by the Butler Volmer Equation directly and indirectly effects each parameter described in conservation of species.

### 3.1.3 Initial and Boundary Conditions

As with any dynamic system, initial and boundary conditions are necessary to initiate and close the mathematical modeling. Previously mentioned equilibrium potentials are set to provide an initial battery voltage. Similarly, electrolyte concentration, cell temperature, and initial current density are specified parameters. The first area of consideration is current density of the battery components. The initial current experienced by the current collectors is defined as

$$-\sigma_{eff} \cdot \frac{\partial \phi_s}{\partial x} \Big|_{x=0} = -\sigma_{eff} \cdot \frac{\partial \phi_s}{\partial x} \Big|_{x=L} = \frac{I}{A} \quad (23)$$

for a given current density, while everywhere else on the cell boundary is defined as

$$\frac{\partial \phi_e}{\partial x} \Big|_{x=0} = \frac{\partial \phi_e}{\partial x} \Big|_{x=L} = 0 \quad (24)$$

The initial conditions of various battery parameters are determined as a function of initial electrolyte concentration. Therefore, initial electrolyte concentration at the boundaries is of great concern. First, the initial concentration is equal to the concentration prior to load and there is no gradient at the boundaries of the electrodes and current collectors [6].

$$c_{e,initial} = c_0 \quad \text{and} \quad \frac{\partial c}{\partial x} \Big|_{x=0} = \frac{\partial c}{\partial x} \Big|_{x=L} = 0 \quad (25)$$

Furthermore, there is no electrolyte flow prior to current flow through the battery, so the change in electrolyte concentration at the boundaries is shown above to equal zero. As outlined in the introduction, thermal effects on the dynamic performance of the battery are the main focus of the research. The initial cell temperature is set to 300 K, but is altered with the introduction of varying ambient temperatures.

$$-k \cdot \frac{\partial T}{\partial x} = h \cdot (T_a - T) \quad (26)$$

Where  $k$  is thermal conductivity of the outer casing,  $h$  is the overall convective heat transfer coefficient,  $T_a$  is the ambient temperature, and  $T$  is the internal temperature of the battery. When the battery experiences low currents, the amount of heat transfer between the environment and battery is negligible.

### 3.1.4 Equation Relationships

Further examination of the Butler-Volmer, material balance, conservation of charge and species equations lead to a number of model simplifications. As with any problem, it is important to first identify the critical variables present. The first vital value is overpotential. As outlined above, there is a solid phase potential,  $\phi_s$ , and electrolyte phase potential,  $\phi_e$ , for each point across the battery cell. Comparison with the equilibrium potential,  $E$ , provides the overpotential or difference between equilibrium and actual battery potential. The equilibrium potential for each electrode at various electrolyte concentrations is provided reference material. Curve fitting to the tabular values results in the following relationship for the positive and negative electrodes potentials to electrolyte concentration [1]:

$$E_-(c) = -0.0002c^5 + 0.0032c^4 - 0.0224c^3 + 0.0725c^2 - 0.1267c - 0.2226 \quad (27)$$

$$E_+(c) = 0.0002c^5 - 0.0034c^4 + 0.024c^3 - 0.0759c^2 + 0.1303c + 1.55 \quad (28)$$

As outlined in Section 2.4, the values of overpotential will remain in the linear portion for normal battery operating conditions. For lead acid batteries, the variation of overpotential can be fitted by a straight line with errors of only .02-.04 V for overpotential values up to .4 V. Therefore, the Butler-Volmer Equation can be linearized, in order to remove the exponential terms. Once the equation is linearized, substitution into the conservation of charge equation represents the overall response of the system shown in Equation 30. Simplification of the equations also creates a more timely convergence of the equations for each cell division [5].

$$\frac{\partial}{\partial x} (\kappa^{eff} \cdot \frac{\partial}{\partial x} \phi_e) + \frac{\partial}{\partial x} [\kappa_D^{eff} \cdot \frac{\partial}{\partial x} (\ln c)] + a_n \cdot i_n = 0 \quad (29)$$

where

$$j_H = a_n \cdot i_n = i_0 \cdot \left( \frac{c}{c_{max}} \right)^\gamma \cdot \left( \frac{\alpha_a + \alpha_c}{R \cdot T} \cdot F \right) \cdot (\phi_s - \phi_e - E) \quad (30)$$

Due to the slowly changing acid concentration, initially the second term in the conservation of charge equation is taken as constant. Therefore, the concentration and temperature at a given time is used to calculate  $\kappa_{eff}$  and  $\kappa_{eff,D}$ . Now that the overpotential equation is simplified and other values are assumed constant, the only unknown variables remaining are the phase potentials. The conservation of charge for the electrolyte is valid across the entire battery cell, resulting in the same number of equations as cell divisions.

However, the solid phase conservation of charge refers to only the battery electrodes and is a function of effective conductivity, solid phase potential and reaction rate [6].

$$\frac{\partial}{\partial x} (\sigma^{eff} \cdot \frac{\partial}{\partial x} \phi_s) - a_n \cdot i_n = 0 \quad (31)$$

The entire battery cell is divided into one hundred grids with 26 assigned to the negative electrode and 37 to the positive electrode resulting in a total of 163 equations representing the conservation of charge. MATLAB solves the system of equations resulting in solid phase potentials at the electrodes and the electrolyte phase potential across the battery cell. Employing the resulting phase and equilibrium potentials provides overpotential at each section across the cell. Overpotential is then used to calculate the reaction rate,  $j_H$ , by means of the Butler-Volmer Equation [5].

Convergence of the conservation of charge for the electrolyte and solid electrodes equations provides the inputs for the conservation of species equation. Using the reaction rate calculated from the initial acid concentration, the conservation of species equation outlined in Equation 37 is employed to determine the change in concentration with each time step. Similar to the method used for calculation of reaction rate, an equation for each segment or grid of the battery cell is derived. While the initial values are known, the acid concentration as a function of the change in time provides the variables for the equation. The battery cell is divided into one hundred segments, and the same number of equations represents each section. Solving the system of equations provides the acid concentration gradient across the cell as described in the flow chart in Figure 6.

### 3.2 Thermal effects

During the charge and discharge processes of a lead acid storage battery, there is a large amount of energy transfer through the battery materials. As a result, during operation, battery internal temperature cannot be assumed constant. There are number of processes that affect the amount of energy released or transferred. Specifically, the main driving forces behind chemical reactions are entropy, S, and enthalpy, H. The total change in Gibbs Free Energy, discussed in Section 2, is equal to the change in enthalpy of the system minus the product of the temperature and change of entropy for constant temperature applications as shown in Equation 32. Investigation of the free energy of the system provides the relative importance of the entropy and enthalpy terms to the entire system. In order for a reaction to be spontaneous, as in a lead acid battery, the overall free energy must be less than zero.

$$\Delta G = \Delta H - T \cdot \Delta S \quad (32)$$

Gibbs Free relates the amount of available electrical potential to the amount of thermodynamic or chemical potential. The potential for each reaction is equal to the amount of work exchanged by the system with its surroundings. Equation 33 describes Gibbs Free Energy in a constant pressure and temperature environment.

$$\Delta G = -n \cdot F \cdot E \quad (33)$$

As the amount of Gibbs Free Energy changes, the cell potential is affected. However, the simplified constant temperature calculation from the equation above is not suitable for high current battery applications. The Maxwell thermodynamic relation



provides a substitution for the enthalpy terms and results in the overall Gibbs Free Energy Equation in terms of measurable properties temperature, pressure, and specific volume.

$$dG = -S_{rev} \cdot dT + V \cdot dP + E \cdot dQ_t \quad (34)$$

Since the internal pressure of the battery is maintained at specified levels,  $dP$  and  $dQ_t$  are negligible, so the  $VdP$  term is removed from the equation to simplify the model [6]. Thermal power dissipated is described by  $T\Delta S$ . There are various processes that cause thermal power exchange or heat transfer between the constituents of the reactions. In order to fully encompass the causes for temperature change within the system, the effects of reversible and irreversible processes must be considered. The entropy of the reversible process, where there is no entropy generation, is found using the following equation where the temperature coefficient,  $\partial E/\partial T$ , of the active materials is specified in several reference materials [1, 2]. The temperature coefficient refers to the effect of temperature on cell potential. If cell potential increases as temperature increases, the coefficient is positive and vice versa. For lead acid battery cells, the lead electrode decreases with temperature increase while the positive electrode experiences the opposite effect.

$$S_{rev} = -\left(\frac{\partial G}{\partial T}\right)_p = Q_t \cdot \left(\frac{\partial E}{\partial T}\right)_p \quad (35)$$

For the irreversible processes, there is entropy generation, where energy is dissipated from the previously mentioned overpotentials. The amount of heat generated is the product of the overall current, and the total overpotential including ohmic, diffusion, and charge transfer discussed in Section 2.4 [7].

$$T \cdot S_{irr} = \eta \cdot I \quad (36)$$

Now that internal thermal effects are quantified, heat transfer between the battery components and the external environment must be considered. When the ambient temperature differs from the internal temperature, conductive and convective heat transfer takes place. Using the method of equivalent resistance a model is constructed of the battery's external surface and internal parts. The equivalent resistance is a function of the thermal conductivity, surface area and heat transfer coefficient. The plastic battery casing has a thermal conductivity of  $.2 \frac{W}{m \cdot K}$ . The thickness and surface area are calculated depending on battery dimensions. Equation 37 provides the heat transfer rate between the external environment and the internal components of the battery [3].

$$T \cdot S_{ht} = \frac{1}{R_{eq}} \cdot (T_a - T) \quad (37)$$

### **3.3 Overall Thermal Effects**

Combination of the various energy terms provides a correlation between system energy and transient temperature. The thermal power dissipated is equal to the relation of specific heat to the electrolyte mass. By setting the two equations equal, temperature change over a specified time is determined. The overall equation describing the energy in the system is shown below.

$$m \cdot c_v \cdot \frac{dT}{dt} = Q_t \cdot \left( \frac{dE}{dT} \right) \cdot T + \eta \cdot I - \frac{1}{R_{eq}} \cdot (T_a - T) \quad (38)$$

In order to accurately evaluate the change in temperature due to the thermodynamic and heat transfer effects described in the equation above the mass,  $m$ , and specific heat capacity,  $c_v$ , must be calculated [2]. The value for specific heat capacity changes with the concentration of the electrolyte solution. The concentration is constantly changing during the charge and discharge processes and is described in the units of mole/kg. Reference books provide values for specific heat capacity at various concentrations [1]. By fitting a curve to the tabular values as a function of molality (concentration), the value for specific heat capacity is calculated.

As shown in Equation 38, cell temperature is function of various chemical properties and transient battery parameters. The heat generation terms caused by overpotential and the temperature coefficient must be quantified for each cell individually. Therefore, the heat generation at the each electrode is the summation of the values across the entire volume. The summation of two heat generation rate terms at each electrode is rewritten as [7]:

$$q = \frac{1}{V_c} \cdot \int_{V_c} \sum_j a_n \cdot i_n \cdot \left( \eta - T \cdot \frac{\partial E_j}{\partial T} \right) \quad (39)$$

The total cell volume is denoted as  $V_c$ . Using the equivalent resistance method to calculate the  $R_{eq}$  mentioned above a temperature profile is established for the casing, electrode and electrolyte [3]. Employing Equation 39 provides heat generation rate in units of  $W/m^3$  and is applied over the cell volume. The model below neglects the role of the current collectors on the thermal properties of the battery and the overall temperature profile. Typical electrode structures consist of a solid lead grid surrounded by the electrode material with similar thermal properties as the electrode itself. However,

extensions from the grids connect the like electrodes to one another and deliver the current to the corresponding terminal. The collectors for the positive and negative plates are to be introduced in the more in-depth three dimensional finite element models in Section 4.2.4.

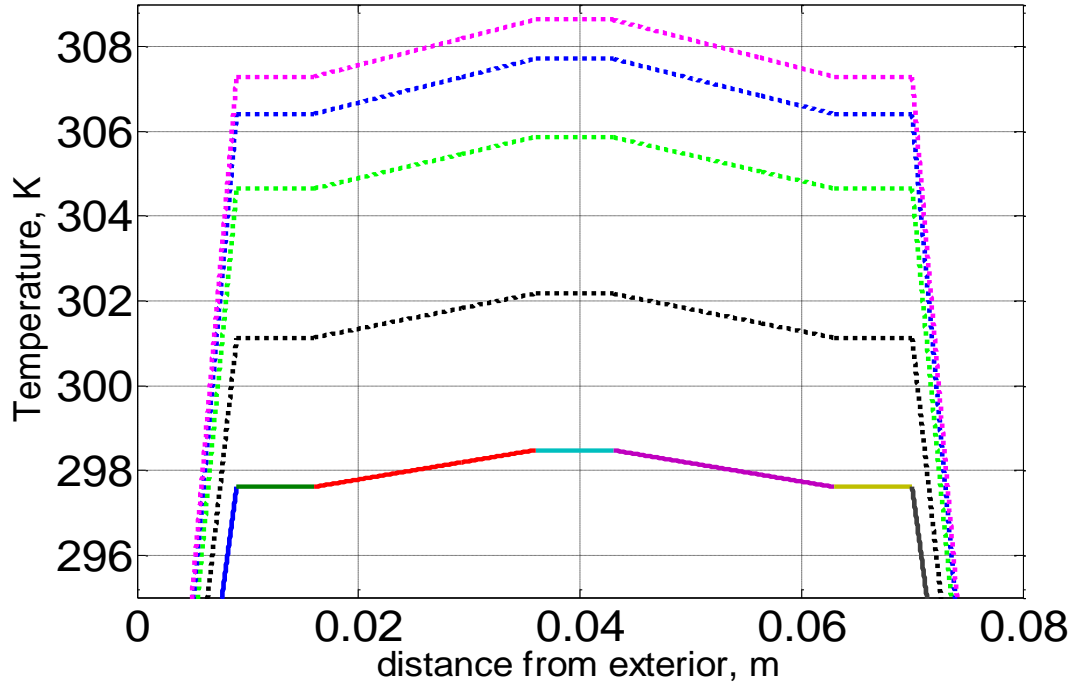


**Figure 7.** Temperature distribution for 2 cell battery at  $T_a= 273\text{ K}$  and  $T_e=298\text{K}$  for increase of 15 A of discharge current.

The result of the temperature distribution (Figure 7) shows that the highest temperature is in the center of the battery and decreases at different rates depending on the properties of the material in question. Due to the higher thermal conductivity of the electrodes the temperature across the electrode is relatively constant. However, the electrolyte reservoir shows a larger temperature range and is directly dependent on the electrode chemical process.

The heat generation and temperature are governed by principles similar to those present in the conservation of charge and species equations. The conservation of thermal energy is found by simply rearranging the previous equations.

$$\frac{\partial T}{\partial t} = q - Q \quad (40)$$

Where

$$q = \left( \frac{dE}{dT} \right) \cdot T + \eta \cdot I \quad \text{and} \quad Q = \frac{1}{R_{eq}} \cdot (T_a - T) \quad (41)$$

Investigation of the units for each of the terms above results in heat transfer rate in joules per second, J/s, or watts, W. Overpotential,  $\eta$ , is calculated as the potentials lost due to electrochemical processes of diffusion of ions and charge transfer between electrode and electrolyte. The product of the overpotential and charge or discharge current provides power units of watts.

### **3.4 Numerical Procedures**

Examination of the central equations reveal dependence of partial differential equations with respect to distance from the boundary,  $x$ , and time,  $t$ . The finite difference method is employed in order to approximate the partial derivatives of the various governing equations outlined in the sections above. Initially, the method calls for division of the domain in question into a uniform grid. For our purposes, a single battery cell is divided into a specified number of equal segments,  $\Delta x$ , for a total number of one-hundred grids. Specified by the battery dimensions, the positive electrode, negative electrode, electrolyte reservoir consist of 36, 27, and 37 grids, respectively. Utilizing

finite difference approximation, the partial derivative of phase potential with respect to  $x$  can be rewritten using the central difference method [24]:

$$\frac{\partial \varphi}{\partial x} = \frac{\varphi_{j+1} - \varphi_{j-1}}{2\Delta x} \quad (42)$$

and the second derivative as

$$\frac{\partial^2 \varphi}{\partial x^2} = \frac{\varphi_{j+1} - 2\varphi_j + \varphi_{j-1}}{(\Delta x)^2} \quad (43)$$

where  $j+1$  refers to the right adjacent grid, and  $j-1$  to the left.

By dividing the cell into grids, the conservation of charge and species equations explained in the following sections are derived for each section of the battery. The characteristics of each segment are dependent values of the two adjacent grids while the grids neighboring the boundary are set by the boundary conditions. A physical illustration of the finite difference method is shown in Figure 8, where each vertical line represents the grid boundary [24].

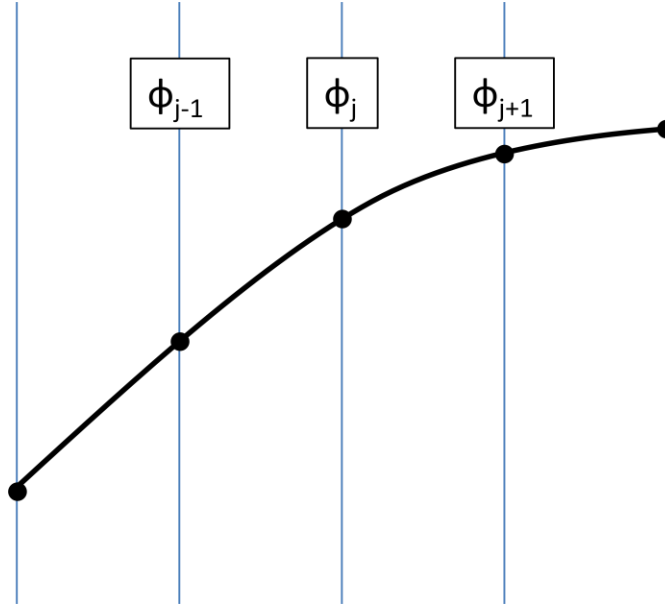


**Figure 8. Finite Difference Method example.**

Time dependent partial differential equations such as conservation of species and mass require a modified approach. As with the approach outlined in Figure 8, the concentration of each segment is dependent on the adjacent grids. However, the partial derivative of concentration,  $c$ , with respect to time is rewritten using the forward difference approach since there cannot be a negative time value:

$$\frac{\partial c}{\partial t} = \frac{c_j^{n+1} - c_j^n}{\Delta t} \quad (44)$$

In order to ensure proper convergence of the equations the concentration for each half step is employed as the average of the step in question and the proceeding time step.

$$c_j^{n+0.5} = \frac{c_j^n + c_j^{n+1}}{2} \quad (45)$$

Implementing the previously discussed conservation of species, conservation of charge, and energy balance equations the final model is constructed. Each parameter that changes with respect to time or dimension,  $x$ , is rewritten employing the finite difference approaches. As illustrated by the program structure in Figure 9 the initial and boundary conditions are set, followed by the initial convergence solving for the electrolyte and solid phase potentials. Next, employing the calculated reaction rate and overpotentials, the second convergence acts to provide the time change in concentration for a given grid.

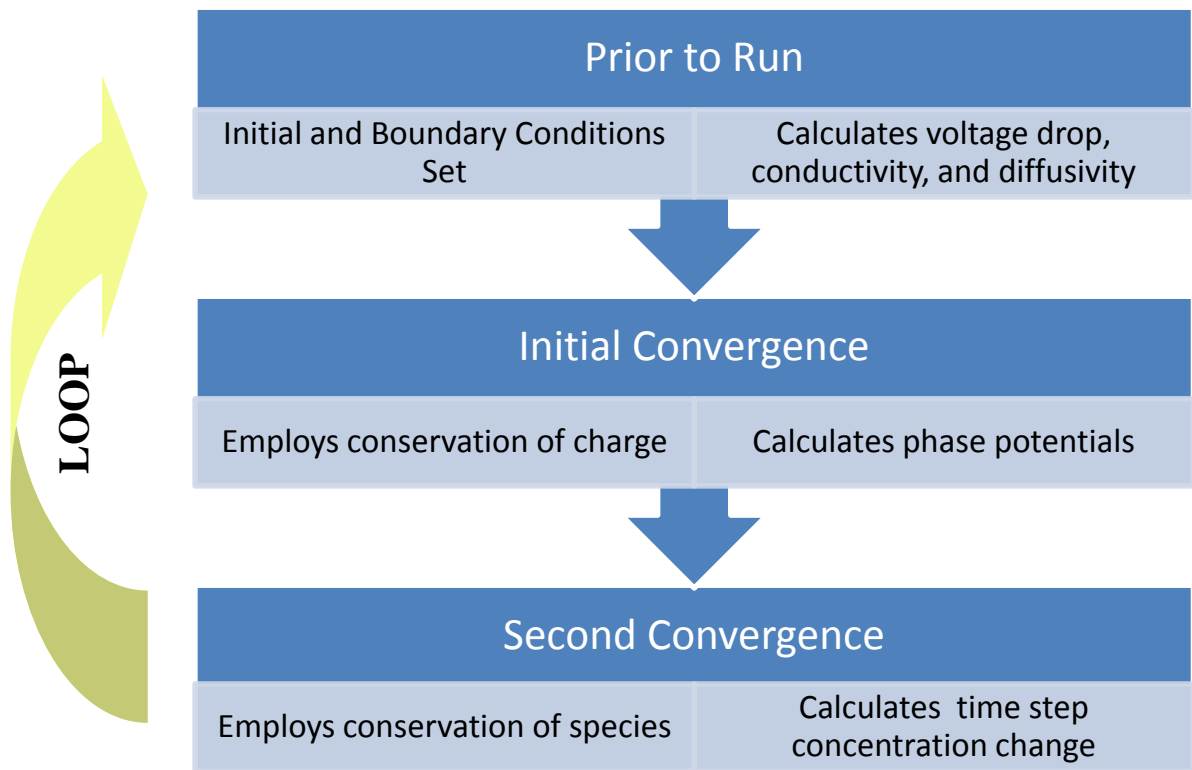


**Figure 9.** MATLAB data analysis and program structure.

As the concentrations are calculated, the values are looped back into the conservation of charge equation to determine the transient phase potentials, overpotentials, and reactions rates across the cell. The definition of cell potential,  $E_{\text{cell}}$ , is



described as the difference of the solid phase potentials of the cell boundaries as shown below [7]:

$$E_{cell} = \varphi_s|_{x=L} - \varphi_s|_{x=0} - I \cdot R_{cell} \quad (46)$$

## 4 MODELING RESULTS

The computer modeling efforts aim to fully represent battery performance under various discharge, charge, and temperature ranges. However, performance is dependent on complex electrochemical processes that determine electrolyte concentration, reaction rate, conductivity, etc. In order to recognize the causes of inconsistent response under varied conditions, researchers must first examine the response of these complex processes. An illustration of data interaction between MATLAB, finite element analysis, and experimental data is provided below.

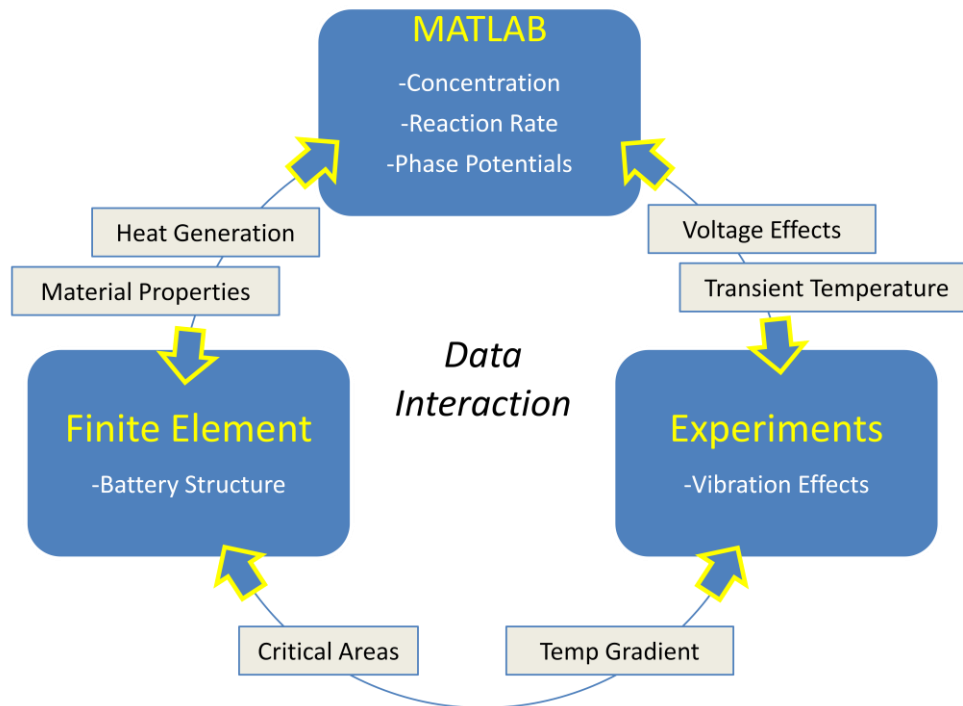


**Figure 10.** Data Interaction.

## **4.1 Isothermal Modeling**

Prior to the investigation of transient temperature effects on battery performance, a thorough understanding of battery electrochemistry under isothermal conditions is vital. The load or supply current is the major factor determining battery kinetics and the rate of chemical processes. This section provides an intense investigation into response of reaction rate, overpotential, and porosity including their effects on electrolyte concentration and cell voltage.

### **4.1.1 Overpotential and Reaction Rate**

Overpotential and reaction rate are identified as the most critical parameters for accurate representation of battery performance. Specifically, overpotential for each electrode grid determines the frequency and reaction rate, at which the chemical reactions take place. As the overpotential at that point increases, so does the reaction rate. While the magnitude of reaction is heavily dependent on the overpotential, the electrode effective surface area plays a significant role. Surface area is constantly changing as active materials are depleted while the electrodes become increasingly or decreasingly porous depending on the process and are calculated using the ratio of available capacity to maximum capacity discussed in Section 2.4.

The exchange current density has a similar response, but is proportional to electrolyte concentration as shown below [3].

$$i_n = i_{n,max} \cdot \left( \frac{c_e}{c_{e,max}} \right)^\delta \quad (47)$$

The correction factor,  $\delta$ , is .3 and 0 for the positive and negative electrodes, respectively. Therefore, the negative electrode current density remains constant regardless of electrolyte concentration. Conversely, the positive electrode current density increases during charge as the concentration approaches the maximum and decreases during discharge.

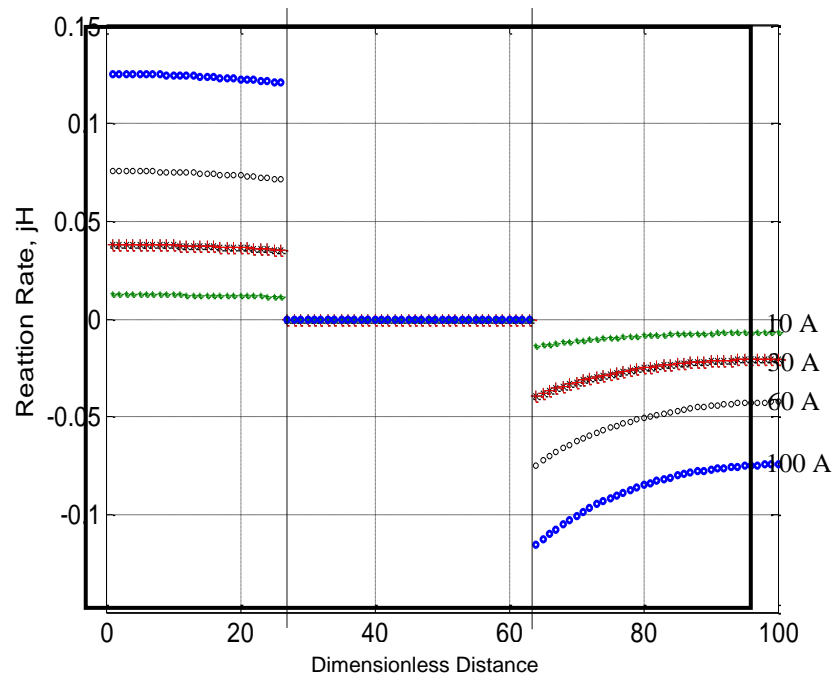


**Figure 11.** Isothermal reaction rate, A/cm<sup>3</sup>, after 15 minute discharge at 10A (.), 30 A (\*), 60 A (o), 100 A (o).

Investigation of modeling results show temperature of the battery environment and current applied or drawn from the battery exhibit significant effects on the reaction rate. As expected, when the current is increased, the reaction rate speeds up to accommodate. There is also a considerable gradient created across the electrodes as more reactions occur at the electrode/electrolyte interface increasing with current as shown in Figure 11. The reaction rate across the negative electrode is relatively uniform as the

current density remains constant over the entire range of concentrations. However, the positive electrode reveals a steeper gradient due to the current density dependence on concentration illustrated by Equation 47.

While applied current has a considerable effect on performance, everything from the electrolyte conductivity to reaction and diffusion rates is a function of temperature. Therefore, variation in temperature affects the amount and location of the chemical reactions during battery operation. On the molecular level, temperature increase causes a rise in particle collision leading to a rise in reactions across the cell.

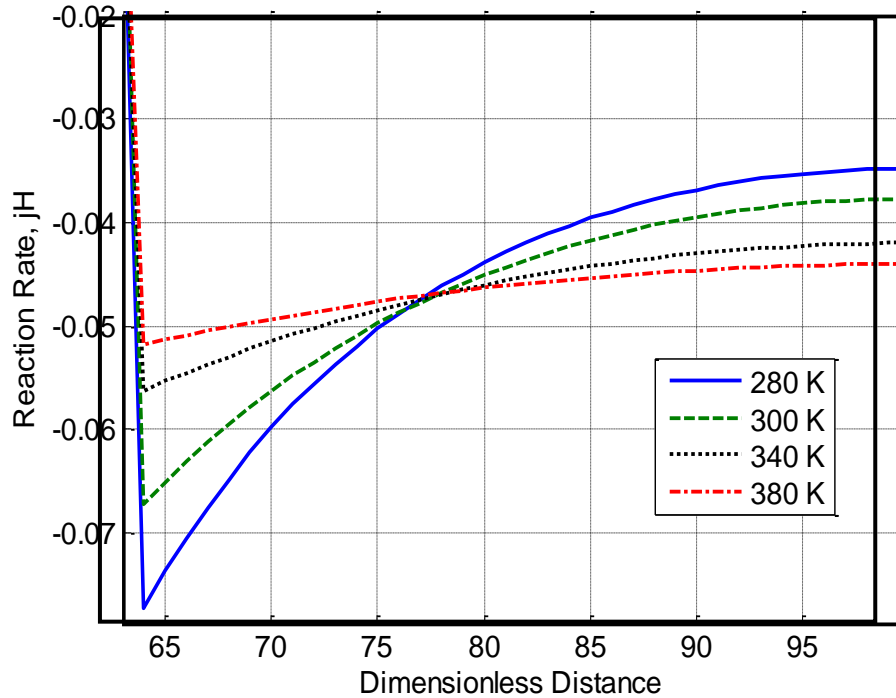


**Figure 12.** Reaction rate of the positive electrode after 15 minute discharge at 30 A and 280 K (solid), 300 K (dash), 340 K (solid dot), and 380 K (dash dot).

Most notably, as temperatures increase reactions occur uniformly across the cell resulting in decreasing gradient as temperature rise. Conversely, as the temperature

decreases a greater percentage of reactions occur at the interface causing a significant gradient across the electrode. Intuitively, as the reaction rate grows increasingly uniform across the electrodes so should the electrolyte concentration.

### **4.1.2 Electrolyte Concentration**

Initially under equilibrium conditions, the electrolyte concentration is assumed constant across the battery cell. During charge or discharge process, ions diffuse towards and away from the electrodes to react at the electrode/electrolyte interface. Ion diffusion along with continuous chemical process causes differing electrolyte concentration across the battery cell. Various parameters, mostly determined by charge or discharge current and temperature, greatly affect the degree of concentration change [9].

As the battery is discharged, the electrolyte concentration decreases at a rate determined by the load applied. However, constant current does not expend the electrolyte at a constant rate, as the reaction rate is constantly changing due to a number of factors. Figure 13 shows acid concentration across the battery cell following fifteen minutes of continuous discharge at 10 A, 30 A, 60 A, and 100 A at room temperature, 300 °K. For each case, the battery is initially at full charge with a uniform acid concentration of 5.6 mol/cm<sup>3</sup>.

During discharge, as the electrochemical processes occur, the electrodes react with the electrolyte decreasing the overall amount of electrolyte present as water takes place of the displaced sulfuric acid. Non-uniform concentration occurs for a number of reasons. The porosity of the electrodes is determined by the electrode material properties and chemical reactions continuously altering the structure, specifically surface area, and

chemical makeup of the electrode interface. Inconsistency of effective surface area, effective current density, and reaction rates at the interface results in a significant slope as shown below. The electrolyte concentration grows increasingly uniform as temperature rises consistent with the reaction rate shown in Figure 11.

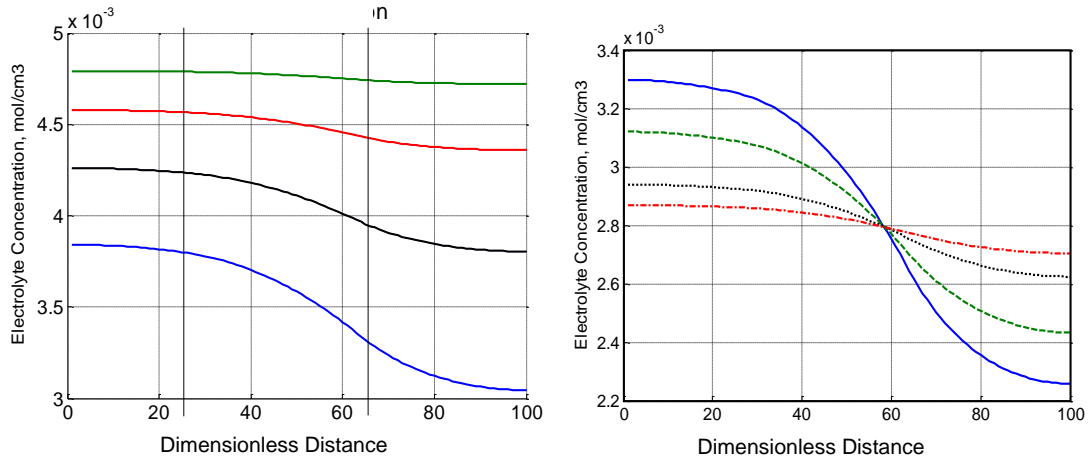


**Figure 13.** (Left) Acid concentration gradient, mol/cm<sup>3</sup>, after 15 minute discharge at 10A (g), 30 A (r), 60 A (b), 100 A (blue). (Right) Acid concentration gradient, mol/cm<sup>3</sup>, after 15 minute discharge at 60 A for various isothermal temperatures.

These findings are consistent with the profile provided in Figure 12 showing a greater number of reactions at the electrode/electrolyte interface. Consequently, the minimum acid concentration occurs at the positive electrode boundary where the least amount of reactions takes place. While the magnitude of current determines the gradient, the average acid concentration is more affected by the battery SOC than the current drawn from the battery. Additionally, the load current directly influences the reaction rates and SOC. In other words, acid concentration depends on the amount of time a battery is under a certain load as the gradient increases over time. Even when under a constant discharge current the gradient grows increasingly steep as shown in Figure 14 where time increases from back to front along the bottom axis.

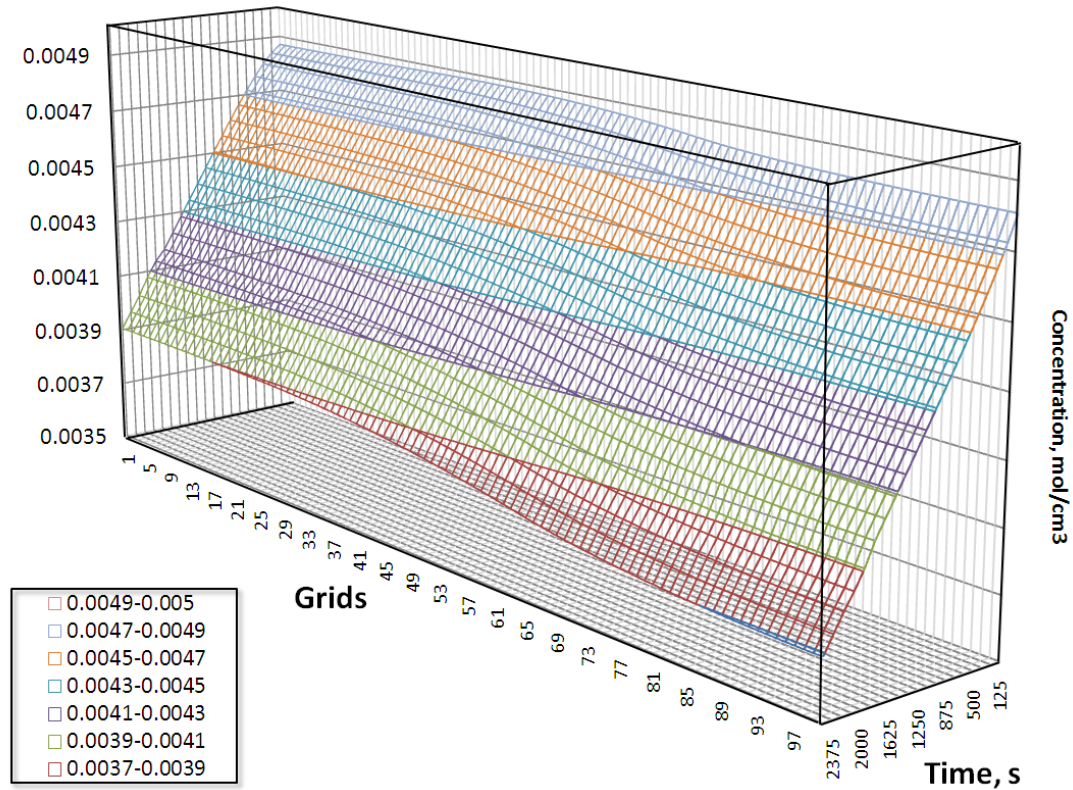


**Figure 14.** One dimensional electrolyte concentration for 30 A discharge.

It is important to note that the minimum acid concentration always occurs at the positive electrode as pictured in Figure 14. As a result, during discharge the positive electrode controls the electrochemical performance. When the acid concentration at the positive electrode is completely depleted, the battery is considered fully discharged or SOC equal to zero [9]. However, during charge, when the current flows in the opposite direction, the gradient has the opposite slope where the minimum concentration occurs at the negative electrode. The figure on the left shows increasing gradient as a greater charge current is applied, consistent with discharge results. Furthermore, the temperature has similar effects on the concentration growing increasingly uniform as temperature rises from 280 K and 380 K as shown in Figure 15.



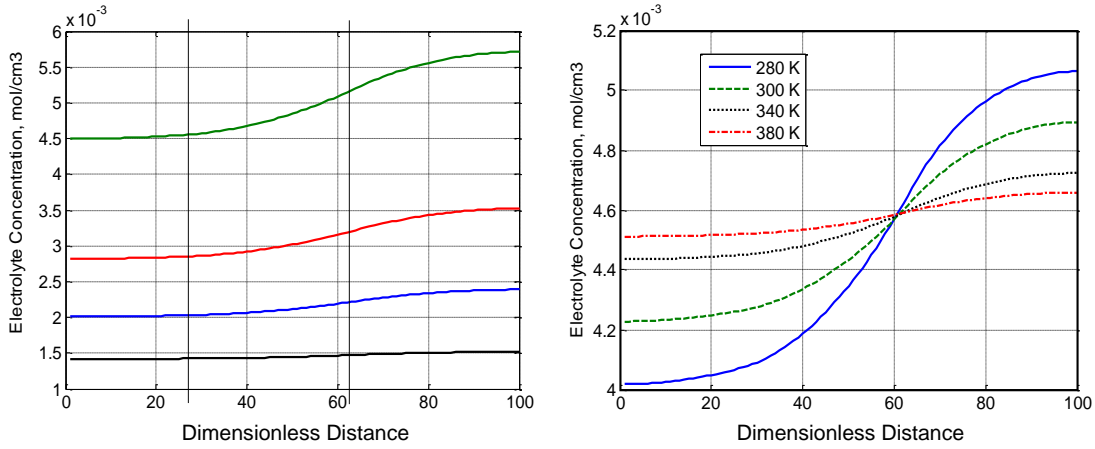


**Figure 15. (Left) Concentration gradient, mol/cm<sup>3</sup>, after 30 minute discharge at 5 A, 20 A, 40 A, and 80 A. (Right) Acid concentration gradient, mol/cm<sup>3</sup>, after 30 min charge at 45 A from 50% SOC at various isothermal temperatures.**

Acid concentration directly determines the voltage experienced at the terminals under load as shown in Figure 13 and 15, but also when the load is removed and the battery is at rest. The amount of voltage recovery discussed in Section 2.7 is mostly determined by the load magnitude of the load removed from the battery. However, the electrolyte concentration slowly regains a uniform equilibrium state after the load is removed and the terminal voltage is affected. An example of this process is described in Figure 16, as the electrolyte concentration gradient decreases when the battery is at rest after a 50 A discharge load is removed. After 1000 s have passed a significant change in concentration occurs, and after 1500 s the electrolyte regains an equilibrium state.

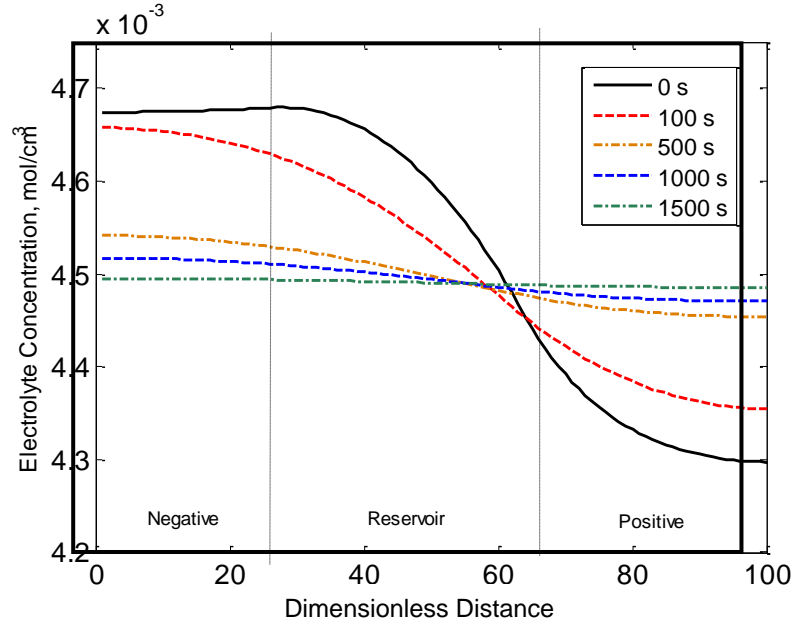


**Figure 16.** Electrolyte concentration 0 s, 100 s, 500 s, 1000 s, and 1500 s after load is removed.

### 4.1.3 Phase Potentials

As expressed in the previous equations the electrolyte and solid phase potentials are directly determined by the electrochemical kinetics described by the material balance, charge balance, and Darcy equations. The matrix constructed using the finite difference approach converges in order to calculate the phase potentials across the cell. The electrolyte phase potential is a resultant of the conservation of charge across the cell while the solid phase potential only occurs at the solid electrodes. Since the current collectors are attached at the electrode boundaries, the cell potential which is delivered to the battery terminals is determined by the solid phase potential at the point of contact between the electrodes and current collectors. As pictured below in Figure 17, the solid phase potential at the electrodes remains constant across the thickness of each.

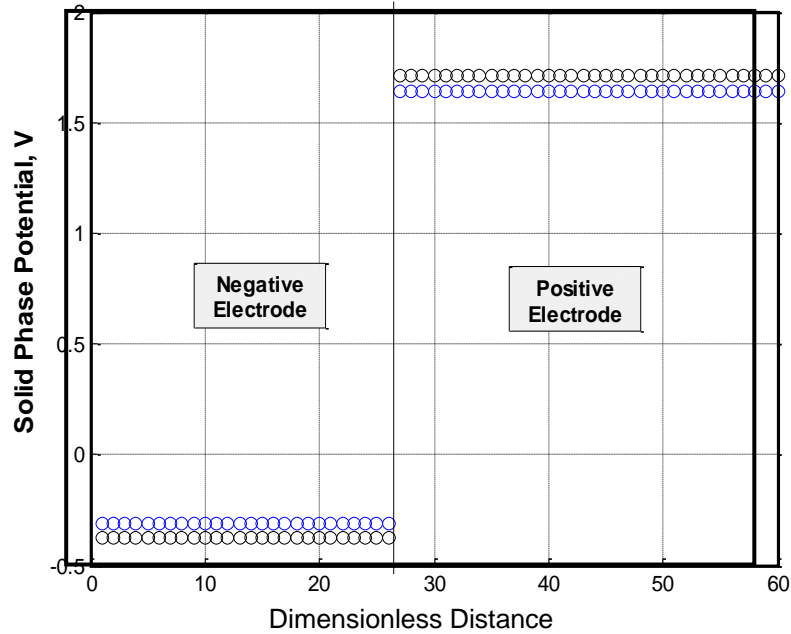


**Figure 17. Solid Phase Potential. (Black) Response after 500s of 30 A discharge. (Blue) Response after 1200s of 30 A discharge.**

The cell potential is a function of acid concentration at each electrode. As expected, the solid phase potential decreases for both electrodes during discharge as the concentration at each lessens causing a decrease in overall cell potential. When the concentration gradient arises the electrolyte phase potential experiences a significant gradient across the cell during the discharge process. This variation directly influences solid phase potential as the system of equations solves for each simultaneously. The negative electrode is specified as the reference electrode since the electrolyte phase potential at the boundary remains zero throughout the various processes as shown in Figure 18.

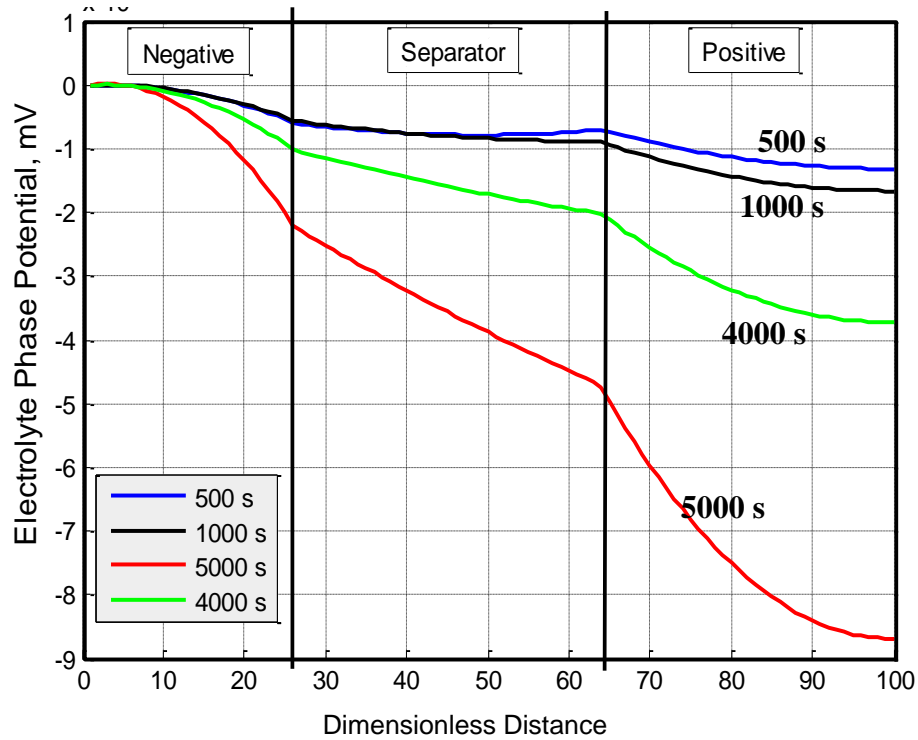


**Figure 18.** Electrolyte phase potential for 60 A discharge.

As the battery is discharged, the rest of the cell shows an increase in gradient for the potential revealing an almost linear relationship across the electrolyte reservoir as shown above. Furthermore, the gradient grows increasingly steep as discharge continues dramatically changing near the end of discharge due when internal resistance substantially rises. The change in the phase potential directly affects electrolyte concentration, effective conductivity, and diffusivity present in the conservation of charge equations. However, for most instances the solid phase potential is much greater than the electrolyte phase. As a result, the electrolyte phase potential effect on the overpotential becomes negligible.

The ultimate result of the battery kinetics outlined in the modeling results determines the voltage experienced at the terminals, which is defined as the difference in

the solid phase potentials at the boundaries. However, the phase potentials are a function of various parameters and material properties that change at different rates determined by the load applied and operating conditions. Additionally, the relationship between acid concentration and electrode potential provided in Equations 26 and 27 do not provide adequate representation for all conditions. The values provided by this equation assume an isothermal system at 300 °K, and the potential values correspond to that temperature. However, the potential at each electrode is temperature dependent and is governed by the temperature coefficients. The first temperature coefficient is related to entropy change of the chemical reactions present, while the second temperature coefficient is dependent on the specific heat of the components. Curve fitting to tabular values provides the temperature coefficients at various electrolyte concentrations. Once the coefficients are determined, the following equation is employed to calculate cell voltage at the instantaneous temperature.

$$E = E_{300K} + (T - 300^{\circ}K) \cdot \frac{dE}{dT} + (T - 300^{\circ}K)^2 \frac{d^2E}{dT^2} \quad (48)$$

Typical discharge curves for 1C, 2C, 3C, and 4C discharge currents as output by the MATLAB model illustrate the linear decrease followed by an exponential drop near the end of discharge (Figure 19). The curves have different initial potentials due to the increase in voltage drop with current.

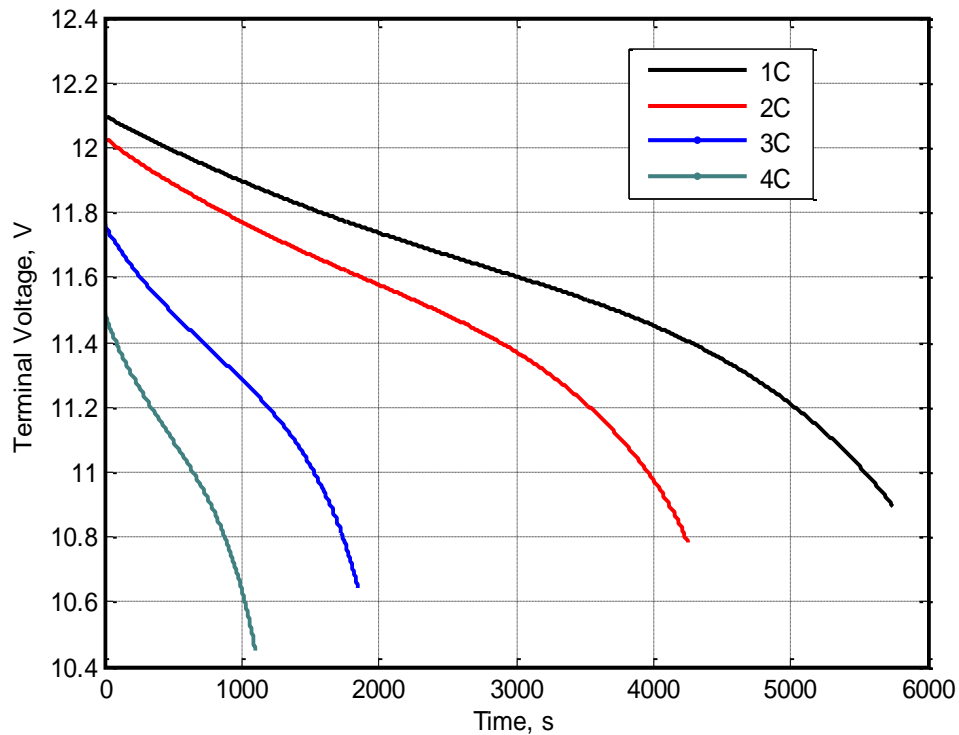


**Figure 19.** Discharge curves for 12 V lead acid battery under various loads.

#### 4.1.4 Porosity and Effective Surface Area

While the isothermal effects discussed above are mostly dependent on the applied currents effect on the discharge rate and depth of discharge, porosity values are a function of number of cycles and electrode material properties in addition to the discharge rate and depth of discharge, DOD. Certain battery models assume porosity as constant, but that is not appropriate.

The material properties of each component show significant degradation over time as the battery is cycled. Therefore, approximations of electrode properties must be made. Specifically, the porosity calculation has great importance as it determines the amount of effective surface area available for chemical reaction. As described in Section

2.3, the porosity of the separator is assumed constant throughout each process, while the porosity of each electrode is assigned an initial state.

During the discharge process, the negative electrodes grow increasingly porous allowing for a larger effective surface area. Conversely, the positive electrode becomes less porous due to the negative reaction rate. Although, there are only small changes to the porosity during both the charge and discharge process, minimal change in the effective surface area has a significant effect on battery performance. Therefore, determining the precise porosity prior to current load is essential to obtaining an adequate response from the model. Figure 20 illustrates the effects of minimal variation to the initial porosity of each electrode. Five cases are investigated, where the black solid line indicates the response of model employing the manufacturer specified porosity values. The dashed lines show the effects of increased porosity and the solid red and blue lines are a result of decreased porosity under a constant load.

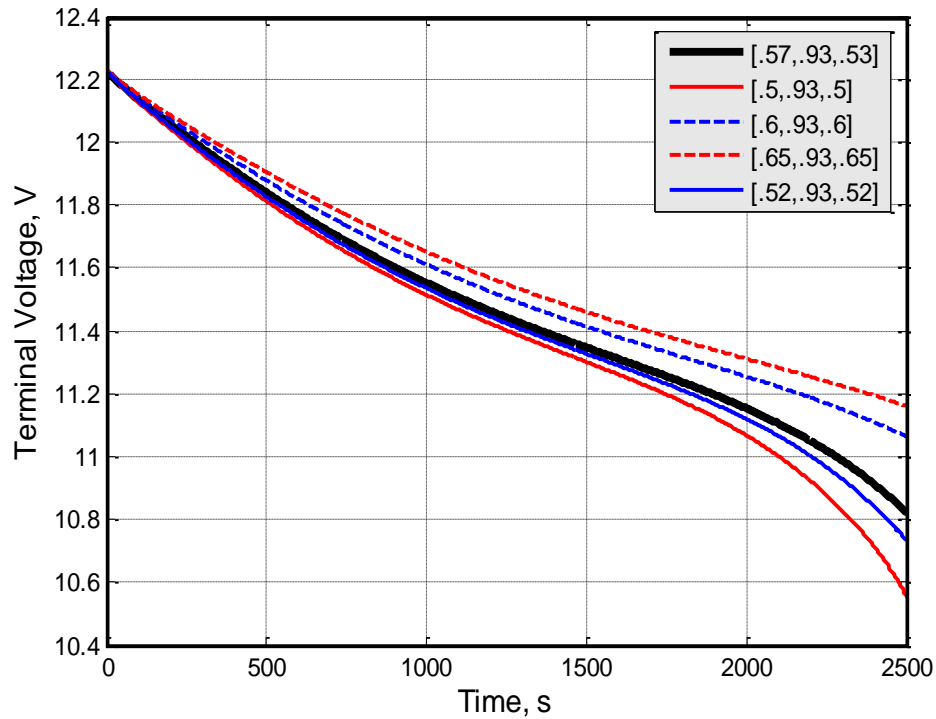


**Figure 20.** Initial porosity parameter effects for 60 A discharge.

The effects of only slight variations in porosity validate the modeling method of employing transient porosity. Using the partial differential equations for the conservation of species, as the porosity is assumed higher, the concentration gradient decreases as electrolyte fills the porous areas aiding the battery's ability to hold charge.

## 4.2 Temperature Effects

Initial thermal effects were derived using a simplified model neglecting the effects of heat generation and convection with a purely isothermal representation. The transient thermal model attempts to merely quantify the amount of energy generated, dissipated, and transferred between the battery components as a means to determine the average temperature of the cell in order to model battery performance. In addition,



control volumes of the casing, positive and negative electrode, and electrolyte reservoir are implemented and constructed as a three dimensional model investigating temperature distribution. For our purposes, the battery is first modeled as a closed system where no heat is lost or added to the system. Secondly, a non-adiabatic system, where heat transfer with the external environment is considered, is modeled using the same principles discussed in the previous section. The amount of heat generation is extracted from the MATLAB model and implemented during finite element analysis.

#### **4.2.1 Constant Current Temperature Response**

There are a number of charge and discharge methods employed for automotive battery applications. Although the battery experiences various discharge rates during operation, there are instances when the load on the battery remains constant. Throughout the driving cycle the battery is constantly interacting with the alternator to provide sufficient current to the electrical components of the vehicle. Simply, the alternator acts to convert mechanical energy to electrical energy. Typical commercial alternators are rated to supply a maximum of 80 to 100 amps [25]. For the most part, the interaction of the battery and alternator occurs in two ways. There are times when the alternator needs assistance to provide the necessary current to power the on-board electrical devices. During the high pulses of load on the alternator, the lead acid battery provides the additional power. Excluding the isolated cases, the alternator and voltage regulator charge the battery at relatively low current levels.

Immediately after cranking draws a substantial load from the battery, the alternator provides up to 45 A of quick charge for a very short period in order to prevent

capacity losses. At no other time will the battery be subjected to such a high charge current. As a rule, lead acid batteries are not charged above 25 % of their capacity preventing detrimental corrosion of the electrode grids and gas evolution. For instance, a 100 A-h battery has a maximum charge acceptance of 25 A without any significant damage.

Using thermodynamic principles discussed in Section 3.2 involving various sources of heat generation, the average cell temperature is calculated. The figures below illustrate cell temperature during 60 A and 100 A discharge for the adiabatic and non-adiabatic cases. The temperature during operation reveals similar response increasing at nearly a constant rate for the adiabatic case, and steadily decreasing over time for the non-adiabatic case.

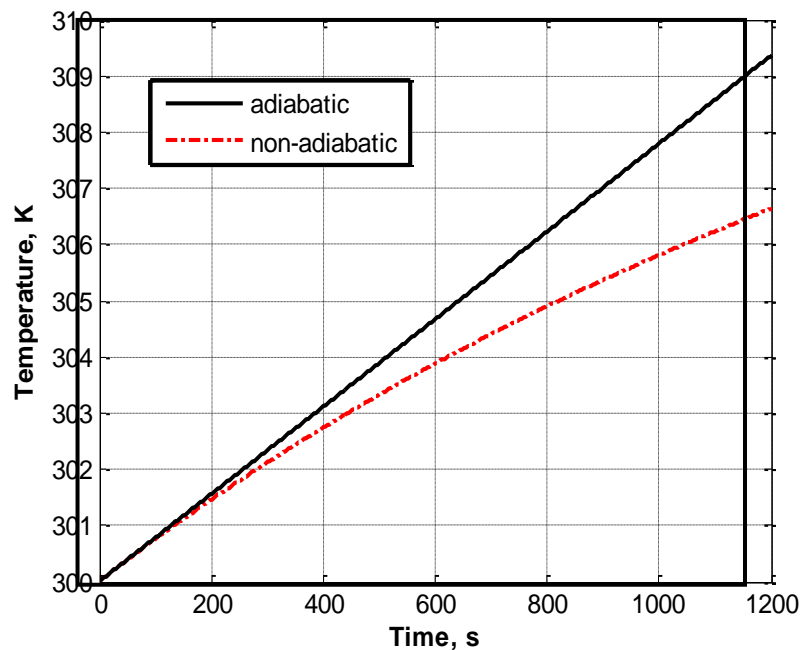


**Figure 21.** Temperatures for a 60 A charge. Adiabatic, solid line, non-adiabatic, dashed line.

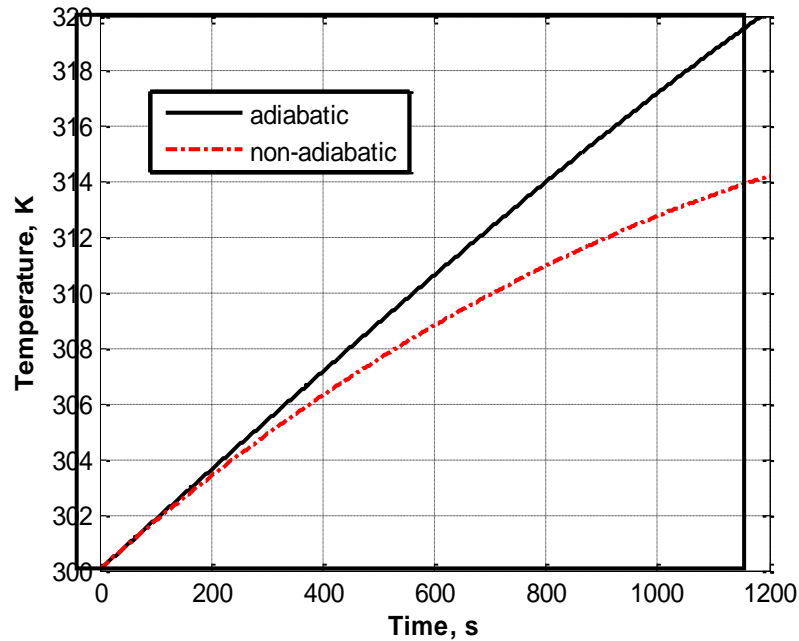


**Figure 22.** Temperature for a 100 A charge. Adiabatic, solid line, non-adiabatic, dashed line.

There is a significant increase in temperature during the discharge process. For the extreme case of 100 A the temperature increased 20 °K, and 10 °K for the other case pictured above. The temperature dependence of the governing equations causes a significant change in the reaction rate at the electrodes as shown in Figure 12. As reaction rate grows increasingly uniform at high temperatures so does the concentration. Isothermal conditions maintain a temperature of 300 °K throughout the discharge process while the adiabatic and non-adiabatic systems include heat generation effects caused by ohmic and electrochemical overpotential, as well as reversible heat generation governed by the temperature coefficient of the electrodes.

Several of the parameters and governing equations that determine battery performance are temperature dependent. On the molecular level, the diffusion of ions

and ionic conductivity of the electrolytes establish electrolyte concentration and both are a function of temperature. Increase in ionic conductivity allows ions to move more freely through the medium, while the diffusion coefficient determines the speed at which ions diffuse to areas of lesser concentration. As shown, in Figure 23, ionic conductivity and diffusivity significantly increase as temperature rises leading to a lesser gradient during the charge and discharge processes.

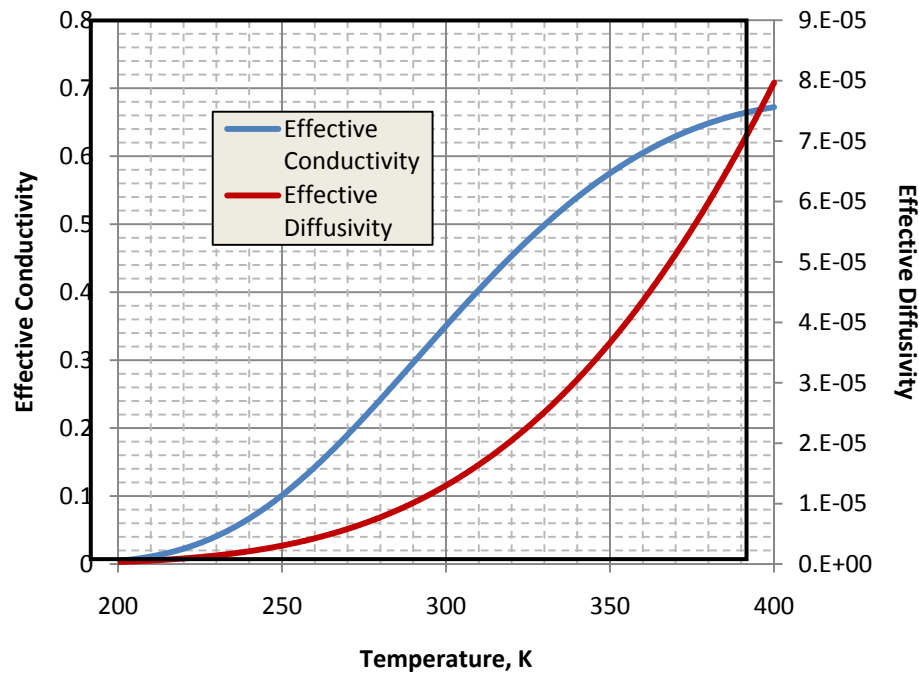


**Figure 23. Coefficient temperature dependence.**

The effects of temperature increase on the electrolyte concentration are evident for the three cases illustrated in Figure 24. The adiabatic and non-adiabatic cases show an increase in temperature from the isothermal simulations leading to elevated electrolyte ionic conductivity and diffusion rates. Although increased temperatures act as a catalyst

to chemical reactions, the batteries actually discharge slower as the lesser gradient aids in the battery's ability to hold charge or capacity.

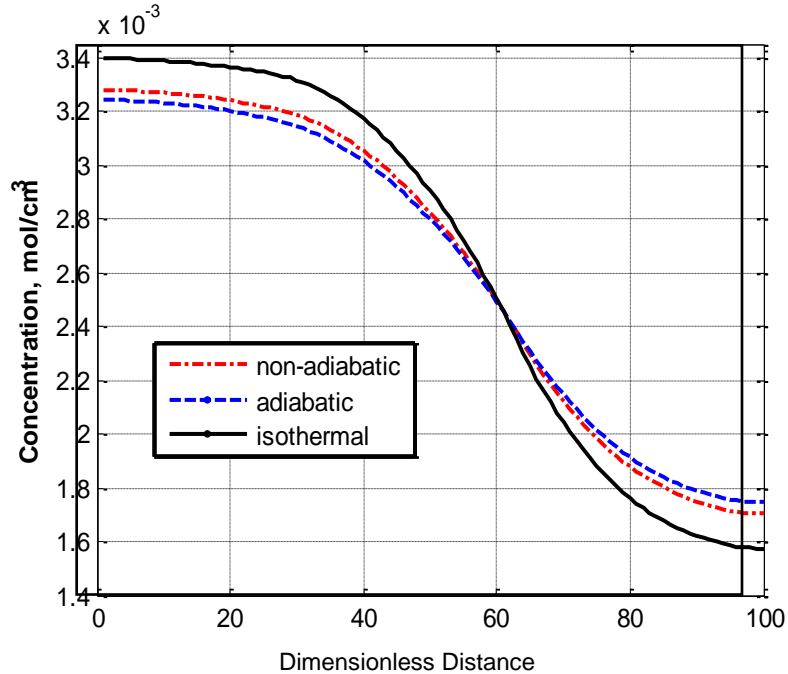


**Figure 24. Electrolyte concentration for isothermal, adiabatic, and non-adiabatic models after 150 A discharge for 1200s, with initial temperature 300 K.**

As expected the highest temperatures occur during adiabatic process with no heat transfer to the external environment leading to lowest concentration gradient across the battery cell as shown in Figure 24 as the amount of reactions near the interface is comparable to reactions within the porous cells. The lower concentration in certain areas is due to lower reaction rates and an increase in diffusion rate at higher temperatures. Although the difference in concentration between the three cases is evident, obvious effects to the discharge performance is only significant at high currents and extreme temperatures some time after the initial load is exerted. In addition to transient effects, extreme temperatures high and low greatly affect the available capacity even at rest.

At elevated temperatures, chemical reactions take place at a greater rate, but also increase ionic conductivity and diffusion rates. This fact is illustrated by the isothermal, adiabatic, and non-adiabatic cases below. Initially, when the temperatures are relatively close, the discharge performance is similar. The discrepancy between the cases is caused by the temperature coefficient which determines cell voltage as a function of temperature. However, after 600 seconds as the temperatures continue to rise, there is a significant difference in terminal voltage. Near the end of discharge the voltage is .1 volts more when compared to the isothermal case at 300 °K.

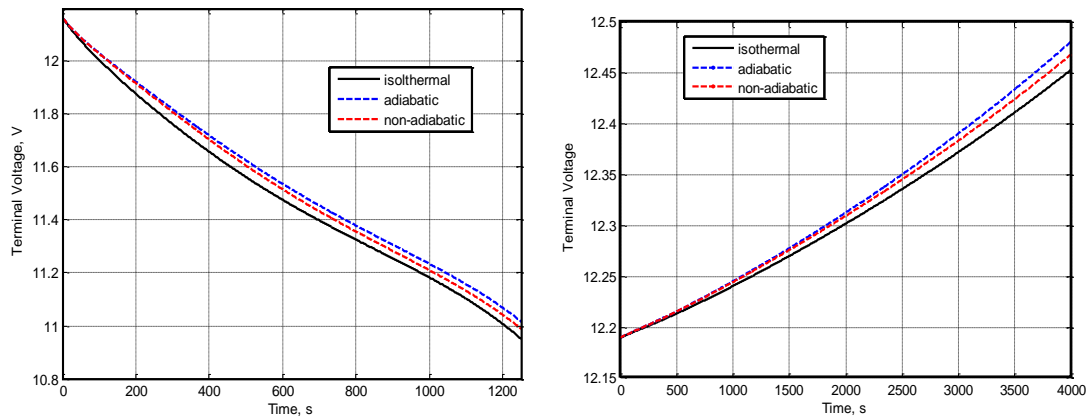


**Figure 25. (Left) Discharge for 100 A. (Right) Charge for 15A or .25C for 60 A-h battery. Solid line, isothermal, dotted line, adiabatic, thick line, non-adiabatic.**

The same effect holds true during charge as the temperature grows over time the cell voltage increases compared to the isothermal case. However, due to low charge currents the amount of temperature change is not large enough until well after the initial supply current is applied to show a considerable change.

### 4.2.2 Dynamic Current Effects

The charge and discharge current profiles depend on the type of vehicle and the rated voltage or currents of the vehicle electrical system. In addition, there are a number of methods used to properly charge a battery that is controlled by the battery management system of the vehicle. Lead acid batteries charge current is held below the maximum .25C or one-fourth of the rated capacity. Currents exceeding this accepted value have negative effects on the battery capacity and ability to hold charge [25]. Various charging and discharge methods include but are not limited to: constant current, constant voltage, trickle charge, and float charge. The most appropriate method is determined by the frequency of charging, battery configuration (series, parallel, etc.), susceptibility to gassing, and vehicle application. In order to investigate the different charge methods, ramp and step current cycles are input into the model to study the effects on the internal temperature of the cell. When the input current is varied, the rate of entropy change and the overpotentials at the electrodes is constantly changing. As a result, the rate of change in temperature greatly differs from the constant current modeling completed in the previous sections as heat generation decreases or increases depending on the ramp slope. The change in current and temperature both have an effect on the voltage experienced at the terminals. The response under common step and varied ramp inputs is provided in Figure 26 below.

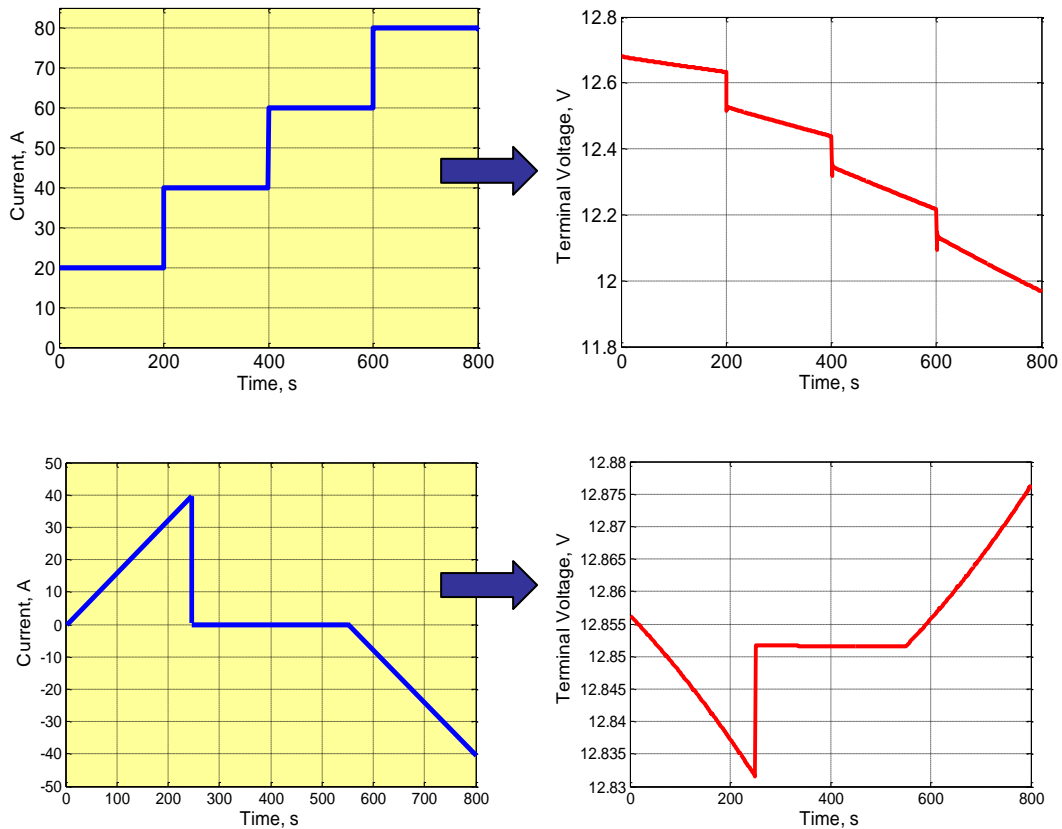


**Figure 26.** Terminal Voltage response to dynamic current.

The step inputs cause a voltage drop equal to the increase in current multiplied by the internal resistance as discussed in Section 2.6. Since the current is increased by 20 amps for each step, the voltage drop for each is the same. The second example employs an increasing discharge current followed by a period of rest, then increasing charge current. The MATLAB model views positive current as discharge and negative current as charge, because during these processes the current has the opposite flow direction. After the load is removed the voltage recovers and then increases as the battery is charged. Also, it is important to note that the terminal voltage decreases at an elevated



rate as the current increases during discharge, and has the opposite effect for charge current.

In addition to the profiles in Figure 26, an increasing ramp current was applied as shown in the figure below resulting in the temperature change over time illustrated in Figure 27. The positive and negative ramp currents are pictured below on the left, and the right side illustrates the temperature change over time.

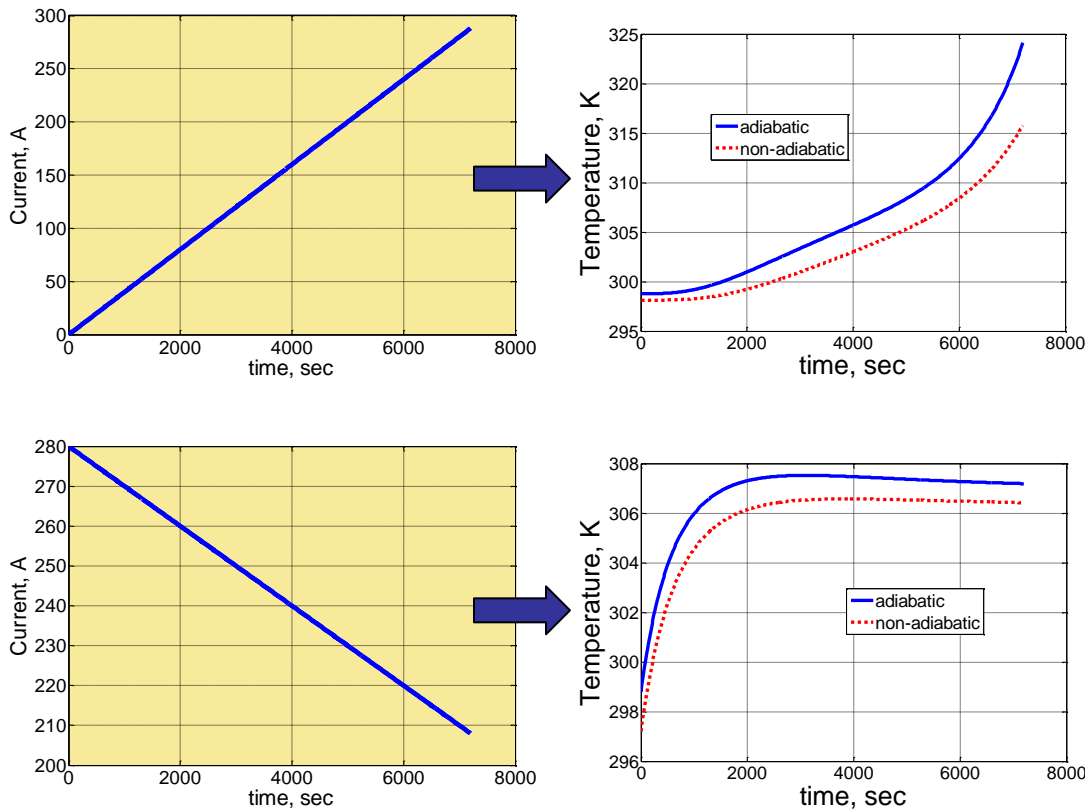


**Figure 27.** Ramp input temperature response.

The results are fundamentally consistent with accepted knowledge of battery performance. At very high current rates, the temperature increases very rapidly. However, at low currents the temperature tends to slowly increase, finally coming to a settling temperature. Automobile starter motors are designed to deliver a high current for

a short period of time during ignition. The average internal cell temperature calculated by summation of the heat generation within the control volume provides suitable inputs for representation of electrochemical processes. However, to fully understand the thermal profile created as chemical reactions continuously occur within the battery cell, a comprehensive finite element model incorporating various material properties of battery components is necessary.

### **4.2.3 Two Dimensional Finite Element Analysis**

In an effort to validate the results of the thermal MATLAB modeling, finite element analysis allows researchers the ability to assemble a more visual model of the system. Constructing a model of the battery cells requires an in-depth understanding of battery manufacturing. First, the electrodes are composite lead material formed around a lead antimony grid that provides longer life and improved performance. Once the electrodes are processed, they are connected using current collectors made of solid lead or copper. The current collector electrode configuration then incorporates separators between the opposing electrodes to prevent electrical shorts. Once the separators are in place, the current collectors are connected to the terminals and placed in the plastic casing. Lastly, a sulfuric acid water mixture is added between the positive and negative electrodes leaving the appropriate space above the cells to complete the battery construction [8].

Finite Element Software modeling, including ANSYS and ProEngineer (Pro/E), uses specified nodes to create very simple two dimensional models to carry out basic analyses of a system similar to the grids employed in the MATLAB model. In order to

accurately address the thermal effects on the battery, a comprehensive three dimensional model will provide a better understanding of the critical areas of the battery during charge and discharge. The model constructed in Pro/E is imported into the ANSYS workspace to observe the effects using the initial condition consistent with the MATLAB and 2D ANSYS model. As the battery is discharged, the transient temperature profile will be constantly changing, forcing snapshots of the thermal effects to be extracted for comparison with experimental and modeling results with the use of equipment discussed in later sections. Additionally, thermal imaging technology will be incorporated to act as a snapshot using the same conditions applied to the model.

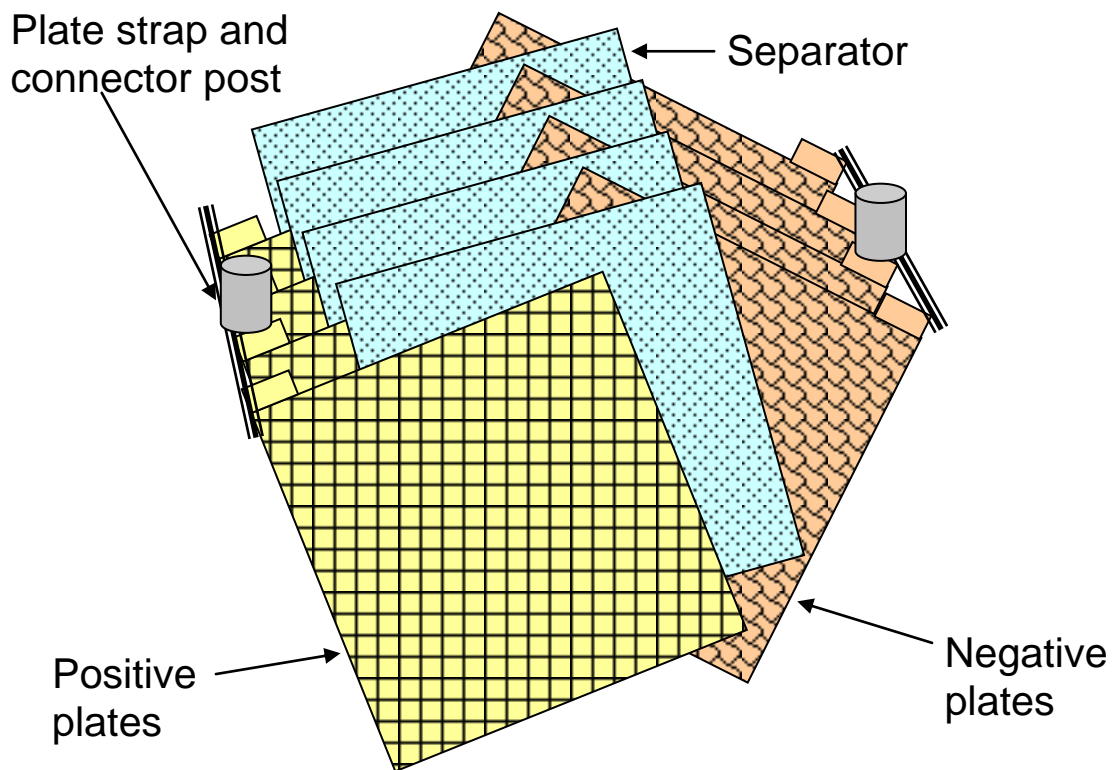


**Figure 28.** Electrode, separator, and current collector configuration.

Investigation of battery electrochemistry within the cells reveals the critical areas for thermal effects and battery degradation. For instance, the battery electrode/electrolyte interface where the majority of the chemical reactions occur is of great concern. Once the critical areas are established, the material properties of the electrode, electrolyte, separator, and casing were obtained from various references [1, 2]. ANSYS and ProE finite element software allows for user specification of material properties including thermal and electrical conductivity, density, and specific heat capacity. However, material properties such as the ones listed above are temperature dependent. In order to address the variation, ANSYS allows for a table of values for each property compared to their corresponding temperature. ANSYS extracts the materials property matching the value to the instantaneous temperature of the node in question. The material properties of specific battery components at room temperature, 300 °K, are provided in Appendix A.

Initially, a simple single cell was constructed with a polyethylene case incorporating the positive and negative electrodes. The thermal and electrical conductivity, density, and specific heat capacity was specified for each of the battery components. Additionally, initial conditions for the internal and external temperatures were set to 300 °K. In order to quantify the effects of heat transfer with the external environment, convection is set for each of the external surfaces of the battery casing. Heat generation, a result of reversible energy change and ohmic irreversible effects, is applied to the electrode/electrolyte interface for both the anode and cathode. The overall heat generation,  $q$ , for each electrode is a function of the overpotential, temperature coefficient,  $dE/dT$ , and applied or discharge current [7].

The first term in Equation 39 is a result of reversible entropy change where the current direction determines the sign while the second term stems from irreversible effects and is always positive [7]. The temperature coefficients determine whether the electrode increases or decreases with increasing temperature and are temperature dependent. Therefore, a table of temperature coefficients and corresponding temperatures are inserted into the material properties for ANSYS modeling. Since heat generation occurs along lines of a two-dimensional model and the electrodes with differing thermal properties experience varying heat generations, a temperature profile is created across the battery cells decreasing towards the outer casing. A type of lead acid battery design incorporates a cell stack with four positive electrodes and three negative electrodes. The temperature distribution of this arrangement is illustrated below in Figure 29.

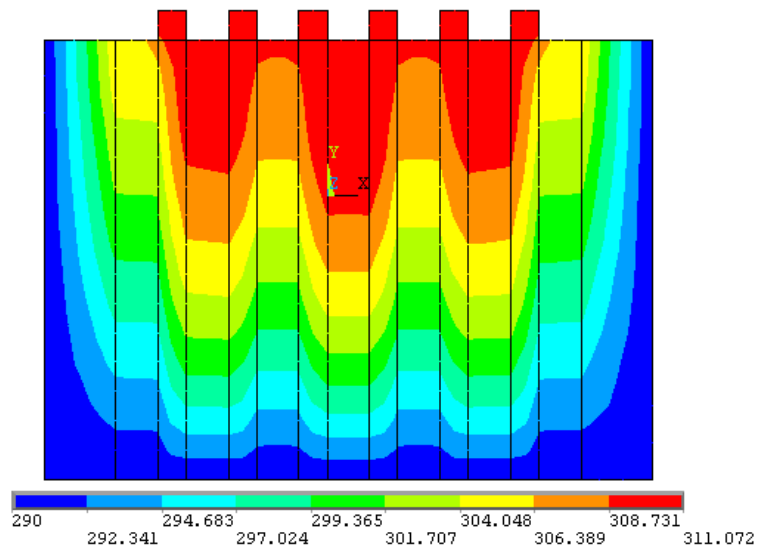


**Figure 29.** Two-dimensional thermal profile under 60 A current load.

As expected, the figure above shows the highest temperatures occur at the lead electrode due to higher heat generation values for the chemical reactions at the electrode-electrolyte interface. Moreover, the temperature profile corresponds to the MATLAB simulation results illustrated in Figure 7. Critical temperatures appear at the connections of the current collectors above the electrodes where the collectors that parallel the electrodes collect and carry electrons to the terminals. The outer casing remains relatively constant with only a few degrees of variation across the polycarbonate protection. Thermal imaging of similar battery configurations is consistent with the ANSYS model showing the highest temperature and the collector tabs and terminals.

#### **4.2.4 Three Dimensional Finite Element Analysis**

Two dimensional analyses of temperature effects provide a basic understanding of battery response under operating conditions. However, to fully encompass each components contribution to the system as a whole requires implementation of a three dimensional model. While material properties and applied loads are consistent with the two dimensional model, the 3D model has a number of significant additions. As shown in the figure below, the battery consists of six identical cells connected in series separated from one another by a thin plastic divide. The positive and negative electrodes are 12.6 cm by 14.3 cm with varying thickness depending on the cell design with the negative electrode designed slightly smaller. The electrodes are connected by the current collectors attached to the tab extending from each electrode in order to deliver or receive currents from the terminals. A 1.25 cm thick polyethylene outer casing protects the internal components from the external environment as shown in Figure 30.

In order to ensure reliable results, each cell is observed separately. In other words, the heat generation calculated for a single cell output by the MATLAB simulation is applied to each of the six cells individually. However, due to the heat transfer between the battery components the heat generation in the neighboring cell will affect the temperature of the entire battery.

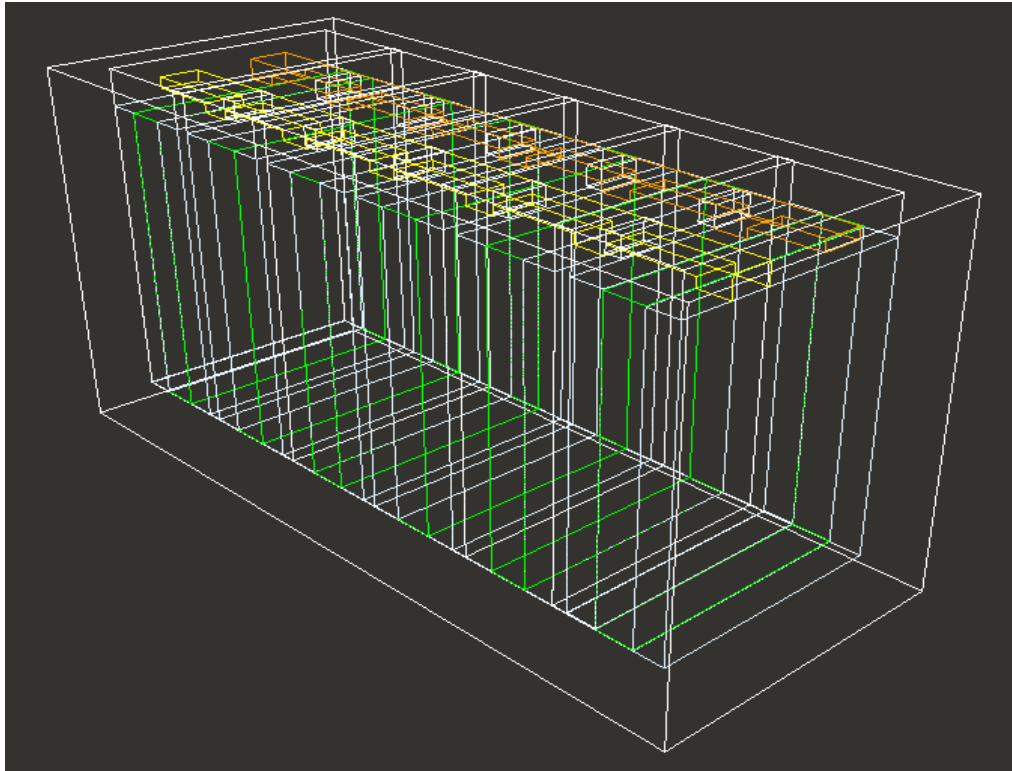


**Figure 30. Blueprint of battery configuration.**

As mentioned in the previous section, heat generation mainly occurs across the electrode/electrolyte interface. Employing the MATLAB simulation of the battery cell at a constant discharge rate, the heat generation at each electrode is calculated after a specified discharge time. Using the simulation data, heat generation loads are applied across the surface area of each electrode as watts per meters squared, or to the electrolyte

reservoir as watts per cubic meters [7]. Prior to the effects of heat generation, the initial temperature of the entire body is set to 300 °K at each node to represent room temperature. While at low currents there is temperature variation, extreme temperatures only occur at high charge or discharge rates. As pictured below, the maximum temperatures occur in the innermost cells within the electrolyte reservoir. A significant amount of heat is transferred to the current collectors, varying only a few degrees from the cell temperature. The small variation provides evidence that due to the components thermal conductivity properties, the terminal temperatures provide a suitable approximation of internal battery temperature. Therefore, during experimentation, the temperature at the terminals will be employed to represent internal temperature for comparison with computer simulation results. Furthermore, the much safer alternative of external thermocouple readings prevents the need for thermocouple probes into the unstable battery cells.

As shown below in Figure 31, the battery casing remains at a relatively constant near room temperature throughout the discharge process. However, since the terminal temperature does not provide sufficient data to extrapolate a temperature gradient and the outer casing remains relatively consistent with ambient air temperature, a thermal imaging camera is necessary for modeling comparison.



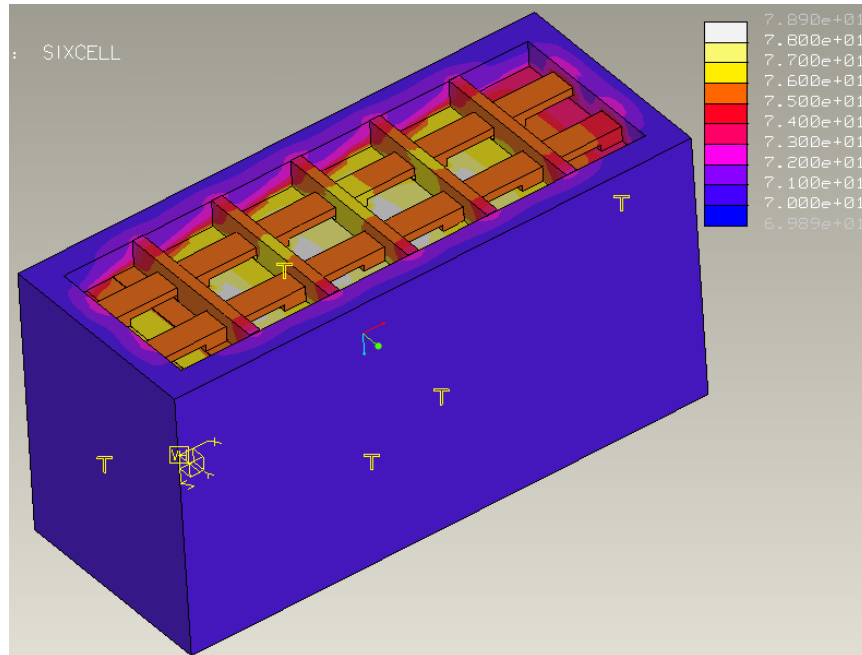


**Figure 31. Temperature distribution for 60 A discharge after 3 min.**

Closer examination of Figure 31 shows only slight variations of a couple of degree Kelvin at the center of each of the cell components. However, each of the cells experiences a significant deviation near the internal wall of the protective casing. Separation of the casing from the cells reveals a distinctive gradient for each of the battery components as shown in Figure 32. The decrease in temperature towards the outer boundaries will result in a drop in reaction rate at those positions compared to the maximum temperature experienced at the cell center. Therefore, the acid concentration will have a small but present gradient with the highest concentration experienced near the middle of the cell. Additionally, the outermost cells lower temperatures will cause a larger concentration gradient across the cell due to a decrease in particle collision. An additional side effect to the lower temperature is a slower discharge rate causing a higher voltage for the boundary cells.

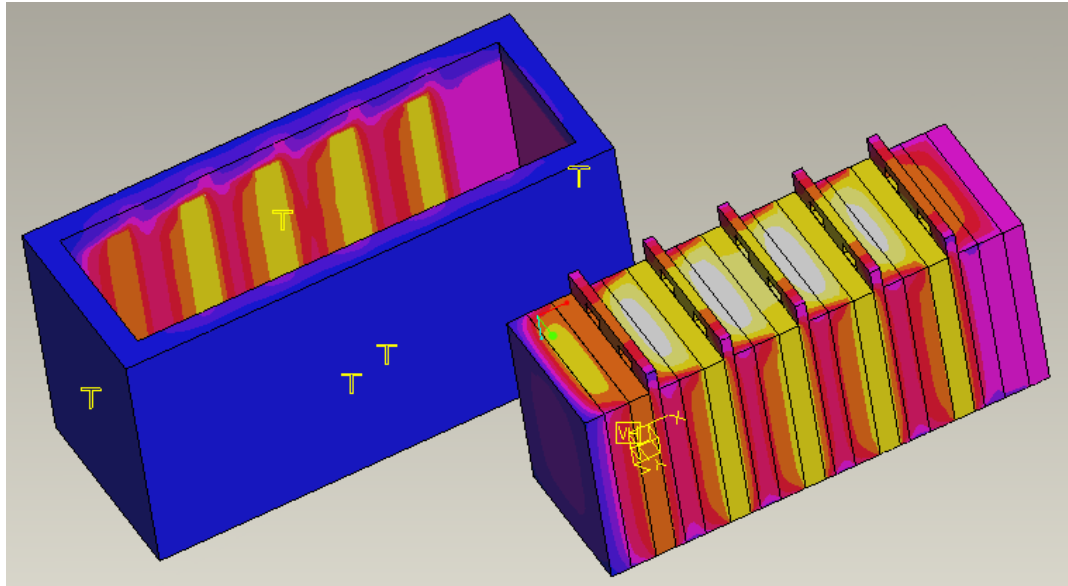


**Figure 32. Three-dimensional thermal profile during discharge.**

#### **4.2.4.1 Comparison with MATLAB Modeling**

The MATLAB simulation derives cell temperature as the average temperature during operation and is calculated due to the change in heat transfer rate over time. For this approach, the entire cell including the electrodes and electrolyte reservoir are considered one control volume. Therefore the heat generation is applied across the entire cell equally. The temperature derived from this method is reinserted into the initial loop used to calculate reaction rate and terminal voltage. The finite element analysis applied material properties to the various components while the heat generation is applied in a similar manner to the MATLAB model.

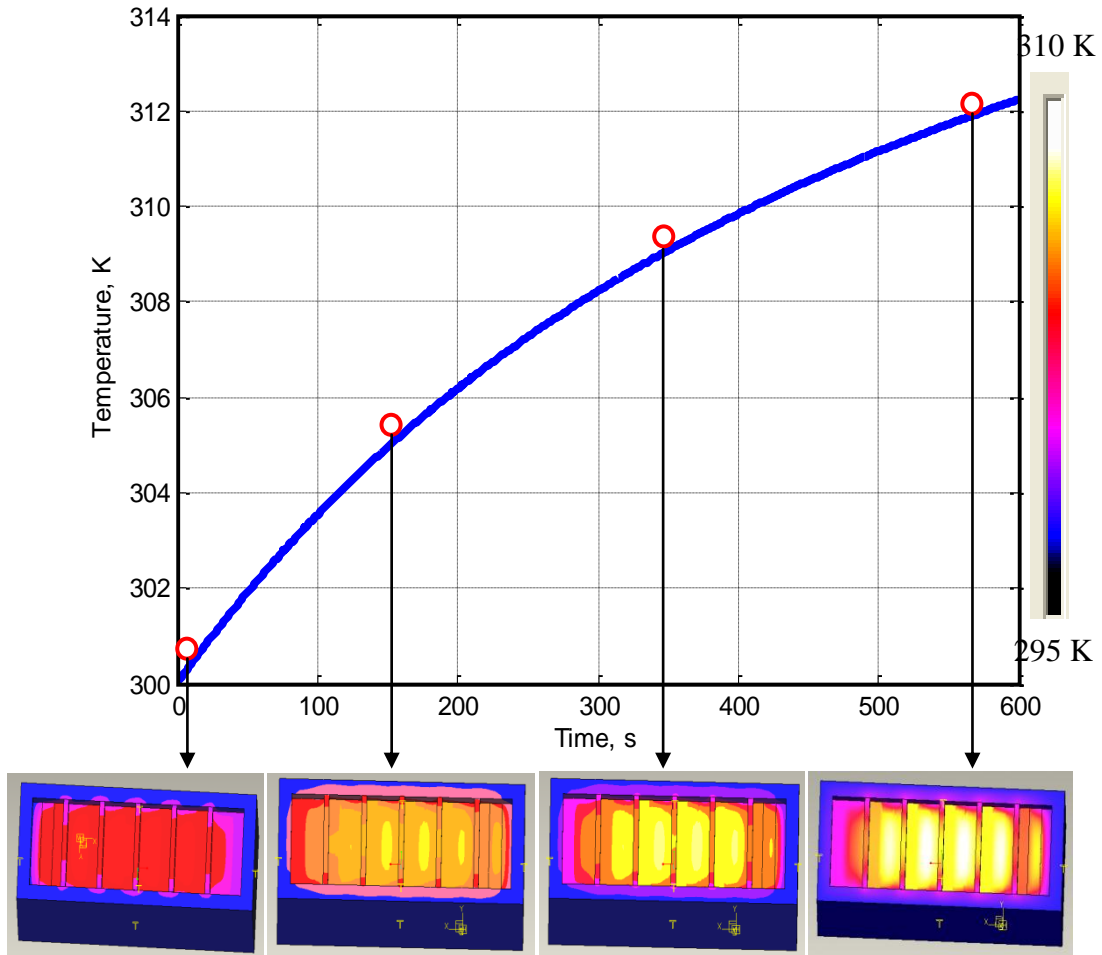


**Figure 33. Transient non-adiabatic temperature modeling comparison during the first ten minutes of 60A discharge.**

Figure 33 illustrates the change in temperature under 60 A discharge load for MATLAB and finite element analysis. The MATLAB simulation provides an average temperature across the cell comparable to that found using 3D finite element thermal profile. The initial temperature after only a few seconds is set prior to the simulations at 300 K, therefore the temperature is nearly identical. For the other three comparisons the MATLAB simulations shows a slightly higher temperature than that of 3D profile. The largest discrepancy occurs the longest period after the initial load is applied varying

almost three degrees Kelvin. However, since battery performance changes only after significant temperature change, the small difference is acceptable.

Additionally, the comparison provides assurance that the non-adiabatic model provides a better representation of temperature change than the adiabatic case, as heat transfer with the external environment is considered for both MATLAB and finite element simulations.

## 5 EXPERIMENTAL TESTING

The objective of the experimental setup is to assemble a testing environment capable of recreating battery working conditions allowing for data extraction from the important areas. A typical commercial automobile consists of an electrical system made up of an alternator, voltage regulator, and a sealed lead acid battery as shown in Figure 34. The alternator connected to a voltage regulator, internally or externally, acts to charge the battery during vehicle operation, typically applying 10A or less since high charge currents and overcharge can be harmful causing corrosion and gassing. Generally, batteries experience minimal discharge currents, however during cranking, a lead acid battery can experience upwards of 600 A for a few seconds [26].

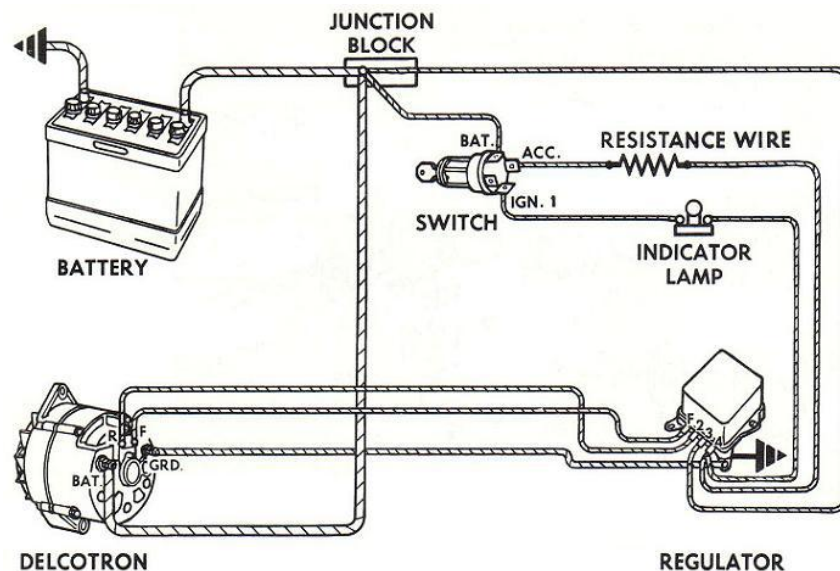


**Figure 34.** Automobile electrical system diagram [26].

The resulting setup, mimicking real world automotive electrical systems, allows for various loads and charging profiles to be applied to the battery and observation of the transient voltage, current, and temperature. Discharge current is controlled by an electronic load that varies the resistance between the battery terminals in order to control the load current and programmable power supply is incorporated to set charge current.

For the purposes of our research, the preparation leading to experimental testing focused on the thermal and vibration effects under extreme conditions. When subjected to extreme temperature a noticeable change in overall performance during both charge and discharge cycles are expected. Therefore, placement of temperature readings and the ability to control the ambient temperature are of great concern. Results from the modeling efforts previously discussed provide sufficient testing ranges for the various parameters.

While research of thermal effects exists, reliable data in the area of vibration effects is lacking. An Auburn University supplied thermal chamber is utilized to subject the battery to a wide range of temperatures, while a shaker is employed to exert various frequencies similar to those experienced during driving conditions.

## ***5.1 Testing Equipment***

The data flow and wiring configuration is illustrated in Figure 36 below demonstrating the roles of the essential components of the setup. The equipment employed comes from a number of suppliers of battery testing and data acquisition technologies. The following list provides a model number and description of each piece of equipment in the battery testing process.

- Sorensen DCS50-20E & DCS8-125E Programmable Power Supplies for supplying current and voltage charging profiles
- Dynaload DLVP 50-300-3000A Electronic Load for discharging the battery at values up to 150A
- Agilent 34410A Multimeter for voltage response, current transducer measurement, and internal resistance of the battery under equilibrium and dynamic conditions
- SC-2345 and SC68 National Instrument Module Connector Block for current transducer and thermocouple inputs and analog outputs used to control electronic load
- NI PCI-6025E Data Acquisition Unit for connection allowing the various readings to be viewed through LabView
- LEM LA-200P Current Transducer for measuring discharge current delivered by the battery
- Three NI-TC02 National Instrument Thermocouple Input Modules relays temperature measurements
- Three K-Type thermocouples for terminal, casing and cell temperature measurement
- Model AVH-14-6-6-S/AC, Cincinnati Sub-Zero (CSZ) thermal chamber capable of temperature -80 °C to excess of 200 °C
- Model V850-440T Ling Dynamic Systems air cooled vibrator allows for frequency and magnitude application

A photograph of the experimental setup is provided in Figure 35 illustrating the battery testing station during operation. The battery is placed inside the thermal chamber on the shaker platform and mounted by a wedge apparatus to ensure stabilization during vibration testing as well as simple removal after the experiments are complete. The thermocouple wires, multimeter extensions, and battery cables are fed through a small

opening in the thermal chamber floor and securely fastened to the appropriate area of the battery as shown below.

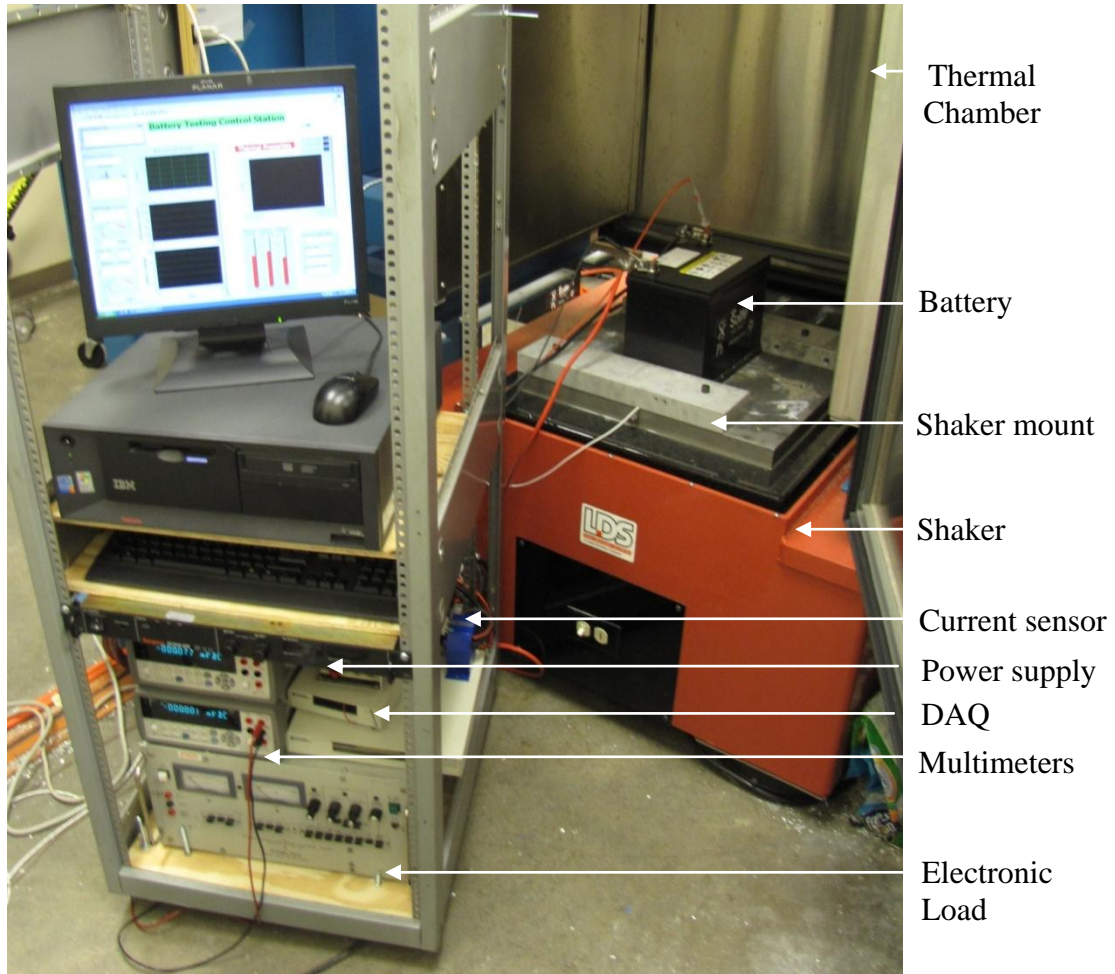


**Figure 35. Battery testing station.**

The photograph above shows the equipment setup but does not provide adequate representation of the equipment interaction and wiring present in the experimental setup. Illustrated in Figure 36, during operation either the power supply or electronic load cables are fed through the current sensor on the way to the thermal chamber cable port depending on the process. Then, the thermocouple and multimeter measurements from



the battery and the current sensor readings from the supply cable are relayed to the computer which is then organized by the LabView program created to automate the setup. Data is logged as an Excel file for future viewing and model comparison.

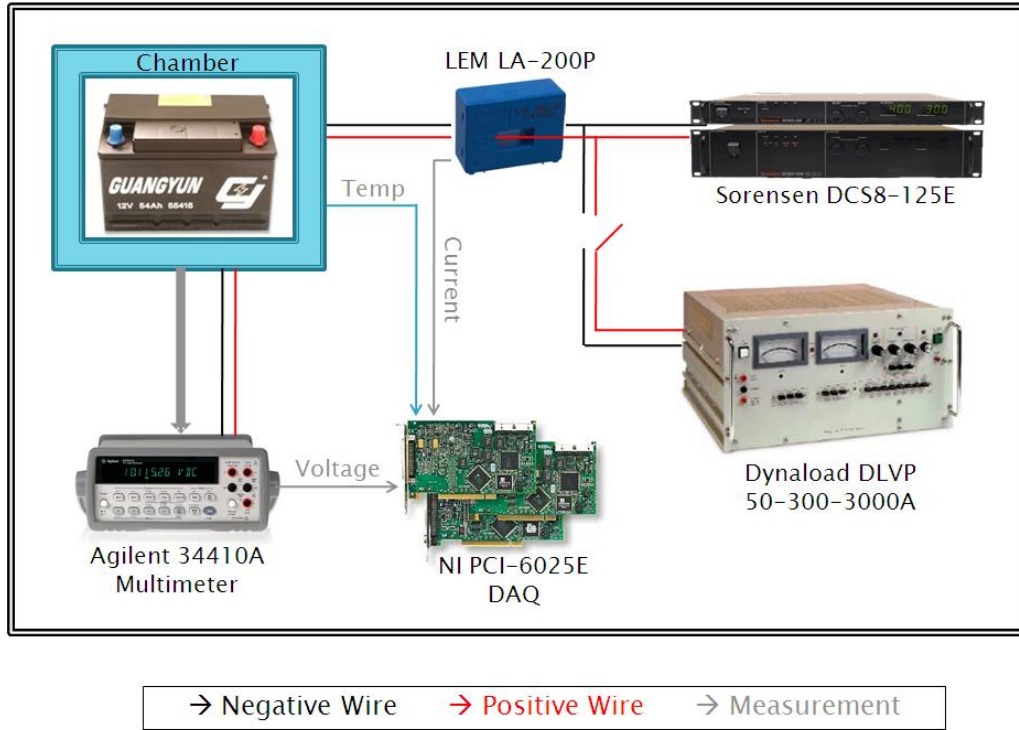


**Figure 36. Experimental setup wiring diagram.**

## 5.2 Battery Parameters

Extensive testing of automotive batteries requires a large supply of identical batteries in order to extract reliable data. As the batteries are cycled and experience extreme temperatures and loads, extensive damage is an unfortunate side effect. Therefore, additional batteries are necessary to model operation at the peak performance of the battery. The sealed lead acid (SLA) batteries, model CMF68L, under observation are provided by Songwoo USA Corporation, a commercial supplier for Hyundai Motor

Company. The batteries in question provide 600 Cold Cranking Amps, CCA, and have a 60 Ampere-hour capacity. Additional specifications are provided by the manufacturer are outlined in the table below.

Table 1  
Sungwoo USA Corporation VRLA Battery Data Sheet

<b>Property</b>	<b>Value</b>
Type	CMF68L
Terminals	SAE Post
Nominal Voltage	12.36 V
CCA	600 A
Life Cycle	4400 Cycles
Reserve Capacity	110 min
Charge Acceptance	21 A
5 Hr Capacity	54 A-h
Total Weight	18.7 kg
Vibration Test	OK
Electrolyte Specific Gravity	1.26±0.01

Electrolyte specific gravity allows for calculation of electrolyte concentration when the battery is fully charged. Comparison of the manufacturer specified maximum measured specific gravity, 1.26, to electrolyte density at various concentrations reveals  $5.65 \text{ mol/cm}^3$  for the Songwoo battery at full charge [1]. Charge acceptance and cold cranking amps, CCA, outline the extremes of charge and discharge loads while the standardized nominal voltage prevents overcharging. Also, the battery structure is capable of withstanding vibration testing as authorized by the manufacturer.

### ***5.3 Battery Testing Station Description***

Although the sections above introduce the equipment used, a more thorough description of each components role is necessary. With all the necessary equipment in place, a system capable of recreating specific testing conditions is necessary to obtain reliable data. In order to manage the testing equipment and measurement devices, a LabView control station is created to automate equipment and export their readings. Accurate representation of battery performance is obtained as data from the current sensor, multimeter, and thermocouples are recorded every 20 milliseconds. The excel output file, as shown in Figure 37, is selected in the top left hand corner providing documentation of experimental results recording temperature, voltage, and discharge current. Multimeter readings display the battery voltage and discharge current in real-time on the bottom left hand corner of the front panel. Three K-Type thermocouples measuring temperature are displayed separately as gauges as well as plotted in real-time for comparison.

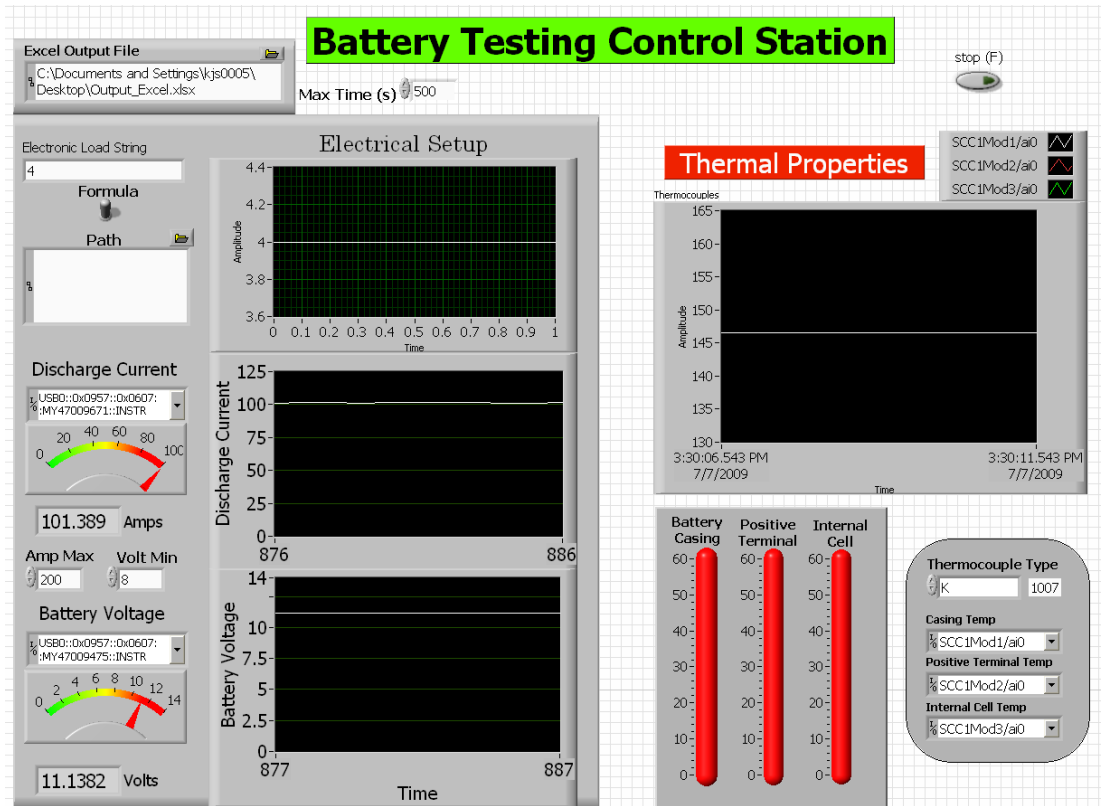


**Figure 37. Battery LabView Control Station screenshot.**

Safety measures are built into the LabView code to prevent harmful scenarios for the batteries and engineers. Maximum current prevents excessive damage to the power supply cables while minimum voltage maintains a specified SOC preventing irreversible capacity loss. Additionally, the total test time is controlled through either the maximum time setting or through the analog waveform path file. However, the primary role of the path file is to control the voltage to the terminals of the electronic load through discharge profiles as discussed in the section below.

### **5.3.1 Programmable Charge and Discharge**

For our experimental setup, several pieces of equipment are utilized in the testing of lead acid batteries under a number of conditions to provide an overall scope of battery performance. Specifically, a Dynaload electronic load and Sorenson power supply provide control of charge and discharge currents, respectively.

The Dynaload Electronic load allows for simple discharge rates of either constant current or constant resistance using external dials. Additionally, through terminals on the rear of the Dynaload device and the analog output pins of the NI-SCB68, discharge profiles are predetermined and controlled from the battery test station shown in the top left hand corner of Figure 37. As a result, the battery is subjected to an array of discharge profiles for observation including step and ramp, as well as a combination of the two. The Dynaload DLVP 50-300-3000A electronic load is rated for 1V/25A and the analog output of the NI-SC68 is restricted to a maximum of 5V resulting in a maximum discharge current of 125 A using control through the external module.

### **5.3.2 Measurement Devices**

The ability to gather consistent and precise measurements are vital to the quality of the results. The devices described below have higher resolution and accuracy than is required providing a sufficient safety factor.

#### **5.3.2.1 Thermal Readings**

K-Type thermocouples are employed to measure the temperature of the battery at each terminal and on the external casing. Ideally, the temperature of the sulfuric acid water mixture would be monitored from inside the cell, but due to the volatility of

sulfuric acid and the pressure regulated batteries, only external temperature readings are recorded. However, measuring the temperature at only a few locations is suitable since internal temperature can be calculated using heat transfer and thermodynamic equations discussed in the earlier sections. Specifically, due to the high thermal conductivity of lead, the thermocouples placed at the positive terminal provide the best representation of the internal cell temperature. For further representation of the thermal effects, a Nikon Thermal Imaging camera provides snapshots of the batteries overall temperature at different stages of the discharge and charge processes. The integration of thermal imaging allows for validation of the internal temperature calculations from the external thermocouple readings. Additionally, finite elements analysis, ANSYS and ProEngineer, provide a three dimensional thermal profile for comparison with imaging data.

### **5.3.2.2 Electrical Sensor Equipment**

LEM LA-200P current sensors relay the current experienced by the battery during the discharge or charge process. The LEM current sensors operate under the laws of the Hall Effect, where the magnetic field through which the current flows is affected by the magnitude. 15V positive and negative are required to power the device, which provide a measure terminal that outputs a voltage that changes proportionally to the current passed through the sensor. Current sensors are solely employed to measure discharge current since the charge current is applied by a programmable power supply. Due to the importance of measurement accuracy, a significant amount of calibration is necessary to assure precise calculations. Once calibrated, three 10  $\Omega$  resistors are connected in parallel to create a 3.6  $\Omega$  (measured) resistor that is connected to the sensor measure

terminal. Additionally, the connected battery cable is looped three times through the current sensor in order to provide a more accurate representation. Using the manufacturer specified 1:2000 conversion ratio and measured voltage across the resistors, the discharge current is calculated. A sample calculation is provided below:

$$Current = \frac{(Measured\ Voltage) \cdot (Conversion\ Ratio)}{(Resistance) \cdot (Number\ of\ loops)} \quad (49)$$

$$I = \left(\frac{2000}{1}\right) \cdot \left(\frac{1}{3.6\ \Omega}\right) \cdot \left(\frac{1}{3\ loops}\right) \cdot V = \underline{185.2 \cdot V}$$

Agilent 34410A Multimeter records the nominal voltage of the battery allowing equilibrium potentials and internal resistance to be calculated and compared to the calculated modeling values. The multimeter has simple USB connections to the computer and allows for easy extraction of the data. Most importantly, real time measurement of battery voltage and discharge current provides I-V curves for comparison with MATLAB results. Battery testing equipment specifications, as outlined by the US Department of Energy (DOE), requires a minimum resolution of 50 Hz. Since the configuration relies on several pieces of equipment, the overall resolution is governed by the slowest link in the system. LabView control of the testing equipment records information at specified intervals. During battery testing, data is recorded every 20 milliseconds well under the specified measurement resolution.

The experimental results from battery testing are collected through a NI-PCI 6025E Data Acquisition Board connected to the computer. The DAQ board receives information from the SC-2345 Signal condition boards with National Instrument

thermocouple modules attached. Additionally, the DAQ board transmits the discharge profile established in LabView through the analog output terminals of the NI-SC68 to control the electronic load.

### **5.3.3 External Environment**

An Auburn University supplied thermal chamber is employed to execute charge-discharge cycles at varying atmospheric temperatures. The thermal chamber is capable of temperatures ranging from  $-80^{\circ}\text{C}$  to  $200^{\circ}\text{C}$ . Battery testing outlined by the DOE only requires ranges from  $-40^{\circ}\text{C}$  to  $100^{\circ}\text{C}$ . Due to safety concerns associated with high temperatures, our ambient temperature will not exceed  $80^{\circ}\text{C}$  or move below  $0^{\circ}\text{C}$  to prevent freezing.

Thermal testing is performed in stages, increasing the temperature by intervals of  $5^{\circ}\text{C}$  until the full range of temperatures is complete. Measurement devices allow for records of discharging and charging performance at various temperatures to be compared with modeling results. For each temperature, the load experienced by the battery is increased by intervals of 10A. However, due to extensive damage caused by continuous discharge at high currents, shortening the discharge time is necessary to prevent capacity loss. As a means to protect the battery, a minimum terminal voltage of 8 volts is set through the LabView control. In order to capture data from the battery during thermal testing, wire routing is of great concern. Adequate cable lengths for the battery charger, electronic load, and thermocouples connect to the battery allowing for control of the environment from outside the chamber. Specially designed wire ports are built in to the thermal chamber to allow access without affecting the chamber environment.



Maintaining battery performance as the batteries are cycled is essential to the reliability of the data extracted. Therefore, immediately after discharge each battery is moved to the charging station to ensure the health of the battery, because if left in a low SOC for a long period there would be irreversible capacity loss. During the charging process, the thermal chamber is adjusted to the proceeding temperature for further observation. In addition to the immediate charge of each battery, detailed records of each test run is kept to provide the history of each battery as shown in Appendix C.

#### ***5.4 Vibration Effects***

Automotive batteries are made up of sensitive materials and are greatly affected by the contact surface area of the electrode and electrolytes. Various parameters and environmental circumstances may cause significant changes to the amount of contact area. Battery researchers have focused on a number of these issues, yet vibrations effect on automotive batteries remains a largely unexplored topic. When the automobile is in operation, there is a significant amount of liquid displacement experienced in the electrolyte reservoir. During turns or as the automobile experiences acceleration through the engine, the electrolyte position is affected. The term used to describe the movement of a liquid inside a container subjected to vibration is sloshing. When considering vibration along the direction from terminal to terminal, sloshing causes a maximum amount of contact surface at one electrode and a minimum at the opposite.

Despite the suspicion of significant effects caused by vibration experienced under automotive conditions, experimental findings to support the belief are lacking. Therefore, incorporating the battery testing station shaker control, the batteries are

subjected to a variety of vibration amplitudes and frequencies under a number of discharge loads. The frequencies ranged from 10 Hz to 80 Hz and the amplitudes of 2 cm and less. Although, the vibrations caused excessive movement of the battery electrolytes, the hypothesis proved incorrect as the effects of vibration on battery performance is minimal as shown in Figure 38 below.

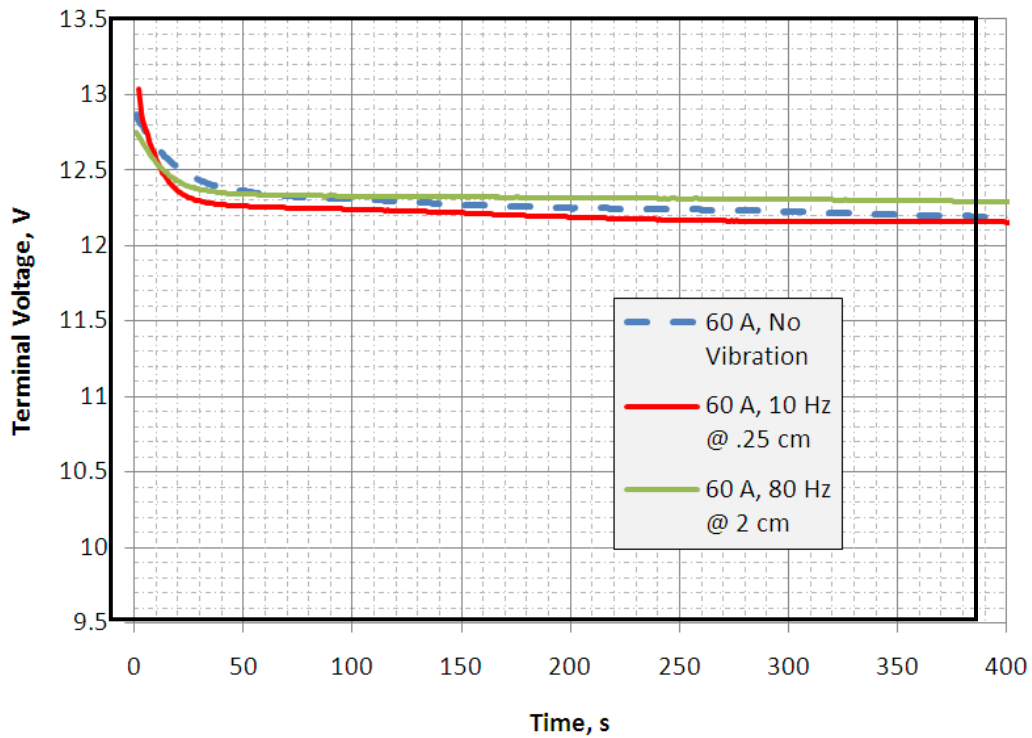


**Figure 38.** Vibration experimental results during the initial stages of discharge.

The discharge performance under various vibrations shows nearly identical slope, and the small discrepancy in terminal voltage appears only as a result of initial voltage drop when load is applied. Discharge loads from 10 A to 125 A were applied to the battery with similar results. Although the results from experimental data were not as expected, useful information was obtained. The knowledge of insignificant effects on

battery performance deters the need for further investigation into the subject. As a result, the main focus of the experiments turns back to heat generation and the temperature effects on battery components and overall performance.

## ***6 COMPARISON OF RESULTS***

The dynamic response of a single lead acid battery cell is extensively discussed in the sections above examining electrochemical values of acid concentration and reaction rate and their behavior as isothermal, non-isothermal, adiabatic, and non-adiabatic systems. The following section aims to provide real world evidence of the validity of the modeling results through the measureable parameters current, cell voltage, and temperature of critical areas. A structured test matrix for each battery was created prior to testing, outlining the role of each battery to be tested in order to ensure reliable results.

### ***6.1 Dynamic Temperature Comparison***

In order to validate the temperature change from the various sources of heat generation, thermocouples were placed on the battery terminals and casing. Reference data and comparison of experimental results to simulation outputs revealed the positive terminal as the most accurate representation of internal temperature. Initially, temperatures were gathered during the first five minutes of discharge when the greatest increase in temperature occurs. Experimental results for discharge currents ranging from 20 A to 100 A is provided in Figure 39. MATLAB modeling of the same discharge currents is directly below the experimental results for comparison.

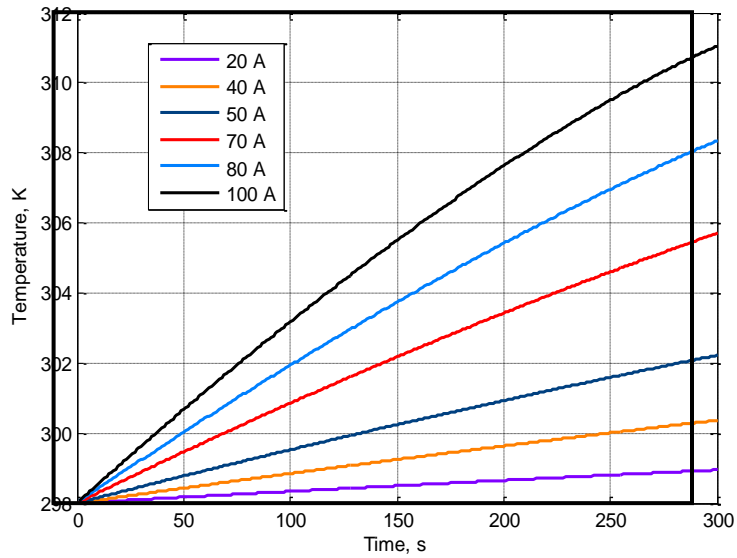
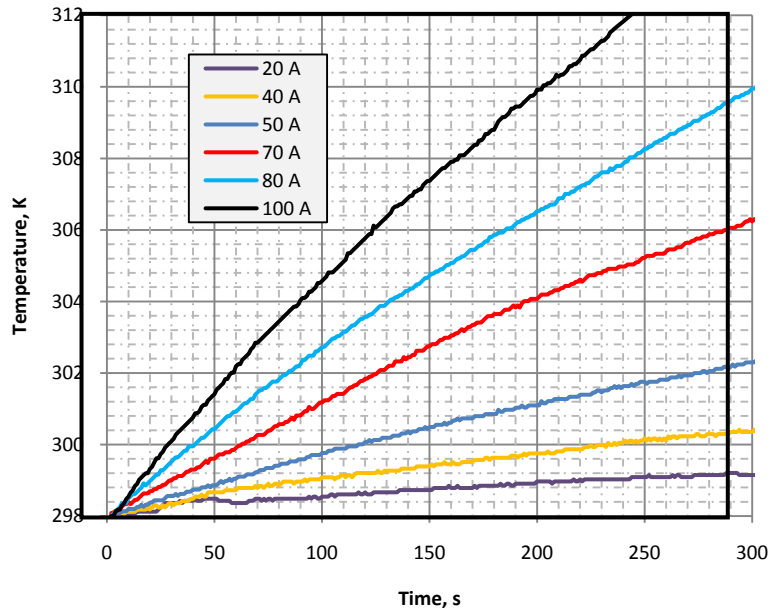


**Figure 39. Transient temperature, (Top) Experimental, (Bottom) Modeling.**

The temperature response of the MATLAB modeling is comparable to the readings of the strategically placed thermocouples, varying only a few degrees at high discharge currents. Additionally, the effect of heat transfer is evident as the slope of increasing temperature lessens as discharge continues for both experimental and

modeling results. Therefore, non-adiabatic simulation provides a better representation of transient temperature. Further evidence is provided in Figure 40 comparing the response of adiabatic and non-adiabatic models against the thermocouple readings during operation.

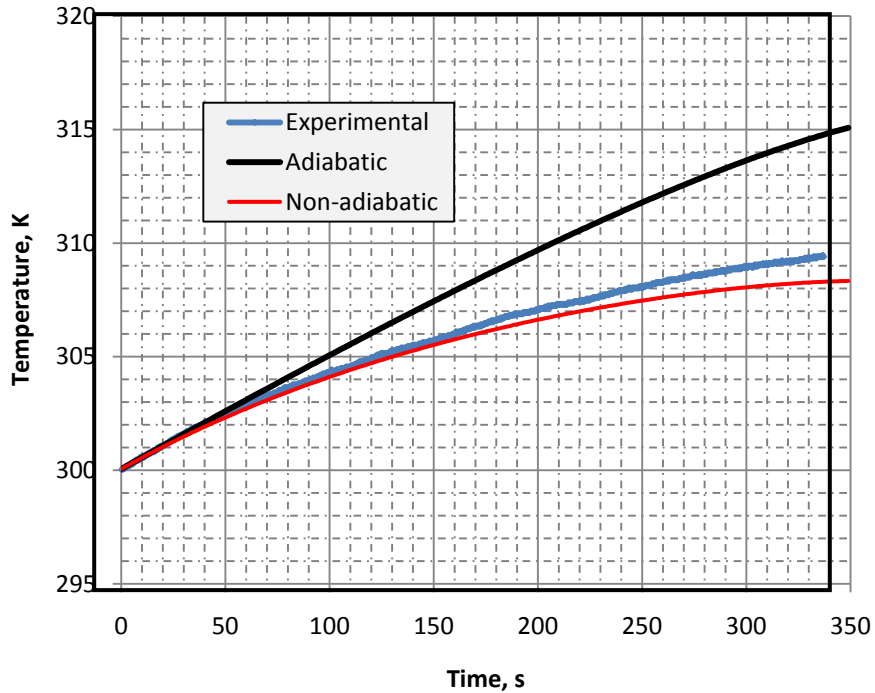


**Figure 40.** Temperature comparison for 1.25C (75 A) discharge current.

While under a 75 A discharge load, the internal temperature increases nearly 10 degrees Kelvin from the initial state of 300 °K during the first six minutes. The amount of temperature change is useful information, but the rise in temperatures' effect on performance remains to be seen.

## 6.2 Discharge Performance

As for any experimental process a standard reference state is needed to determine the effects of varying parameters. For our purposes, the reference state will be performance when ambient temperature is equal to room temperature, 300 K. From this initial reference state the temperature is increased and decreased in intervals of 10 degrees Kelvin to observe the effects within the range of 0 °C and 80 °C, well within the range of acceptable operating conditions. Since significant heat generation only occurs under high loads, experiments involving discharge currents within the low, medium, and high ranges will be performed for comparison. An example comparison of the discharge performance under the various loads at room temperature is provided in Figure 41 below.

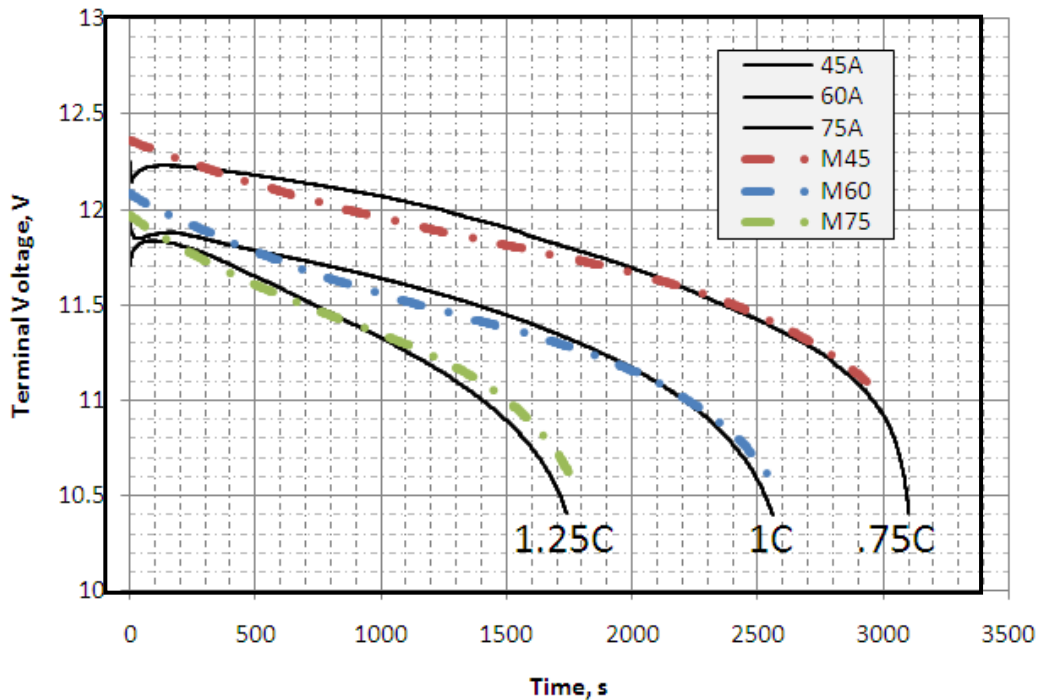


**Figure 41.** Reference at 300K, 100 % SOC. Solid, experiment, dashed, model.

The comparison provided above shows close representation by the MATLAB model of battery performance for 45 A, 60 A, and 75 A discharge at room temperature. Slight discrepancies appear for the initial voltage drop, but only vary 50 mV during the first quarter hour of discharge. There is a more significant difference near the end of discharge as the internal resistance grows causing a sudden drop in terminal voltage. The model shows similar effects from the increase in resistance but less drastic. This is due to the model's dependence on acid concentration. As the experimental results illustrate the quick descent, the simulation is structured so that when concentration is calculated to be zero at the positive electrode the run stops, before the final drop occurs.

As experienced during the simulation of battery performance, significant change in discharge performance only occurs at extreme temperatures. The initial testing under mild conditions with minimal effects results in a reassessment of strategy focusing more intensively on the extreme temperatures and varied load responses. The remainder of the comparison of experimental results includes the reference state at 300 °K, and the boundaries of the operating temperature range provided by the manufacturer of 273 °K and 353 °K (0 °C and 80 °C) to avoid freezing of the electrolyte. The batteries are subjected to a range of currents until near the end of discharge avoiding the final voltage drop. A comparison of experimental and simulation results are provided for 45 A discharge current at 273, 300, and 353 °K below.



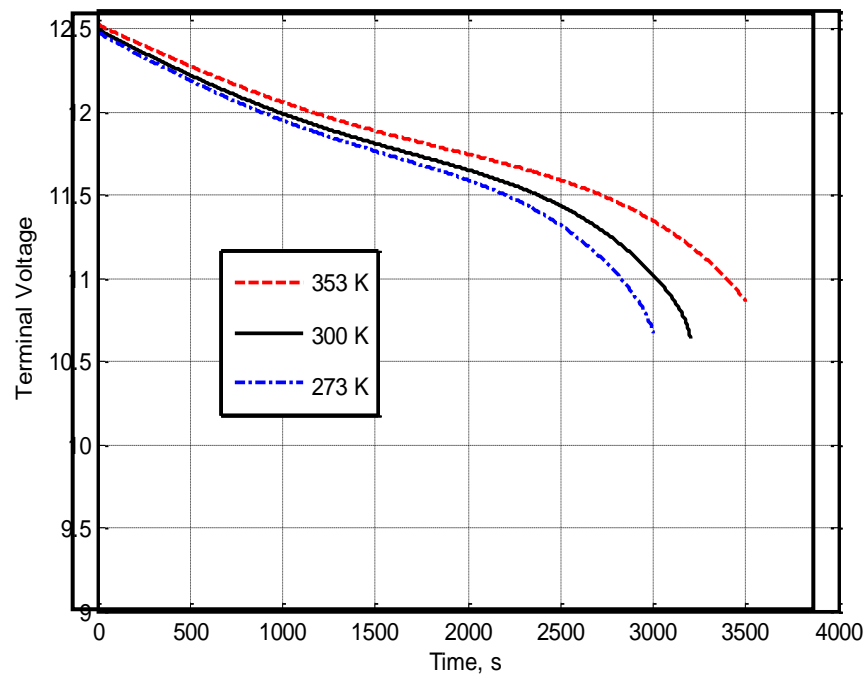
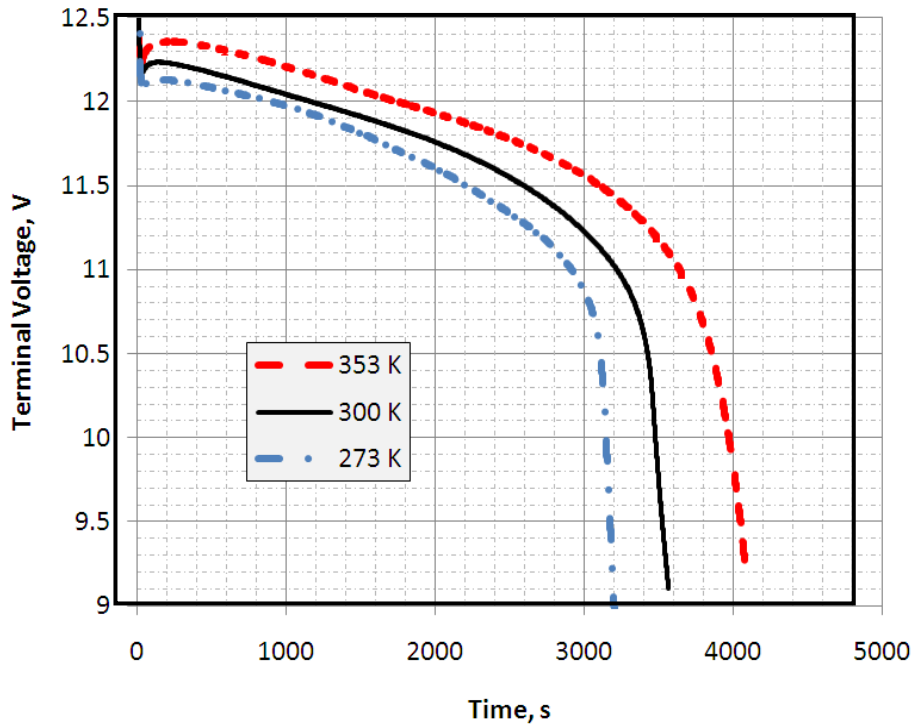


**Figure 42.** Ambient temperature effects on terminal voltage comparison during 45 A discharge. (Top) experimental, (Bottom) modeling.

As illustrated above, decrease in temperature has negative effects on the battery voltage showing a slight decrease in initial voltage and significantly lower discharge time. There is about a 5 minute difference in total discharge time between 273 °K and 300 °K, and nearly 6 minutes between 300 °K and 353 °K. The initial voltages of the plots above differ slightly due to the approximations of the initial voltage drop. However, the responses reveal similar slopes and voltage near the end of discharge. In full, the modeling shows close approximation of battery performance and the various temperatures.

The experimental comparison thus far considers only constant current during discharge. However, the MATLAB simulation has the ability to model charge and discharge behavior under transient current loads. A typical profile employs continuous steps to observe the change due to increasing current voltage drop and overall battery performance. Pictured below in Figure 43 is the 10 A step input current on the right vertical axis and the response of the experimental and modeling voltage on the left hand vertical axis.

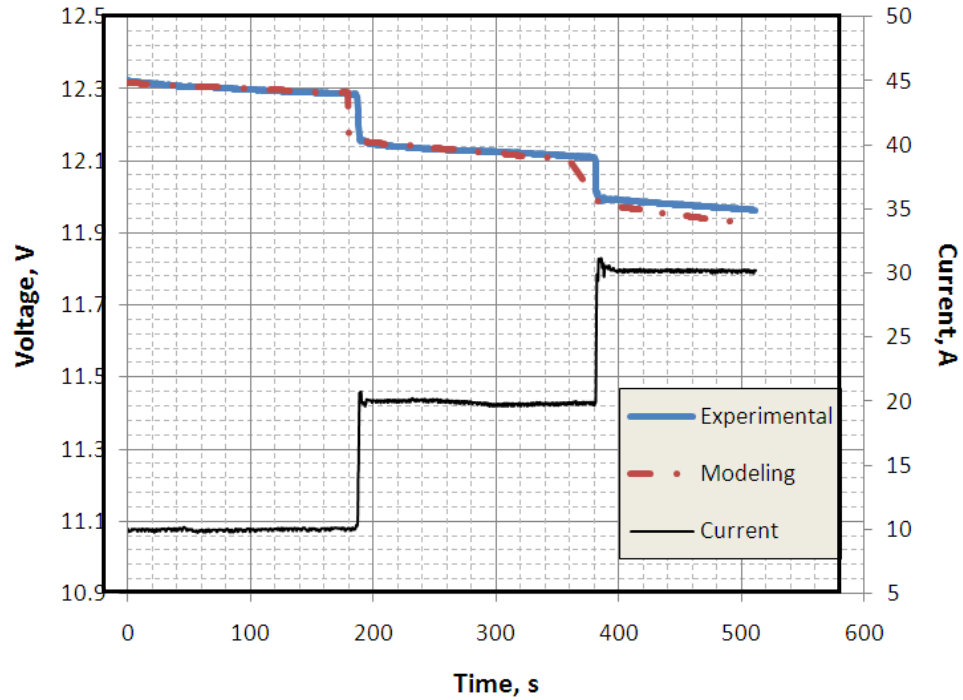


**Figure 43. Step Response for discharge at 300 K.**

Comparison of the 10 A and 20 A load steps to the modeling results show a good relationship. However, the modeling during the 30 A load shows as much as .02 volts discrepancy from the experimental data. Most notably, the initial voltage drop caused by the increase in load is greater for the modeling response while the voltage at the end of the 20 A step is slightly lower causing a compound effect. Additionally, the magnitude of the voltage drop is calculated by the product of the load current and the battery internal resistance therefore both values must be constant and accurate to provide a proper representation. Yet, the increase in current is gradual and not instantaneous, and the internal resistance is approximated.

Further investigation into the models' ability to simulate dynamic current effects on terminal voltage incorporates a pulse profile. The response pictured in Figure 44 compares experimental and modeling results for two 50 A pulses, each followed by a

period of rest of the same length. The simulation closely represents the real world results only differing 40 mV during the second pulse. Again, this is mostly attributed to the approximation of the amount of voltage drop and recovery.

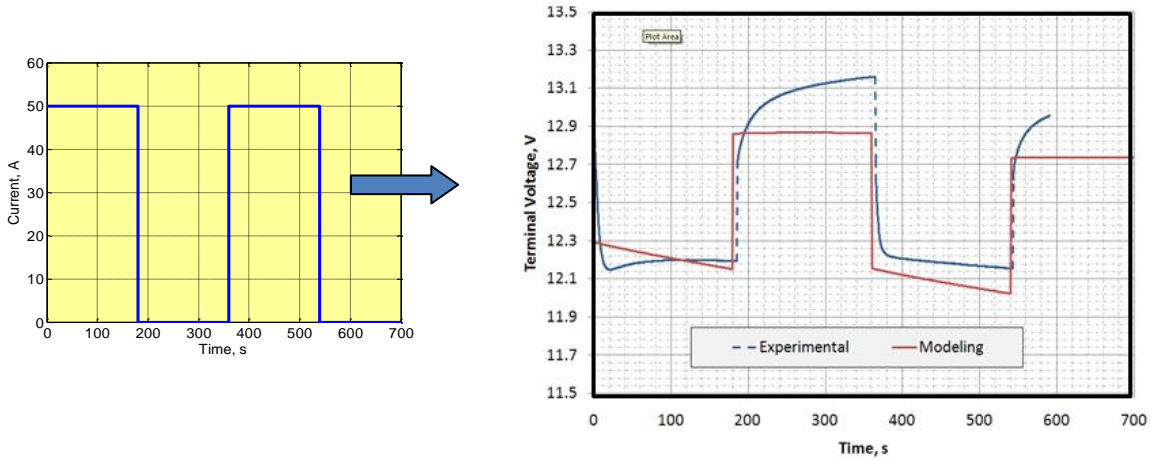


**Figure 44.** 50 A pulse discharge response.

### 6.3 Thermal Imaging

Safety issues discussed previously related to the volatility of sulfuric acid and the complexity of the internal battery structure prevented internal temperature measurements with the use of thermocouple probes. Thermal imaging emerged as the best and safest alternative. Thermal imaging detects radiation in the infrared spectrum to determine temperature across its field of view, FOV. Since all objects emit radiation based on their temperature according to Planck's law of blackbody radiation, computer software provides output temperature through comparison with measured radiation. The COMPIX PC2000 thermal imaging camera is capable of snapshots every 20 seconds, scanning the FOV taking infrared readings along the path.

Observation of thermal effects with the use of the thermal imaging camera provides proof that the positive terminal provides the best comparison for MATLAB simulation results for the internal battery temperature only varying a few degrees. However, since the thermal imaging results show a distinct temperature gradient the most useful comparison is with three dimensional finite element modeling as shown in Section 4.2.4. The three dimensional FE analysis is a transient model as heat generation changes throughout the charge and discharge processes as function of overpotentials and temperature coefficients at the electrodes. As a result, snapshots from the ANSYS and ProE analysis are taken at instances consistent with the discharge time captured by the thermal camera. Temperature distribution from the modeling and experimental testing are compared in Figure 45 below extracting results from the initial equilibrium state up until 10 minutes after the initial load is experienced.

Lead acid batteries under a constant load show temperature readings that tend to level off after a certain period of time. Over the duration of discharge, the magnitude of overpotential steadily decreases resulting in a noticeable decrease in slope of transient temperature. Additionally, the incorporation of heat transfer effects causes decrease in temperature as the external environment and battery work to achieve thermal equilibrium. Therefore, the first six minutes of discharge shows the greatest change in cell temperature validated by the analysis illustrated in Figure 45.

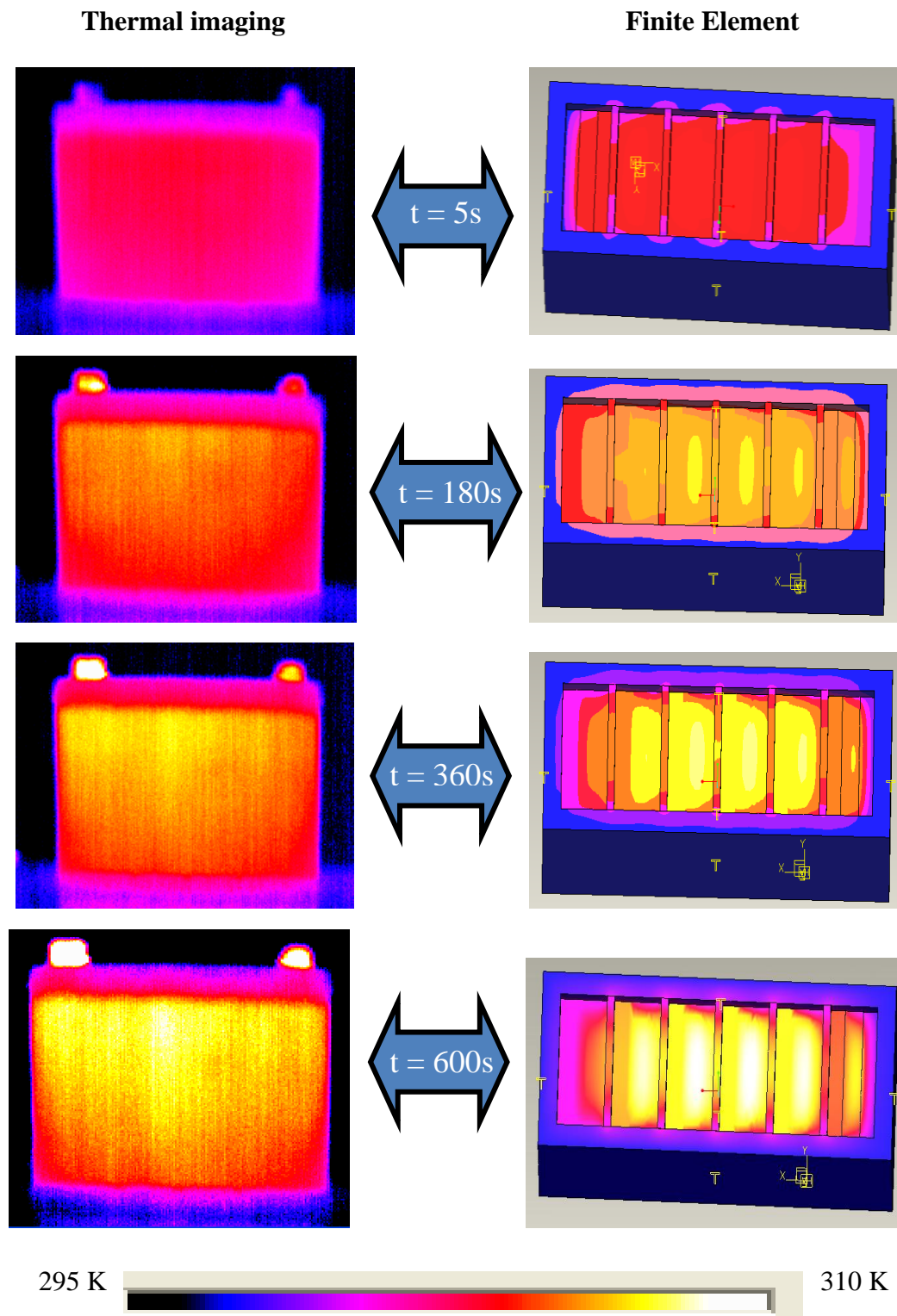


**Figure 45.** Thermal imaging and FE analysis comparison at 60 A discharge.

The comparison in Figure 45 shows temperature distribution consistent with thermal imaging results. In both cases, the highest temperatures nearing 310 °K after 180 seconds occur in the center of the battery at the top of the electrodes near the current collectors and decrease slightly in the cells near the boundaries of the outer casing. Elevated temperature in this area is a result of greater current flow through the metallic components connected to each terminal which are removed for easier view of the battery cells. The variation between the terminal temperature and internal cell temperature is a result of the contact surface area between the electrical cable connectors and the terminals. A closer look at the temperature in each region is provided in Figure 46, where the center cells show a 310 °K temperature while the outer cells experience temperatures near 300 °K.

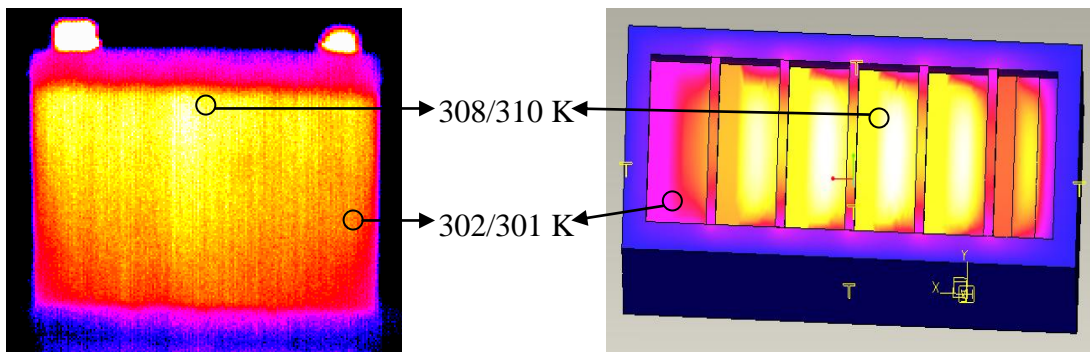


**Figure 46. Specific areas temperature comparison 600s after initial 60 A load.**

The major contribution of the thermal images is exposure of the areas that experience the greatest temperature increase. Using this knowledge, closer attention to these areas during FE analysis is necessary to determine possible improvements to the overall battery structure and component composition. Since the amount of heat generation results from distinct chemical reactions allowing for only slight variations, the

properties of the additional components absent from these reactions are the more apt to change. Specifically, altering material temperature coefficient and thermal conductivity of various components will allow for greater control distribution of the energy created during the electrochemical processes.



## *7 CONCLUSION*

This paper outlines the communication of a mathematical model and finite element analysis seeking to fully represent the performance of a six cell sealed lead acid battery for implementation into existing vehicle models. Following modeling results, experimental data is obtained to establish validity of the simulations. The approach incorporates existing equations and methods for the simulations of a single cell and expands to represent the entire battery. Close attention is paid to the thermal effects of the various components and electrochemical processes present in the battery cells that determine quality of performance. In doing so, certain findings provide a greater understanding of processes on a molecular level as the well as the overall scope of the battery's ability to deliver the necessary electrical power.

Initially, when investigating electrochemical processes, a pattern arose from the application of various electrical and thermal loads. As expected, increase in current results in a higher reaction rate along with a greater percentage of reactions occurring along the electrode electrolyte interface. However, temperature is a well known catalyst to chemical reactions, leading to the assumption of higher reaction rates at elevated temperatures. In reality, reaction rates grow increasingly uniform across each of the electrodes for both the charge and discharge process as temperature rises due to increased ionic conductivity and diffusivity. The more consistent reaction rates at each section of

the battery leads to a lower concentration gradient, causing a slightly higher concentration at the positive electrode and the opposite effect on the negative electrode. As a result, the terminal voltage is only slightly changed. While the uniform reaction rates and concentration aid the battery's ability to hold charge, the rise in terminal voltage is mostly attributed to the temperature coefficients. The temperature coefficients account for temperature rise in electrochemical cells effects on terminal voltage at the same electrolyte concentration. The effect of these coefficients outweighs any decrease in voltage that may be caused by a decrease in gradient for the isothermal, adiabatic, non-adiabatic cases, and non-isothermal finite element analysis.

For each of the cases, significant change in voltage experienced at the terminals only resulted from temperature change of at least 10 degrees Kelvin. Therefore, for the isothermal simulation, temperatures that varied 20 degrees Kelvin showed obvious change which was later verified through experimental processes. For the simulations incorporating transient heat generation, considerable temperature increase for typical battery operation only occurs at high discharge currents, 30 A and above. Consequently, substantial change in overall battery performance occurs later in the discharge process as the battery experiences temperature change between 10 and 30 degrees Kelvin well after the initial load is applied. Additionally, typical lead acid batteries are charged at relatively low currents (below 20 A), therefore, the thermal effects during charging has negligible effects on performance.

Examining the different causes for heat generation reveals the contribution of the reversible and irreversible processes. The reversible effects calculated using the

instantaneous temperature and temperature coefficient is consistent regardless of the applied load. However, as the temperature continues to rise the reversible effects grow proportionately. The irreversible effects calculated as the product of overpotential and volumetric current for each grid are constantly changing throughout battery operation. As a result, the percentage of heat generation caused by overpotentials is directly dependent on the current applied. For currents below 30 A, the reversible effects are an order of magnitude higher. However, the irreversible and reversible effects exhibit comparable contributions to the overall heat generation of the system for discharge current exceeding 70 A.

Incorporating the parameters employed during the MATLAB simulation to calculate the average cell temperature, a 3D finite element model was constructed. Extraction of heat generation rates during various loads calculated from the MATLAB model were input into the finite element analysis to observe the effects. Heat generation was applied along the electrode/electrolyte interface per square meter or to the entire cell volume per cubic meter. Temperature distribution from the non-isothermal finite element simulation is consistent with thermal imaging data gathered revealing the maximum temperature in the center of the cell slowly decreasing towards the boundaries a total of 5 °K under 60 A discharge. Similar temperature distribution arose regardless of load current, only differing in magnitude.

In addition to modeling efforts, another major contribution of the research is the battery testing station constructed to simulate automotive conditions allowing for control of external temperature, supply and load currents, as well as the ability to record the data

from the appropriate locations. Employing the testing station allowed for extensive testing of the lead acid batteries while providing real world data for comparison with simulation results. First, the effects of vibration on battery performance were extensively examined revealing no change regardless of amplitude or frequency applied. Through initial comparison of results, changes were made to the model and project focus. The thermal effects became to focal point of the remaining modeling and experimental testing. As for the modeling modifications, the maximum electrolyte concentration approximated by previous researchers did not hold true for the battery under observation. Therefore, through communication with the manufacturer, the maximum specific gravity was obtained and the corresponding concentration calculated. Following the correction, the results were largely improved.

Overall, the goals set prior to modeling and experimental efforts were achieved. Most importantly the simulations show good representation of battery performance under various thermal and electrical loads including step and ramp illustrated in the sections above. However, the overall system has a few minor shortcomings leaving room for additional testing. Namely, the MATLAB simulation is capable of calculating the SOC as a function of the applied load of a certain amount of time, but reliable approximation of battery SOC during experimental processes is absent without the use of a hydrometer to measure electrolyte specific gravity that will render the battery useless. As a result, the majority of tests were carried out from full charge, 100 % SOC, in order to assure dependable results.

Along with adequately representing a battery cell, the model seeks to fully characterize a six cell battery as well as allow for relatively simple implementation of different battery types and designs. While experimental testing is performed using a Songwoo 60 A-h battery with a specified maximum voltage and electrolyte concentration, replacement of these three values, capacity, maximum voltage and concentration, will provide sufficient representation of similar lead acid battery designs. However, the cell dimensions and porosity must be closely approximated in order to obtain reliable results as discussed in Section 4.1.4. Suitable battery parameters will allow designers and manufacturers to accurately simulate several battery designs with varying acid concentration, material properties, and dimensions in order to maximize results. In addition, the MATLAB simulation will approximate battery performance if implemented into existing vehicle models from typical internal combustion or hybrid power systems.

## **7.1 Future Work**

The modeling and experimental data provide a full representation for the specific lead acid battery under observation, also allowing for manipulation of battery parameters to simulate other battery designs. In addition, similar approaches are employed to model various battery types such as lithium ion and nickel metal hydride. The methods of quantifying the electrochemistry and heat generation hold true for each of the common automotive battery types. Therefore, the temperature change and the effects on each battery type can be further explored using both MATLAB and finite element modeling software using a similar approach by inserting the appropriate parameters.

## REFERENCES

1. H. Bode, *Lead Acid Batteries*, Wiley and Sons, New York, NY, 1977.
2. Jasinski, Raymond, *High Energy Batteries*, Tyco Laboratories, Inc. Bear Hill, Waltham, Massachusetts, 1967.
3. J.J. Esperilla, J. Felez, G. Romero, A. Carretero, A full model for simulation of electrochemical cells including complex behavior, *Journal of Power Sources* 165 (2007) 436–445.
4. T.V. Nguyen, R.E. White, H. Gu, *J. Electrochemical Soc.* 137 (1990), 2998–3003.
5. Gu, H. *Mathematical Modeling in Lead Acid Battery Development*. General Motors Research Laboratory.
6. Gu, W. B., Wang, G. Q., Wang, C. Y. Modeling the overcharge process of VRLA batteries, *Journal of Power Sources* 108 (2002) 174-184.
7. W.B. Gu, C.Y. Wang, *Thermal-Electrochemical Modeling of Battery Systems*, *Journal of Electrochemical Soc.* 147 (2000) 2910–2922.
8. Crompton, T. R. *Battery Reference Book*. Former Head of Metals Section, North West Water, UK, 2000
9. Sung Chul Kim, Won Hi Hong. Analysis of the discharge performance of a flooded lead/acid cell. *Journal of Power Sources* 77\_1999.74–82.
10. W.H. Tiedemann, J. Newman, *Battery design and optimization* Princeton, in: S. Gross \_Ed., *The Electrochemical Society Softbound, Proceedings Series*, Princeton, NJ, 1979, p. 23.
11. Takayuki Doi. Computer simulation of a porous positive electrode. *Journal of Power Sources* 174 (2007) 779–783.
12. Nguyen, T.V. A Mathematical Model of Sealed Lead Acid Battery. *Electrochimica Acta*, Vol. 38, No. 7. pp. 935-945. 1993.
13. Venkat Srinivasan, G. Q. Wang, C. Y. Wang. *Mathematical Modeling of Current Interrupt*, *Journal of The Electrochemical Society*, 150, A316-A325, 2003.
14. D. Baert, A. Vervaeet. Lead-acid battery model for the derivation of Peukert's law. *Electrochimica Acta* 44 (1999) 3491-3504.
15. M.A. Dasoyan, I.A. Aguf, *Current Theory of Lead Acid Batteries*, Technicopy Limited, 1979.
16. P. Ekdunge, A simplified model of the lead/acid battery, *Journal of Power Sources* 46 (1993) 251-262.
17. W.G. Sunu, *Electrochemical cell design*, in: R.E. White, \_Ed., *Plenum*, New York, 1984, p. 357.

18. J. Thoma, B. Ould Bouamama, Modeling and Simulation in Thermal and Chemical Engineering, Springer-Verlag, Berlin, 1999.
19. W.A. Facinelli, Modeling and simulation of lead-acid batteries for photovoltaic systems, Ph.D. thesis, Arizona State University (1983).
20. R. David Prengaman, Improvements to active material for VRLA batteries, Journal of Power Sources 144 (2005) 426–437.
21. W. Hoffman, Lead and Lead Alloys: Properties and Technology, 2<sup>nd</sup> ed., Springer-Verlag, New York, 1970, p. 330.
22. Otmar Bitsche, Guenter Gutmann, Systems for hybrid cars, Journal of Power Sources 127 (2004) 8–15.
23. P.D. Vidts, R.E. White, J. Electrochemical Soc. 144\_1997.1343.
24. Morton, K. W., Mayers, D. F. Numerical Solution of Partial Differential Equations. 2<sup>nd</sup> ed. Cambridge University Press, 2005. Cambridge, New York.
25. Fasih, Ahmed, Modeling and Fault Diagnosis of Automotive Lead Acid Batteries. Ohio State University. 2006. Columbus, Ohio.
26. Nova Resource. June 4, 2008. <<http://novaresource.org/alternator.htm>>.

## APPENDIX

Parameter	Value	Reference
Initial specific surface area for Pb electrode $a_{\max\text{Pb}}$ ( $\text{cm}^{-1}$ )	23000	3
Initial specific surface area for $\text{PbO}_2$ electrode $a_{\max\text{PbO}_2}$ ( $\text{cm}^{-1}$ )	230000	3
Initial exchange current density $i_{\max\text{Pb}}$ ( $\text{A cm}^{-2}$ )	$4.96 \times 10^{-6}$	3
Initial exchange current density $i_{\max\text{PbO}_2}$ ( $\text{A cm}^{-2}$ )	$3.19 \times 10^{-7}$	3
Pb electrode conductivity ( $\text{S cm}^{-1}$ )	500	7
$\text{PbO}_2$ electrode conductivity ( $\text{S cm}^{-1}$ )	$4.8 \times 10^4$	7
Initial cell temperature T (K)	298	-
Ambient temperature $T_a$ (K)	298	-
Standard reduction potential $E_{\text{Pb}}$ (V)	-0.356	6
Standard reduction potential $E_{\text{PbO}_2}$ (V)	1.685	6
Cathodic charge transfer coefficient $\alpha_{\text{Pb}}$	.45	3
Anodic charge transfer coefficient $\alpha_{\text{Pb}}$	1.55	3
Cathodic charge transfer coefficient $\alpha_{\text{PbO}_2}$	.85	3
Anodic charge transfer coefficient $\alpha_{\text{PbO}_2}$	1.15	3
Exponent for exchange current density $\xi_{\text{Pb}}$	0	3
Exponent for exchange current density $\xi_{\text{PbO}_2}$	0.3	3
Pb electrode size $V_{\text{Pb}}$ ( $\text{cm}^3$ )	49	-
$\text{PbO}_2$ electrode size $V_{\text{PbO}_2}$ ( $\text{cm}^3$ )	151.9	-
Mean ionic coefficient $\gamma_{\pm}$	fitted from data	1
Specific heat capacity of electrolyte $c_v$ ( $\text{J} \cdot (\text{kg} \cdot \text{C})^{-1}$ )	fitted from data	1



Temperature coefficient $\partial E_{Pb}/\partial T$ (V-K <sup>-1</sup> )	-1.15x10 <sup>-3</sup>	6
Temperature coefficient $\partial E_{PbO_2}/\partial T$ (V-K <sup>-1</sup> )	3.27x10 <sup>-4</sup>	6
Thermal conductivity container k (W m <sup>-1</sup> C <sup>-1</sup> )	0.2	-
Thickness of container wall $\varepsilon$ (m)	0.005	-
Maximum electrolyte density (kg/L)	1.28	-
Maximum electrolyte concentration $[SO_4H_2]_{max}$ (mol/cm <sup>3</sup> )	5.6x10 <sup>-3</sup>	-